



저작자표시-비영리-변경금지 2.0 대한민국

이용자는 아래의 조건을 따르는 경우에 한하여 자유롭게

- 이 저작물을 복제, 배포, 전송, 전시, 공연 및 방송할 수 있습니다.

다음과 같은 조건을 따라야 합니다:



저작자표시. 귀하는 원 저작자를 표시하여야 합니다.



비영리. 귀하는 이 저작물을 영리 목적으로 이용할 수 없습니다.



변경금지. 귀하는 이 저작물을 개작, 변형 또는 가공할 수 없습니다.

- 귀하는, 이 저작물의 재이용이나 배포의 경우, 이 저작물에 적용된 이용허락조건을 명확하게 나타내어야 합니다.
- 저작권자로부터 별도의 허가를 받으면 이러한 조건들은 적용되지 않습니다.

저작권법에 따른 이용자의 권리와 책임은 위의 내용에 의하여 영향을 받지 않습니다.

이것은 [이용허락규약\(Legal Code\)](#)을 이해하기 쉽게 요약한 것입니다.

[Disclaimer](#)



이학박사 학위논문

**Effect of hydrogen on electronic
properties of two dimensional
Graphene, Graphene oxide and MoS₂**

**수소가 2차원 그래핀, 그래핀산화물,
이황화몰리브데늄의 전기적 특성에 주는 영향**

2017년 2월

서울대학교 대학원

융합과학부 나노융합전공

박 민

Effect of hydrogen on electronic properties of two dimensional Graphene, Graphene oxide and MoS₂

Min Park

Supervised by

Professor Yung Woo Park

A Dissertation
Submitted to the Faculty of
Seoul National University
in Partial Fulfillment of
the Requirements for the Degree of
Doctor of Philosophy
February 2017

*Program in Nano Science and Technology
Department of Transdisciplinary Studies
The Graduate School
Seoul National University*

Abstract

Effect of hydrogen on electronic properties of two dimensional Graphene, Graphene oxide and MoS₂

Min Park

Program in Nano Science and Technology

Department of Transdisciplinary Studies

The Graduate School

Seoul National University

Two-dimensional(2D) materials have attracted great scientific attention due to their extraordinary and fascinating properties. Graphene and transition metal dichalcogenides such as MoS₂, have shown promising candidate for gas sensing, flexible electronics, energy harvesting due to their high mechanical properties, high surface-to-volume ratio, low noise and sensitivity of electronic properties to the changes in the surroundings. It has been intensively investigated on the interaction between hydrogen and 2D materials both experimentally and theoretically. Therefore, it is required that studies of the interaction between hydrogen and 2D materials have been increasingly required due to the indispensable modification of the electronic structure of 2D materials for device applications and the possibility of using 2D materials as hydrogen storage materials. In this dissertation, we will describe the effect hydrogen on the electronic properties of 2D materials such as Graphene, Graphene Oxide, MoS₂ using electrical conductivity, thermoelectric power (TEP), and Raman spectroscopy.

The first part of this thesis describes presenting a simple method to fabricate *p-n* junction in a single layer graphene by means of the selective H₂ exposure. This is achieved by the fabrication of poly methyl methacrylate (PMMA) window on the half region of the graphene. The gate voltage (V_G)- dependent resistance of single layer graphene is measured as a function of H₂ (12 bar) exposure time at 350 K. As hydrogen exposed sample, *n*-doping of the window region shifts to the negative V_G region prominently compared with that of the PMMA-covered region. The temporal evolution of Dirac point both PMMA region and window region follows first order Langmuir adsorption model. Consequently, a single graphene *p-n* junction is obtained by measuring the V_G -dependent resistance of the whole graphene region.

The second part of this thesis describe the electrical transport properties of single layer reduced graphene oxide(RGO) and its hydrogenation. The single layer RGO is obtained by bubble deposition method and thermal reduction. The structure and reduction efficiency is confirmed by X-ray photoelectron spectroscopy and Raman spectroscopy, respectively. The RGO contains 82 % of C=C and C-C species and have 2 nm of defect distance. The transfer characteristic of RGO shows ambipolar transport for temperature range (10 K < T < 300 K). The conductance of Ohmic regime is rapidly decrease as decrease temperature which means a sign of variable range hopping. The Efros-Skhlovskii variable range hopping (ES-VRH) is a dominant charge transport (T < 70 K). With increase temperature (T > 70 K), the charge transport become 2D-VRH due to absence of coulomb gap. The ES-VRH is additionally confirmed by electric field dependent conductance of non-Ohmic regime at low temperature. The TEP exhibits that the dominant charge carrier in RGO is switched at charge neutrality point. The Seebeck coefficient is proportional to $T^{1/3}$ (50 K < T < 300 K) suggesting a 2D VRH conduction. Hydrogenation of RGO shows n-type doing resulting from hydrogen adsorption. Maximum resistance of transfer curve is reduced by improvement of reduction efficiency.

The third part of this thesis will introduce the effect of hydrogen on geometric and electronic structure of single layer MoS₂. MoS₂ is well known catalyst for hydrodes-

ulfurization process and the hydrogen adsorbed plays an important role in its activation. So that, investigations of the interaction between molecular hydrogen and molybdenum disulfide have been increasingly demanded for the understanding of the HDS process, especially the hydrogen adsorption on MoS₂ and creation of sulfur vacancies in MoS₂. Electrical transport properties were measured as a function of time at 350 K and 12 bar of hydrogen atmosphere. Upon to hydrogen exposure, the threshold voltage of MoS₂ is shifted toward negative bias, which indicates n-type doping by thiol bonding and sulfur vacancy. The temporal evolution of threshold voltage follows double exponential first adsorption model, which consist of thiol bonding term and sulfur vacancy term. The mobility has increase as exposure to hydrogen, which result from screening of long range scatterer by intercalated hydrogen between MoS₂ and substrate. The n-type doping of MoS₂ by hydrogen is confirmed by TEP measurement. The TEP curve is shifted toward negative gate bias region likewise transfer characteristics. We observe the red shift of the two prominent peaks in Raman spectroscopy by electron doping and strain.

Keywords: Graphene, MoS₂, Electron doping, Hydrogenation, Graphene oxide

Student Number: 2010-22667

Contents

Abstract	i
Contents.....	iv
List of Figures	vii
Chapter 1. Research background.....	1
1.1 2D Materials.....	1
1.1.1 Graphene	2
1.1.2 Graphene Oxide	4
1.1.3 MoS ₂	5
1.2 Raman Spectroscopy.....	7
1.2.1 Raman Spectroscopy of graphene and graphene oxide.....	7
1.2.2 Raman Spectroscopy of MoS ₂	9
1.3 Variable range hopping theory.....	12
1.4 Thermoelectric power	14
Chapter 2. Formation of graphene <i>p-n</i> junction by selective hydrogen adsorption	21
2.1 Introduction.....	21
2.2 Experimental details.....	22
2.3 Result and discussion.....	24
2.3.1 Transfer characteristics	24
2.3.2 Raman spectroscopy.....	30
2.4 Summary	31

Chapter 3. Electrical transport of reduced single layer graphene oxide and its hydrogenation	35
3.1 Introduction.....	35
3.2 Experimental details.....	36
3.2.1 Synthesis of graphene oxide	36
3.2.2 Preparation of single layer reduced graphene oxide	37
3.2.3 Transport properties measurement.....	39
3.3 Characterization (AFM, Raman, XPS)	39
3.4 Result and discussion.....	42
3.4.1 Temperature dependence of conductance	42
3.4.2 Thermoelectric power	48
3.5 Hydrogenation.....	51
3.6 Summary	52
Chapter 4. Effect of hydrogen on geometric and electronic structure of MoS₂.....	57
4.1 Introduction.....	57
4.2 Experimental details.....	59
4.3 Result and discussion	60
4.3.1 Transfer characteristics	60
4.3.2 Mobility.....	62
4.3.3 Effect of sulphur vacancy and thermoelectric power.....	64
4.3.4 Raman spectroscopy.....	67
4.4 Summary	68
Chapter 5. Conclusion	73
Appendix	77
A.1 Introduction.....	77

A.2 Experimental details.....	78
A.3 Result and discussion	79
A.3.1 Temperature dependence of resistance	79
A.3.2 MR of 1T-TaS ₂ with CCDW state	80
A.3.3 MR of 1T-TaS ₂ with H state	82
A.4 Summary	83
국문 초록	87

List of Figures

1.1 Band structures of single-layer hexagonal boron nitride, MoS ₂ , black phosphorus and graphene	1
1.2 Schematic of the honeycomb lattice structure of graphene showing σ -bonds and π -bonds and dispersion over the entire Brillouin zone.....	2
1.3 Transfer curve of graphene and the electron and hole symmetric and conical band structure of graphene.....	3
1.4 Schematic of the process developed to make GOs.....	4
1.5 Three-dimensional representation of the structure of MoS ₂ and top and side views of 2H, 1T and 1T' phase.....	5
1.6 Three-dimensional representation of the structure of MoS ₂	6
1.7 The Raman spectra of single layer graphene and multi-layer graphene.....	7
1.8 Raman spectra of fluorine plasma treated graphene and reduced graphene oxide.....	8
1.9 I _D /I _G ratio vs distance between two defects (L _D)	9
1.10 Raman active mode of MoS ₂ and the number of layer dependence of Raman spectra.....	10
1.11 Effect of strain on Position of the A _{1g} and E ¹ _{2g} Raman peaks from monolayer and few-layer MoS ₂	11
1.12 Schematic of Mott variable range hopping and Efros-Shklovskii variable range hopping behavior at low temperature regime.....	12
1.13 The schematic of redistribution of the carrier in response to the temperature gradient along the material.....	14
1.14 The TEP of doped multi wall carbon nanotubes and the gate dependent TEP of	

single layer graphene	15
2.1 Optical image of graphene device fabricated covered with PMMA and transfer curve of PMMA covered graphene device	24
2.2 Process for PMMA window fabrication. The optical image of the PMMA window on single-layer graphene. I, II, and III indicate the three electrodes	25
2.3 $R(V_G)$ of the window and PMMA-covered regions as a function of the exposure time	26
2.4 Shift in the CNP as a function of H_2 adsorption for two regions	27
2.5 Transfer curves of pristine sample and hydrogenated sample and the fitting parameters	28
2.6 $R(V_G)$ between electrodes I and III. As the exposure time increased, P_2 developed and became prominent and ΔV_p increased	29
2.7 $R(V_G)$ s of the entire (between electrodes I and III), PMMA, and the PMMA-covered regions	30
2.8 Raman spectroscopy of the PMMA-covered and window regions before and after exposure to 12 bars of H_2 pressure	32
3.1 Schematic of the bubble deposition process and obtained sample	39
3.2 Optical image of RGO device and tapping mode AFM image with the height profile	40
3.3 XPS spectra for reduction efficiency of RGO and deconvolution of the C1's peaks	41
3.4 Raman spectra of before and after reduction	42
3.5 The gate voltage dependence of conductance as a function of temperature and the temperature dependence of conductance extracted from transfer curve	43
3.6 Reduced activation energy plotted versus temperature in a log-log scale	44

3.7 Electrical conductance of the RGO, G VS $T^{-1/3}$ and $T^{-1/2}$	45
3.8 Semi-log scale plot of G vs $T^{-1/2}$ and $T^{-1/3}$ for different gate voltage.....	46
3.9 The E_{CG} vs V_G	47
3.10 $\ln G$ vs $E^{-1/2}$ for RGO device as a function of gates voltage.....	48
3.11 TEP as a function of back gate voltage and TEP vs $T^{1/3}$	50
3.12 The transfer curve of RGO before and after hydrogen exposure.....	52
4.1 Simplified diagram of a HDS process for thiophene elimination.....	59
4.2 The transfer curves of MoS_2 as a function of H_2 exposure time at 350 K.....	61
4.3 The temporal evolution of threshold voltage of MoS_2	62
4.4 Mobility of as a function of hydrogen exposed time.....	64
4.5 Transfer curves of MoS_2 device before and after hydrogen exposure and evacuation.....	66
4.6 Gate voltage dependent TEP of MoS_2 device before and after hydrogen exposure and evacuation.....	67
4.7 Raman spectra of pristine MoS_2 and hydrogen exposed MoS_2	68
A.1 Temperature dependence of the four probe resistance on temperature sweep	80
A.2 MR of 1T-TaS ₂ with CCDW State at 1.6, 3, 6, 10, 15, 25 K.....	81
A.3 MR of 1T-TaS ₂ with H state at 1.6, 3, 6, 10, 15, 25 K.....	82

Chapter 1

Research background

1.1 2D Materials

2D materials, referred to as single layer materials, are crystalline materials consisting of a single layer of atoms. These crystal structures feature single-atom-layer or polyhedral-thick layers of atoms that are covalently or ionically connected with their neighbors within each layer. These layers are bonded together by van der Waals force along the c-axis. The weak interlayer van der Waals bonding enable the exfoliation of these layers. The simple and easy method for obtaining single- and few layer 2D materials from these solids is mechanical exfoliation of large crystals using Scotch tape. So that, the single or few layer are easily deposited onto arbitrary substrate [1].

2D materials exhibit diverse electronic properties, ranging from insulating

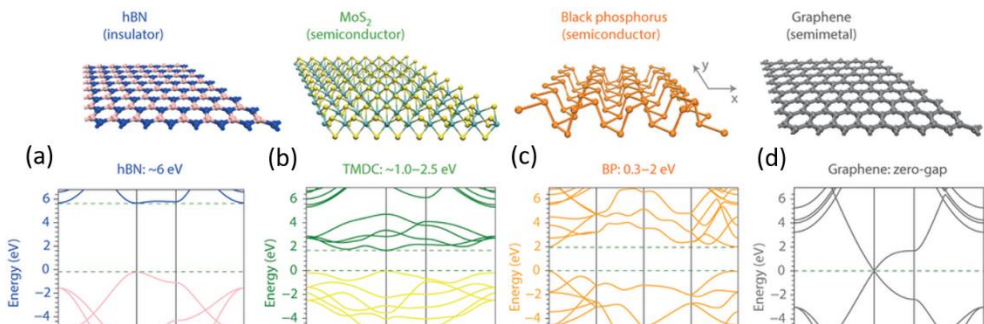


Figure 1.1 Band structures of single-layer hexagonal boron nitride (b), MoS₂ (c), black phosphorus (d) and graphene (e). Adapted from Ref. [2]

hexagonal boron nitride and semiconducting black phosphorus and MoS₂ to semi-metallic graphene shown in Fig.1.1. Among the 2D materials, Transition metal dichalcogenides (TMDCs) have a variety of electronic properties such as metallic, superconducting, semiconducting. Moreover, TMDC have three difference phase (2H, 1T and 1T') in same materials [3]. Thus, the same materials have difference electronic properties and coexistence of difference phase in the same materials [4].

1.1.1 Graphene

Graphene is a one atom thick sheet of carbon atom bonded by orbital hybridization as shown in Fig. 1.2 (a) [5]. Carbon atom has four valance electrons, three electrons in sp^2 orbital ($2s$, $2p_x$, $2p_y$) and one electron in the $2p_z$ orbital. The electron in the sp^2 orbital from in a σ bonds and bind with a carbon atom to its three neighbors. The in-plane σ bonds are origins of the honeycomb lattice with atomic distance of 1.42Å and not the contributor for electron conduction in graphene, these are responsible for the large binding energy and the mechanical properties of the graphene. Beside the electron in $2p_z$ orbital form π bonds, which is perpendicular to the plane formed due to the sideward overlap of the $2p_z$ (π) orbitals. Thus, the fourth electron in the $2p_z$

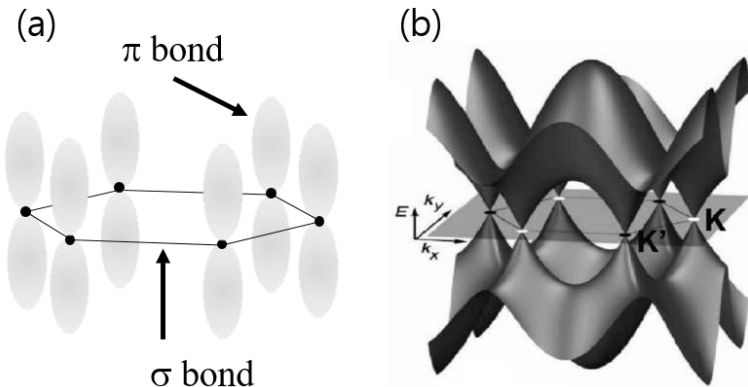


Figure 1.2 Schematic of the honeycomb lattice structure of graphene showing σ -bonds and π -bonds. (b) Electronic dispersion in the honeycomb lattice over the entire Brillouin zone. Dirac cones are located at six corners of the Brillouin Zone. Adapted from Ref. [6]

orbital is delocalized and responsible for the linear dispersion relation in the low energy regime in band structure of graphene as shown in Fig. 1.2 (b). Using a tight-binding approximation, the energy dispersion relation of graphene can be obtained [7]:

$$E_{\pm} = \pm \hbar v_F |k|$$

Here, E_+ (E_-) is conduction (valence) band, \hbar , v_F is Fermi velocity ($\sim 10^6$ m/s), k is wave vector. Graphene is unique in electronic structure. it shows band-overlap in two conical points (K and K') in the Brillouin zone, where effective carrier density is zero. The linear dispersion relation at low energy lead to zero effective mass for electrons and holes. Therefore, the charge carrier of graphene is known as massless Dirac fermions, which can be described by Dirac equations. This unique linear dispersion of graphene results in a linear density of states. The electron-hole symmetry in band structure is easily confirmed measuring gate voltage dependence of resistance as shown in Fig 1.3. Since the gate voltages adjust Fermi level of graphene. Graphene is expected to show exotic electronic properties such as ballistic transport [8], quantum Hall effect [9] and Klein Tunneling [10]. These unique electronic properties of graphene have made it suitable for applications in electronics, as well as one of the most suitable materials for studying basic quantum physics.

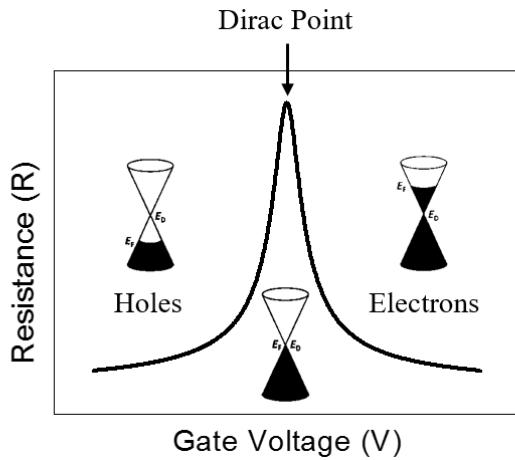


Figure 1.3 Transfer curve of graphene and the electron and hole symmetric and conical band structure of graphene. The resistance is maximum at Dirac point due to absence of effective carrier density

1.1.2 Graphene Oxide

Graphite oxide is prepared by chemical oxidation of graphite [11]. The oxidized carbon sheets are decorated with various oxygen functional groups, which not only expand the interlayer distance of graphite but also make it hydrophilic. As a result, this oxidized graphite can be easily exfoliated and dispersed in water under moderate sonication. These exfoliated individual sheets containing only one or few layer of carbon atoms like graphene derivatives, are called graphene oxide (GO). The process of graphene oxide is shown in Fig 1.4. The geometric structure of the GO is still not clearly understood due to strong disorder and depending on synthesis method and degree of oxidation. It typically preserves the structure of graphene. Surface of GO synthesized using modified Hummers method are functionalized with oxygen epoxide groups, carbonyl ($C=O$), hydroxyl (-OH), phenol [12]. Graphene oxide layers are about 1.1 nm thick. The oxygen atoms are arranged in a rectangular pattern. The edges of GO layers are terminated with carboxyl and carbonyl groups [13]. The most attractive property of GO is that it can be reduced to graphene-like sheets by removing the oxygen functional groups with the recovery of a graphitic structure [14,15]. Moreover, it is enable to be sufficient scalable for the bulk production. Thus, the reduced GO (RGO) sheets are usually considered as one kind of chemically derived graphene. The GO is simply controlled electronic properties from insulating to metallic by adjusting the degree of reduction. GO/RGO have the processing advantages and unique properties such as mechanical stability, tunable electrical, and optical properties. They can be applied for industrial applications such as transparent electrode [16], chemical sensors [17], thin film transistors [18], supercapacitors [19] and nonvolatile memory devices [20].

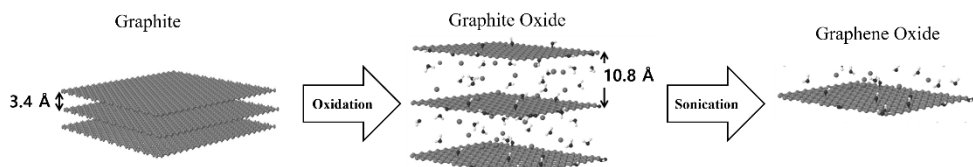


Figure 1.4 Schematic of the process developed to make GOs. Graphite is chemically functionalized and exfoliated by modified Hummers method. The graphite oxide was sonicated for separation of individual sheets. Adapted from Ref. [21]

1.1.3 MoS₂

MoS₂ is a family of TMDCs. MoS₂ nanoparticles are conventionally well known in terms of hydrodesulfurization catalyst to remove sulfur compounds from crude oil. The mechanical cleavage method has been developed, MoS₂ have received the attention of researchers. In contrast to graphene, MoS₂ has sizeable band and n-type semiconducting property, which can be applied for post silicon materials. Figure 1.5 (a) shows that MoS₂ has a plane of hexagonally arranged molybdenum atoms sandwiched between two planes of hexagonally arranged sulfur atoms, with the covalently bonded S-Mo-S atoms [22]. The most commonly observed crystal symmetry structures of MoS₂ are hexagonal (2H phase) and octahedral (1T phase) distorted octahedral (1T' phase) configuration as shown in Fig. 1.5 (b). The 2H phase of MoS₂ are semiconducting whereas 1T and 1T' phase of MoS₂ is metallic. The 1T and 1T' phase is metastable. It can be easily transformed to the thermodynamically stable 2H phase [23]. 1T and 2H phase can coexist in the same MoS₂ sheets and that the phase boundary between two phase is atomically sharp and no defects [24].

Figure 1.6 shows the band structure of 2H-MoS₂. In bulk MoS₂, the valence band maximum is located at the Γ point, while the conduction band minimum is located almost halfway along the Γ -K direction, which is the indirect band gap with 1.2 eV. As the number of layer decreases, the fundamental indirect band-gap increases

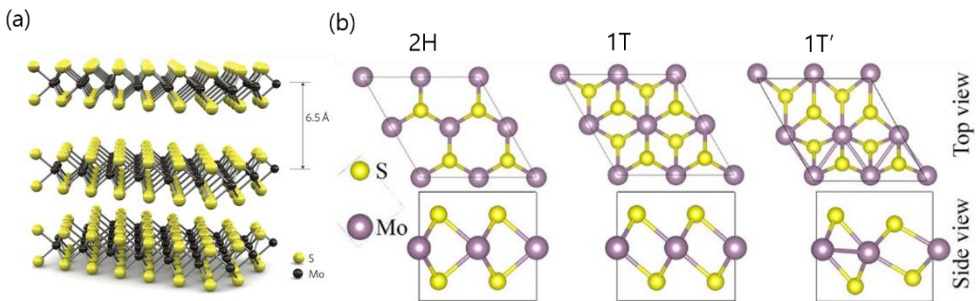


Figure 1.5 (a) Three-dimensional representation of the structure of MoS₂. Adapted from Ref [26] (b) Top and side views of the 2H, 1T and 1T' phase. The Mo atoms have octahedral and trigonal prismatic coordination in the 1T/1T'- and 2H-MoS₂, respectively. Adapted from [23].

due to the quantum confinement effect. In the monolayer limit, the band gap of MoS₂ become the direct band-gap with 1.9 eV at the K-Point [25].

This property of MoS₂ make it possible to be used in the industrial application such as microelectronics [26], photovoltaics [27] and hydrogen evolution reaction (HER) [28]. Additionally, the odd number of layers of MoS₂ could produce piezoelectric voltage and current outputs, indicating its potential applications in energy harvesting [29].

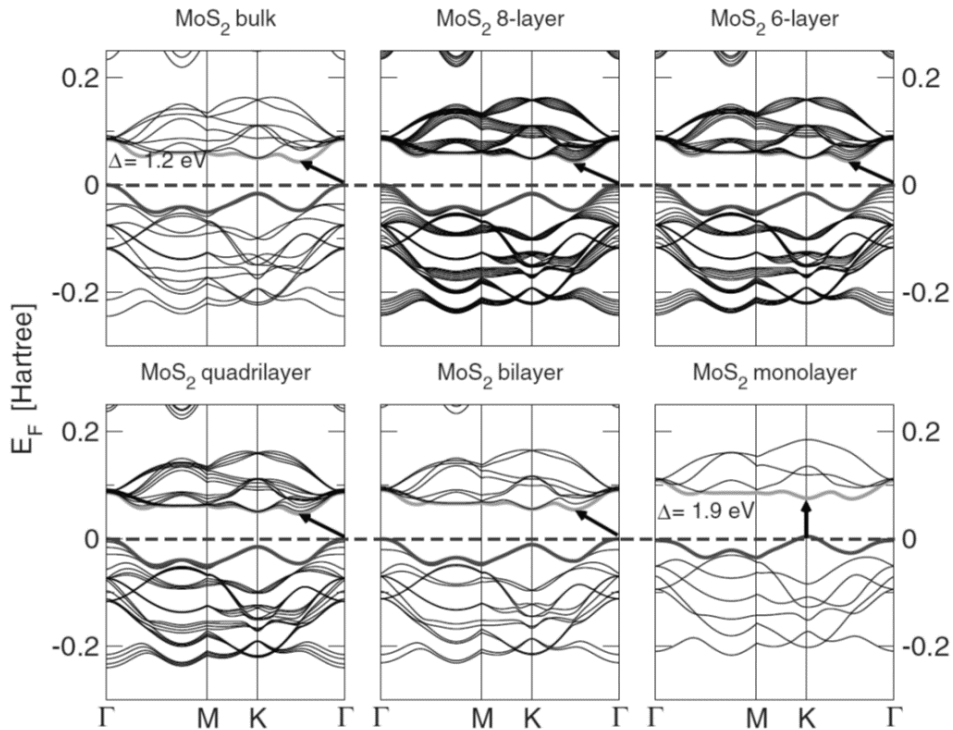


Figure 1.6 Band structures of bulk, few layer and monolayer of MoS₂. The arrows indicate the fundamental band gap (direct or indirect). The top of valence band (blue) and bottom of conduction band (green) are highlighted. Adapted from Ref. [23].

1.2 Raman spectroscopy

1.2.1 Raman spectroscopy of Graphene and Graphene oxide

Raman spectroscopy has been widely used for characterize 2D materials and carbon based materials not only the determination of structure but also electronic properties of sample. When incident light interacts with molecular vibrational modes and phonons in a sample, the light energy is shifted down (Stokes) or up (anti-Stokes) through inelastic scattering [30]. Raman spectra of graphene can provide an information related to the number of layers, doping, strain, disorder. In general, the three representative (G, 2D and D) Raman peaks are observed. G peak near the 1580 cm^{-1} is a primary in-plane vibrational mode involving the sp^2 hybridized carbon atoms and D peak near the 1350 cm^{-1} is a ring breathing mode from sp^2 carbon rings, although to be active the ring must be adjacent to a graphene edge or a defect. 2D peak near the 2690 cm^{-1} is a second-order overtone of a different in-plane vibration of D peak [32]. Figure 1.7 shows the Raman spectra of single layer graphene. The 2D peak has been used to probe the single layer graphene. 2D band is observed to be a single Lorentzian peak with a full width at half maximum (FWHM) of $\sim 30\text{ cm}^{-1}$. When increasing the layers of graphene in the sample, the 2D band is split into multi

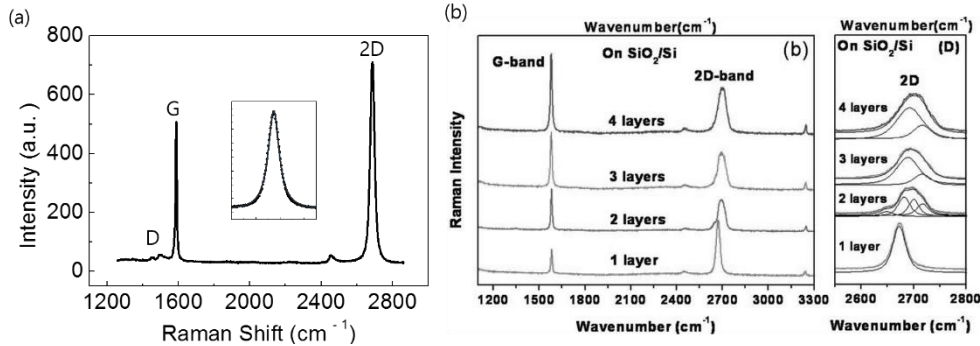


Figure 1.7 (a) The Raman spectra of single layer graphene and insert is single Lorentzian fitting of 2D peak (b) Left: The Raman spectra as a number of layer. Right: The deconvolution of 2D peak of single (multi-) Lorentzian peak for mono, bi, and few-layer. adapted from Ref [31]

overlapping of Lorentzian. Figure 1.8 shows the disordered graphene with different defect concentration. and RGO with different reduction temperature. As the amount of disorder in graphene increases, the Raman intensity increases for the three separate disorder peaks (D , D' and $D+G$) shown in Fig. 8. The D peak, intervalley scatters from K to K' , the D peak increases at first and then decreases while broadening. The D' peak near the 1620 cm^{-1} , intravalley scatters from K to K , increases and eventually merges with the G peak. and $D+G$ near the 2940 cm^{-1} , combination scattering peak increases in intensity and broadens [33]. The $2D$ peak monotonously decreases until it almost disappears. Likewise, the Raman spectra of reduced graphene oxide shows the opposite behavior with increase reduction temperature. The pristine graphene oxide has broad D and G peak, as increase reduction temperature, The D peak and G peak become more sharp and $2D$ peak are restored. The ratio of peak intensities I_D/I_G can be used to probe the level of disorder and distance between two defects in graphene. I_D/I_G ratio vs distance between two defects (L_D) are plotted in Fig. 1.9. However, the same I_D/I_G ratio have difference L_D value at two difference regions. As the amount of disorder increase, the FWHM of Raman peaks are broadened. It is possible to distinguish between stage 2 and stage 1 region by analyzing Raman spectra in terms of the FWHM.

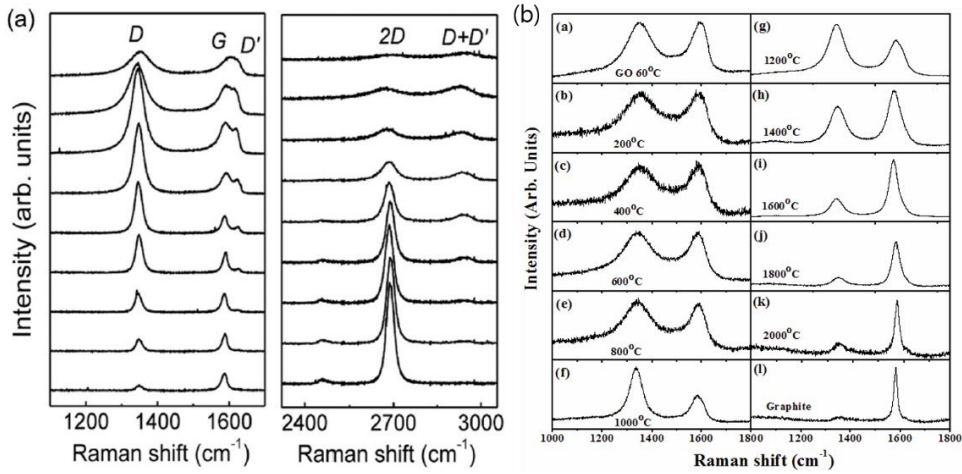


Figure 1.8 (a) Raman spectra of fluorine plasma treated graphene with increasing defect concentrations. Adapted from Ref. [34] (b) Raman spectra of reduce graphene oxide with increasing reduction temperature. Adapted from Ref. [35]

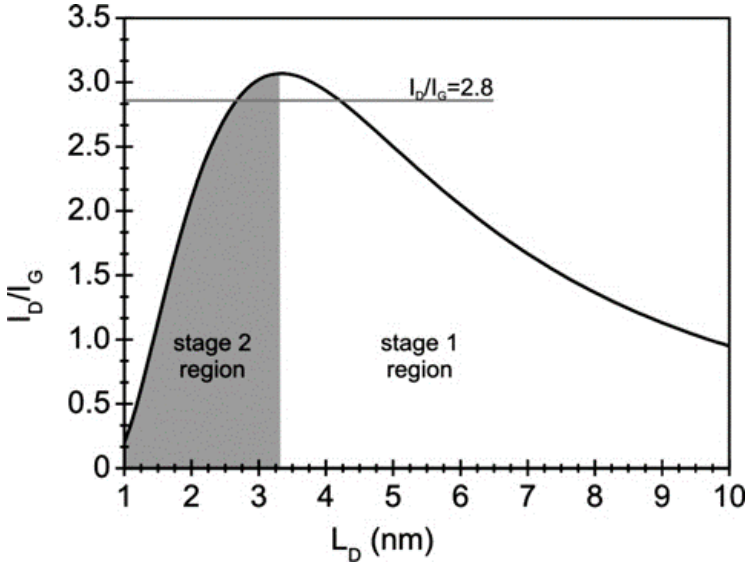


Figure 1.9 I_D/I_G ratio vs. distance between two defects (L_D), for 532 nm laser excitation (maximum I_D/I_G ratio 3.1), which is adapted Ref. [36]

1.2.2 Raman spectroscopy of MoS₂

MoS₂ have four first order Raman active mode three in-plane vibration (E_{1g} , $E^{1_{2g}}$, and $E^{2_{2g}}$) mode and one out of plane vibration mode, A_{1g} as shown in Fig. 1.10 (a) [37]. The Raman spectra of MoS₂ is usually measured two prominent peak ($E^{1_{2g}}$ near the 384 cm^{-1} and A_{1g} modes near the 410 cm^{-1}). The other two peaks could not be detected due to selection rule for back scattering geometry on a basal plane [38]. The Raman mode of MoS₂ can probe information of the thickness, doping and strain. The difference between the two main modes have been used to identify the number of layers [39]. Figure 1.10 (b) shows Raman spectra of 1 to 4 layer MoS₂ [40]. The separation between the two modes decreases with decreasing thickness of the material. The $E^{1_{2g}}$ mode redshifts as the number of layers increases whereas the A_{1g} mode blue shifts [41]. The blue shift of A_{1g} mode with the number of layers can be explained by classical model for coupled harmonic oscillators, whereas the redshift of $E^{1_{2g}}$ with increasing number of layers has been attributed to the enhancement of

dielectric screening of the long-range Coulomb interactions [42]. The strain affects Raman spectra of MoS₂. As uniaxial strain is applied to MoS₂, the E¹_{2g} is broadened and split into two modes as the degeneracy is lifted as shown Fig. 1.10 (b). Thus, the in-plane E¹_{2g} mode splits and redshifts whereas the out-of-plane A_{1g} mode is not affected by uniaxial strain, which is good indicator for probing strain as shown in Fig. 1.11 (a, b) [43]. The A_{1g} mode is very sensitive to adsorbates on the MoS₂ surface and electron doping. A_{1g} mode shows a red shift and an increase in the peak width with increasing electron doping level due to stronger electron-phonon coupling of the A_{1g} mode, whereas the E¹_{2g} mode is not affected [44], which is shown in Fig. 1.11 (c, d). The blue shift of A_{1g} is also observed in *p*-doping of MoS₂ [45]. Therefore, the A_{1g} mode can be used to probe the doping effect of MoS₂.

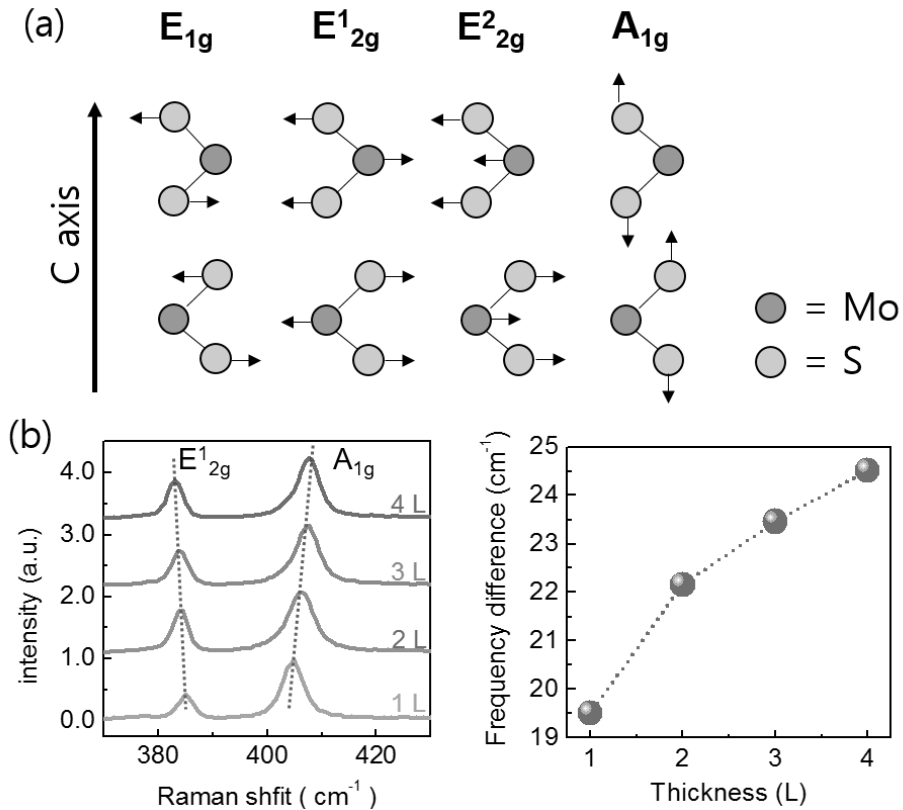


Figure 1.10 (a) Raman active mode of MoS₂ (b) (a) Left: The number of layer dependence of Raman spectra. Right: As the thickness increases, the frequency difference between E¹_{2g} and A_{1g} increases from 19.5 to 24.5 cm⁻¹.

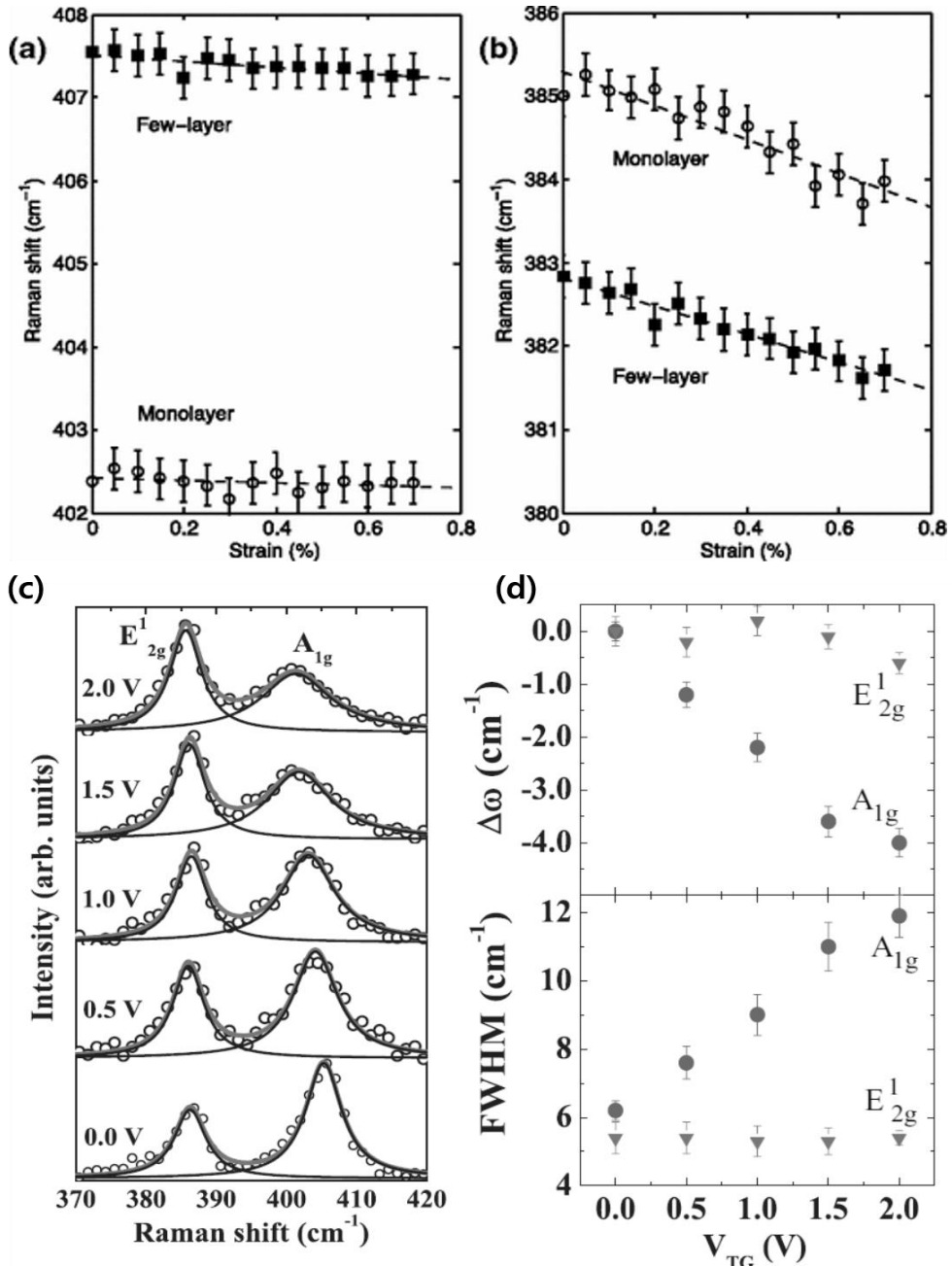


Figure 1.11 Effect of strain on Position of the (a) A_{1g} and (b) E_{2g}^1 Raman peaks from monolayer and few-layer MoS₂. Adapted from Ref. [43]. (c) Raman spectra of monolayer MoS₂ at different top-gate voltages V_{TG}. Change in the (b) Raman shift ω and (c) FWHM of A_{1g} and E_{2g}^1 modes as a function of V_{TG} Adapted from Ref. [44].

1.3 Variable range hopping theory

Variable range hopping theory describes the low temperature behavior of the conduction in strongly disordered systems with localized carrier state, which is invented by Mott in 1969 [46]. In disordered system, the charge carriers with non-metallic behaviors are observed by disorder, which result from that the wave function of electron decay by the interference with the source of disorders. The conduction of carriers among the difference localization site is occurred by thermal hopping. The localized states have different energy differences and distribution in distance. Therefore, the hopping occurs statistically among the hopping sites. Charge carrier prefers to hop to the nearest neighbor in distance and the next site of small energy difference. The competing factors of the hopping probability can be the distance and the energy difference between sites, which is variable range hopping. Mott's theory assumes that the density of states is constant in vicinity of the Fermi level (Fig. 1.12 (a)). This assumption neglects Coulomb interactions between the particles. At low temperatures the conductivity then shows a universal behavior:

$$\sigma(T) = \sigma_0 \exp\left(-\frac{T_0}{T}\right)^{\frac{1}{d+1}}, \text{ with } T_0 \equiv T_M = \frac{\beta}{k_B g(\varepsilon) \xi^d} \quad (1)$$

where, k_B , $g(\mu)$, ξ , β and d is Boltzmann constant, the density of states at the Fermi level, the localization radius of states vicinity of the Fermi level, a numerical coefficient, and the dimensionality of system, respectively.

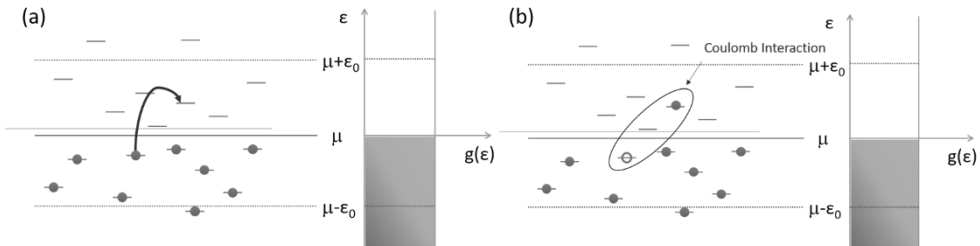


Figure 1.12 Schematic of (a) Mott variable range hopping and (b) Efros-Shklovskii variable range hopping behavior at low temperature regime.

However, Efros and Shlovskii mentioned that, correlations between localized charge carriers are especially relevant for strong interactions and low temperatures (Fig 1.12 (b). When an electron hops from one site to another, it leaves a hole and the system must have enough energy to overcome Coulomb interaction. The density of state (DOS) vanishes near the Femi energy level due to the long range Coulomb interaction [47] This vanishing DOS, called Coulomb Gap (CG), so that inclusion of electron-electron interactions changes the exponent of Eq. (1) to $\frac{1}{2}$ regardless of dimensions and conduction is described by Efros-Shklovskii variable range hopping (ES-VRH):

$$\sigma(T) = \sigma_0 \exp\left(-\frac{T_0}{T}\right)^{\frac{1}{2}}, \text{ with } T_0 = T_{ES} = \frac{\beta e^2}{k_B \epsilon \epsilon_0 \xi} \quad (2)$$

where ϵ and ϵ_0 are the value for permittivity of vacuum and the dielectric constant of the material. The Coulomb gap energy would be calculated from:

$$E_{CG} = \frac{T_0}{\beta \sqrt{4\pi}} \quad (3)$$

As discussed above, The ES-VRH fits well the data at low bias regime. However, in a strong electric field ($E > E_C = \frac{2k_B T}{e \xi}$, where k_B is the Boltzmann constant, T is the temperature, e is the electron charge, and ξ is the localization length) the electrons participating in the hops acquire an energy necessary for executing hop, not due to the thermal phonons but rather due to the electric field. The conductivity in strong electric field no longer depends on the temperature (without an activation energy) and increase with increasing electric field in accordance with

$$\sigma(E) = \sigma_0 \exp\left(-\frac{E_{ES}}{E}\right)^{\frac{1}{2}} \text{ with } E_{ES} = \frac{k_B T_{ES}}{e \xi} \quad (4)$$

where, T_{ES} and ξ are the same parameters as in low bias Ohmic regime ES-VRH of Eq. 2 and $\sigma(E)$ is non-Ohmic conductivity at high electric field regime. ES-VRH is dominant at all temperature in highly disordered materials. On the other hand, in relatively low disordered samples, the carriers have enough energy to overcome *coulomb gap energy* at all measurable temperatures, which indicate that the DOS

near the Fermi energy level is practically constant. In that case, only Mott VRH will be dominant. At intermediate disorders sample, the transport is switched from ES to Mott VRH with increasing temperature in the same sample.

1.4 Thermoelectric Power

The thermoelectric effect was first observed by Estonian German physicist Thomas Johann Seebeck in early 1820. Thermoelectric power is very useful at probing electronic transport properties, which are intrinsic to the material. Resistivity measurement can be altered by material defects or grains but there do not affect thermoelectric power measurement. The microscopic mechanism of the TEP mostly depends on the carrier distribution under a temperature gradient. Fig. 1.12 shows that The heat is applied the end of the material, the temperature gradient arise on the material. The charge carriers at the hot end have lager kinetic energy and tend to diffuse to the cold end. Then the charge carriers start to re-distribute in response to a

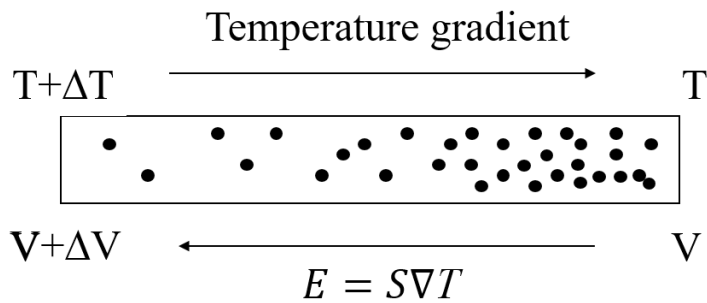


Figure 1.13 The schematic of redistribution of the carrier in response to the temperature gradient along the material.

temperature gradient and accumulation of the charge established an internal electric field (Fig. 1.13). The potential difference is proportional to the generated temperature difference as $\Delta V = S\Delta T$. The coefficient defines by the ratio the voltage deference to the temperature difference across the material, which is called as TEP, or the

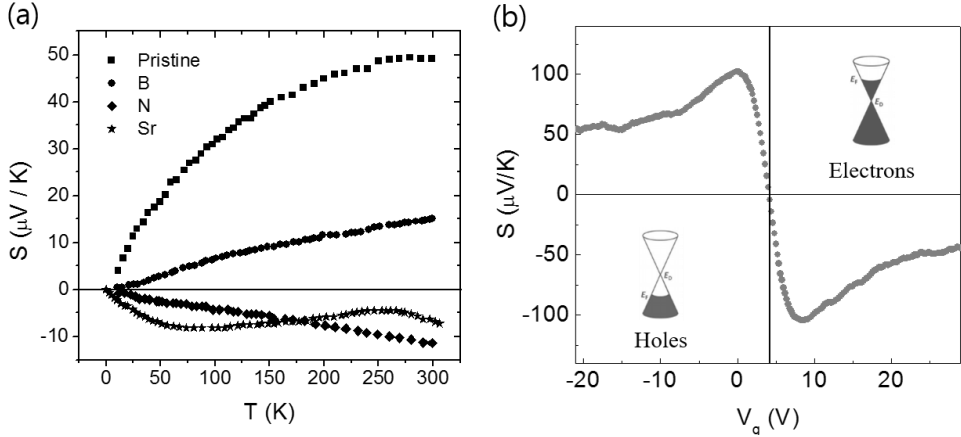


Figure 1.14 (a) The TEP of Doped multi wall carbon nanotubes, (b) The gate dependent TEP of single layer graphene

Seebeck coefficient, S . This depends on the electronic property of material. [49] The direction of induced electric field is determined by type of carrier. thus the sign of TEP is related to the type of dominant carrier, $S < 0$ for electrons, $S > 0$ for holes. So that TEP can probe major charge carrier in system. Figure 1.13 shows the TEP of doped multiwall nanotubes and gate dependent TEP of graphene. The sign of TEP in multiwall nanotubes has change depending on dopant. The sign of TEP in graphene is modulated adjusting Fermi level by gate voltage.

According to Boltzmann transport equation in metallic systems, the Mott formula for diffusion TEP can be derived as

$$S = -\frac{\pi^2}{3} \frac{k_B}{e} k_B T \left. \frac{\partial \ln \sigma(\varepsilon)}{\partial \varepsilon} \right|_{\varepsilon=\varepsilon_F} \quad (1)$$

Where k_B , e , T , σ and ε_F are the Boltzmann constant, the electron charge, temperature, electrical conductivity and Fermi energy, respectively. The diffusion TEP is proportional to the temperature.

On the other hand, The TEP in VRH system is derived as [50]

$$S = \frac{1}{3} \frac{k_B}{e} \frac{W^2}{k_B T} \left. \frac{\partial}{\partial \varepsilon} (\ln N(\varepsilon)) \right|_{\varepsilon=\varepsilon_F} \quad (2),$$

where W is the activation energy for hopping. $N(E)$ is density of state near the Fermi

energy. The activation energy of hopping depends on types of VRH. The activation energy of different VRH system is given by

$$W_{3D-VRH} = \frac{1}{4} k_B T \left(\frac{T_M}{T} \right)^{\frac{1}{4}}$$

$$W_{2D-VRH} = \frac{1}{3} k_B T \left(\frac{T_M}{T} \right)^{\frac{1}{3}}$$

$$W_{ES-VRH} = \frac{1}{2} k_B T \left(\frac{T_{ES}}{T} \right)^{\frac{1}{2}}$$

Therefore, the TEP of VRH for different system is

$$S_{3D-VRH} = \frac{1}{48} \left(\frac{k}{e} \right) k_B (T_M)^{\frac{1}{2}} (T)^{\frac{1}{2}} \frac{\partial(\ln N(\varepsilon))}{\partial \varepsilon} \Bigg|_{\varepsilon=\varepsilon_F}$$

$$S_{2D-VRH} = \frac{1}{27} \left(\frac{k}{e} \right) k_B (T_M)^{\frac{2}{3}} (T)^{\frac{1}{3}} \frac{\partial(\ln N(\varepsilon))}{\partial \varepsilon} \Bigg|_{\varepsilon=\varepsilon_F}$$

$$S_{ES-VRH} = \frac{1}{12} \left(\frac{k}{e} \right) k_B (T_{ES}) \frac{\partial(\ln N(\varepsilon))}{\partial \varepsilon} \Bigg|_{\varepsilon=\varepsilon_F}$$

The TEP of Mott VRH can be generalized as

$$S(T)_{VRH} \approx K_B T \left(\frac{T_M}{T} \right)^{\frac{2}{d+1}} \times \frac{\partial n(\varepsilon)}{\partial \varepsilon} \Bigg|_{\varepsilon=\varepsilon_F} \propto T^{\frac{d-1}{d+1}},$$

where d is dimension of systems. However, the presence of Coulomb gap is expected to become different TEP when the temperature is low enough such that $k_B T < E_{CG}$. Burns and Chaikin [51] argued that, TEP will remain constant value in the low-temperature as expressed

$$S(T)_{ES-VRH} \propto S_0$$

This theoretical prediction has been future confirmed by Ref [52]. However, this has never been confirmed by experiments.

Bibliography

- [1] K.S. Novoselov, D. Jiang, F. Schedin, T. Booth, V.V. Khotkevich, S.V. Morozov and A.K. Geim, Proc. Natl. Acad. Sci. USA **102**, 10451 (2005).
- [2] F. Xia, H. Wang, D. Xiao, M. Dubey and A. Ramasubramaniam, Nat. Photo. **8**, 899 (2014)
- [3] K.-A. N. Duerloo, Y.Li & E. J. Reed, Nat. Commu. **5**, 4214 (2014).
- [4] R. Kappera, D. Voiry, S. E. Yalcin, B. Branch, G. Gupta, A. D. Mohitr and M. Chhowalla, Nat. Mater. **13**, 1128 (2014).
- [5] A. K. Geim and K. S. Novoselov, Nat. Mater. **6**, 183 (2007).
- [6] Phaedon Avouris Nano Lett. **10**, 4286 (2010).
- [7] A. H. Castro Neto, F. Guinea, N. M. R. Peres, K. S. Novoselov, and A. K. Geim, Rev. Mod. Phys. **81**, 109 (2009).
- [8] X. Du, I. Skachko, A. Barker and E. Y. Andrei, Nat. Nanotech. **3**, 491 (2008).
- [9] Y. Zhang, Y.-W. Tan, H. L. Stormer and P. Kim, Nature **438**, 201 (2005).
- [10] N. Stander, B. Huard, and D. G.-Gordon, Phys. Rev. Lett. **102**, 026807 (2009).
- [11] S. Stankovich, D. A. Dikin, R. D. Piner, K. A. Kohlhaas, A. Kleinhammes, Y. Jia, Y. Wu, S. T. Nguyen and R. S. Ruoff, Carbon **45**, 1558 (2007).
- [12] S. Eigler, C. Dotzer, F. Hof, W. Bauer, A. Hirsch, Chem. Eur. J. **19**, 9490 (2013).
- [13] H. C. Schniepp, J.-L. Li, M. J. McAllister, H. Sai, M. H.-Alonso, D. H. Adamson, R. K. Prud'homme, R. Car, D. A. Saville and I. A. Aksay, J. Phys. Chem. B **110**, 8535 (2006).
- [14] G. Eda, G. Fanchini and M. Chhowalla, Nat. Nanotech. **3**, 270 (2008).
- [15] X. Wang, L. Zhi and K. Müllen, Nano Lett. **8**, 323 (2008).
- [16] Z. Yin, S. Sun, T. Salim, S. Wu, X. Huang, Q. He, Y. M. Lam and H. Zhang, ACS Nano **4**, 5263 (2010).
- [17] J. T. Robinson, F. K. Perkins, E.S. Snow, Z. Wei and P. E. Sheehan, Nano Lett. **8**, 3137 (2008).
- [18] M. Jin, H.-K. Jeong, W. J. Yu, D. J. Bae, B. R. Kang and Y. H. Lee, J. Phys. D: Appl. Phys. **42**, 135109 (2009).
- [19] Z. Lei, N. Christov and X. S. Zhao, Energy Environ. Sci. **4**, 1866 (2011).

- [20] H. Y. Jeong, J. Y. Kim, J. W. Kim, J. O. Hwang, J.-E. Kim, J. Y. Lee, T. H. Yoon, B. J. Cho, S. O. Kim, R. S. Ruoff and S.-Y. Choi, *Nano Lett.* **10**, 4381 (2010).
- [21] U. Martinez, J. H. Dumont, E. F. Holby, K. Artyushkova, G. M. Purdy, A. Singh, N. H. Mack, P. Atanassov, D. A. Cullen, K. L. More, M. Chhowalla, P. Zelenay, A. M. Dattelbaum, A. D. Mohite and G. Gupta, *Sci. Adv.* **2**, 1501178 (2016).
- [22] A. F. Wells, *Structural Inorganic Chemistry*, Oxford: Clarendon Press (1984).
- [23] X. Sun, Z. Wang, Z. Li and Y. Q. Fu, *Sci. Rep.* **6**, 26666 (2016).
- [24] Y.-C. Lin, D. O. Dumcenco, Y.-S. Huang and K. Suenaga, *Nat. Nanotech.* **9**, 391 (2014).
- [25] A. Kuc, N. Zibouche, and T. Heine, *Phys. Rev. B* **83**, 245213 (2011).
- [26] B. Radisavljevic, A. Radenovic, J. Brivio, V. Giacometti and A. Kis, *Nat. Nanotech.* **6**, 147 (2011).
- [27] M.-L. Tsai, S.-H. Su, J.-K. Chang, D.-S. Tsai, C.-H. Chen, C.-I Wu, L.-J. Li, L.-J. Chen and Jr-H. He, *ACS Nano* **8**, 8317, (2014).
- [28] H. Li, C. Tsai, A. L. Koh, L. Cai, A. W. Contryman, A. H. Fragapane, J. Zhao, H. S. Han, H. C. Manoharan, F. A.-Pedersen, J. K. Nørskov and Xiaolin Zheng, *Nat. Mater.* **15**, 48 (2016).
- [29] W. Wu, L. Wang, Y. Li, F. Zhang, L. Lin, S. Niu, D. Chenet, X. Zhang, Y. Hao, T. F. Heinz, J. Hone and Z. L. Wang, *Nature* **514**, 470 (2014).
- [30] Gardiner, D. J. *Practical Raman Spectroscopy*; Springer-Verlag: Berlin, (1989)
- [31] Y. Wang, Z. H. Ni, T. Yu, Z. X. Shen, H. M. Wang, Y.H. Wu, W. Chen, A. T. S. Wee, *J. Phys. Chem. C* **112**, 10637 (2008).
- [32] J. yan, Y. Zhang, P. Kim, and A. Pinczuk, *Phys. Rev. Lett.* **98**, 166802 (2007)
- [33] R. Saito, A. Jorio, A. G. Souza Filho, G. Dresselhaus, M. S. Dresselhaus and M. A. Pimenta, *Phys. Rev. Lett.* **88**, 027401 (2001).
- [34] A. Eckmann, A. Felten, I. Verzhbiskiy, R. Davey and C. Casiraghi, *Phys. Rev. B* **88**, 035426 (2013).
- [35] S.H. Huh (Ed.) S. Mikhailov (Ed.), Thermal reduction of graphene oxide, Physics and applications of graphene-experiments, InTech pp., 73–83 (2011).
- [36] S. Eigler, C. Dotzer and A. Hirsch, *Carbon* **50**, 3666 (2012).
- [37] J. Verble and T. Wieting, *Phys. Rev. Lett.* **25**, 362 (1970).

- [38] G. Frey, R. Tenne, M. Matthews, M. Dresselhaus, and G. Dresselhaus, Phys. Rev. B **60**, 2883 (1999).
- [39] C. Lee, H. Yan, L. E. Brus, T. F. Heinz, J. Hone and S. Ryu, ACS Nano **4**, 2695 (2010).
- [40] B. H. Kim, M. Park, M. Lee, S. J. Baek, H. Y. Jeong, M. Choi, S. J. Chang, W. G. Hong, T. K. Kim, H. R. Moon, Y. W. Park, N. Park and Y. Jun, RSC Adv. **3**, 18424 (2013).
- [41] H. Li, Q. Zhang, C. C. R. Yap, B. K. Tay, T. H. T. Edwin, A. Olivier and D. Baillargeat, Adv. Funct. Mater. **22**, 1385 (2012).
- [42] A. M.-Sánchez and L. Wirtz, Phys. Rev. B **85**, 155413 (2011).
- [43] C. Rice, R. J. Young, R. Zan, U. Bangert, D. Wolverson, T. Georgiou, R. Jalil, and K. S. Novoselov, Phys. Rev. B **87**, 081307 (2013).
- [44] B. Chakraborty, A. Bera, D. V. S. Muthu, S. Bhowmick, U. V. Waghmare and A. K. Sood, Phys. Rev. B **85**, 161403 (2012).
- [45] Y. Shi, J.-K. Huang, L. Jin, Y.-T. Hsu, S. F. Yu, L.-J. Li and H. Y. Yang, Sci. Rep. **3**, 1839 (2013).
- [46] N.F. Mott. Conduction in non-crystalline materials, localized states in a pseudogap and near extremities of conduction and valence bands on crystalline materials, localized states. Philosophical Magazine, 19:835–852, 1969.
- [47] B. I. Shklovskii and A. L. Efros. Electronic properties of doped semiconductors (Springer-Verlag, Berlin, 1984).
- [48] A.V Dvurechenskii, V. A. Drain and A. I. Yakimov, J. Exp. Theor. Phys. Lett. **48**, 155 (1988).
- [49] F. J Blatt, P. A. Schroeder, C. L. Foiles and D. Greig. Thermoelectric power of metal, (Springer Science & Business Media, 2012).
- [50] N. F. Mott and E. A. Davis. Electronic Processes in Non-Crystalline Materials. (Oxford University Press, 1979).
- [51] M. J. Burns and P. M. Chaikin, J. Phys. C: Solid State Phys. **18**, L743 (1985).
- [52] N. V. Lien and D. D. Toi, Phys. Lett. A **261**, 108 (1999).

Chapter 2

Formation of Graphene *p-n* junction by selective hydrogen adsorption

2.1 Introduction

Graphene, a single sheet of carbon with a two-dimensional honeycomb lattice, exhibits unique electronic properties such as the fractional quantum Hall effect, high carrier mobility, Klein tunneling, and ballistic transport [1-4] that make it a fascinating material for research and next generation electronic devices. However, to achieve graphene-based electronic devices, the modulation of the electronic band structure such as the gap opening and the *n*- and *p*- type properties in single graphene must be required. Recently, various methods have been used to engineer the carrier density and electronic structure of graphene [5-9]. The *p-n* junction in graphene also needs to be produced because *p-n* junctions have an important role in modern electronic devices. It has been produced by chemical doping and double gating [10-19]. However, a graphene *p-n* junction produced by chemical doping causes the degradation of devices such as carrier mobility. In the case of *p-n* junctions using the electrostatic gating method, the complex fabrication steps are indispensable. Hence, both methods are not appropriate for industrial application at this stage. In light of

this, it is highly desirable to find other methods which can overcome this limitation. One good candidate for controlling the electronic properties of graphene is dissociative hydrogen adsorption [20]. The hydrogen molecule breaks the C=C bond in graphene and produces two unpaired electrons. Finally, one electron participates in the formation of a C-H bond on the graphene, and the other electron is delocalized. This leads to the *n*-type doping of graphene.

In this chapter, we present a simple method to demonstrate local doping on single-layer graphene by means of selective H₂ exposure. This is achieved by fabricating a poly methyl methacrylate (PMMA) window on half of the graphene. The gate-voltage (V_G) dependent resistance of the single-layer graphene was measured as a function of the H₂ (12 bars) exposure time at 350 K. The charge neutrality point (CNP) of the uncovered area is significantly shifted toward the negative V_G region with an increase in the exposure time. However, the CNP in the PMMA-covered region did not shift prominently. Consequently, we show that a *p-n* junction on single-layer graphene can be obtained by selective hydrogen exposure.

2.2 Experimental details

The single layer graphene obtained by micromechanical cleavage was identified using color contrast with optical microscopy and confirmed by 2D and the *G* peaks from Raman spectroscopy (LabRam 300 with a 532 nm laser line of less than 0.5 mW, JY-Horiba). The field effect transistor is made with standard electron beam lithography (VEGA MM5150 with a 30 keV filament, Tescan). The electrodes (Cr/Au 5 nm/60 nm) is defined by e-beam evaporation and the lift-off process in acetone and IPA. A highly doped silicon substrate was used as the global back gate. The electrical measurement is done with a semiconductor parameter analyzer (4200-SCS, Keithley) in a homemade high-pressure and high-vacuum chamber.

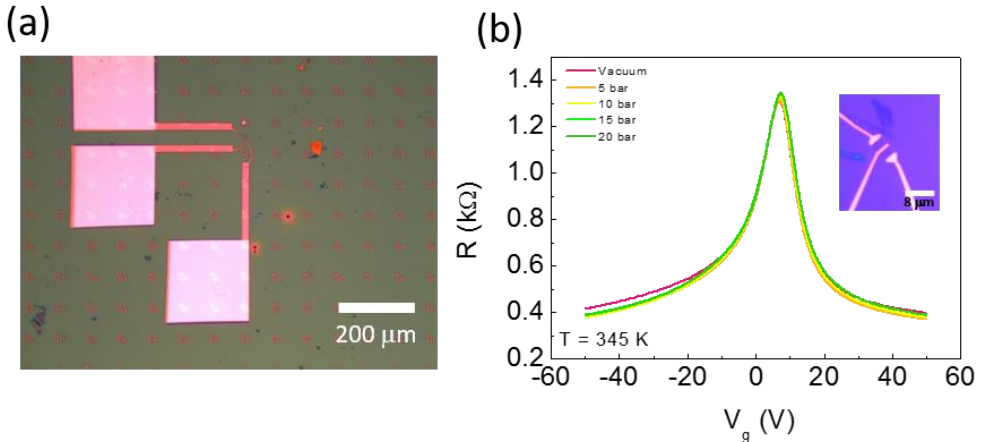


Figure 2.1 (a) Optical image of graphene device fabricated covered with PMMA. (b) Transfer curve of PMMA covered graphene device. Inset is a magnification of a fabricated device in figure (a)

The single-layer graphene obtained by micromechanical cleavage from highly oriented pyrolytic graphite (HOPG) is transferred onto the top of a highly *p*-doped silicon (100) wafer with 300 nm thermally grown SiO₂. The substrate is coated with copolymer and PMMA for electron beam lithography resist. Third, the electrode pattern is done by standard electron beam lithography and Cr/Au were deposited by e-beam and thermal evaporation. Finally, 200 nm of PMMA (950,000 g/mol) was spin-coated on the device. Before fabricating PMMA window on graphene device, we checked penetration of hydrogen through PMMA. PMMA have a free volume, which can be modulated by temperature and pressure [20]. So that, hydrogen may penetrate depending on molecular weight and thickness of PMMA [21]. We measured transfer characteristics of PMMA fully covered graphene device at hydrogen atmosphere. Figure 2.1 shows the transfer curve as a function of hydrogen pressure at 345 K. The no significant shift of CNP is observed as increase hydrogen pressure, indicating that hydrogen cannot penetrate at this condition. Thus, a window on the half of graphene device was obtained with electron beam lithography. A change in color is observed in the window (Fig. 2.2 (b)). Figure 2.2 (a) shows the fabrication process of the PMMA window. The device was loaded into a high-pressure and high-vacuum chamber to investigate the variation in the electronic

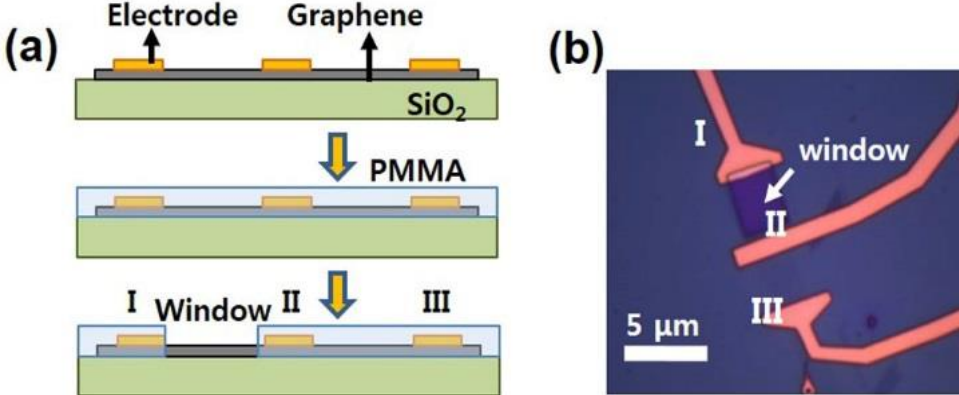


Figure 2.2. (a) Process for PMMA window fabrication. (b) The optical image of the PMMA window on single-layer graphene. I, II, and III indicate the three electrodes. structure in the graphene during hydrogen exposure [22], and thermal annealing at 393 K under high vacuum (1.0×10^{-6} torr) was performed overnight to remove water molecules and ad-molecules. Then, we measured the V_G -dependent resistance of the entire regions under high vacuum to verify the metal contact doping effect. The device was exposed to 12 bars of H₂ (99.9999 %) pressure at 350 K. Finally, the V_G -dependent resistance ($R(V_G)$) of the three regions of graphene, PMMA-window (between electrodes I and II in Fig. 2.2 (a)), PMMA-covered (between electrodes II and III), and the entire regions (between electrodes I and III), was measured.

2.3 Result and discussion

2.3.1 The transfer characteristics

The $R(V_G)$ of the device as a function of time under 12 bars of H₂ pressure at 350 K is shown in Fig. 2.3. We observe a decrease in the $R(V_G)$ as soon as the graphene was exposed to a H₂ atmosphere and a shift in the CNP toward the negative V_G region at both PMMA covered region and window region. As the H₂ exposure time increased, the shift in the CNP is enhanced; the $R(V_G)$ in the $V_G < V_{CNP}$ increased, and $R(V_G)$ in the $V_{CNP} < V_G$ decreased as described in a previous report [22]. This indicates that the hydrogen molecules are dissociated and adsorbed on the graphene and resulting

in the induction of the *n*-type doping effect on the graphene. The electron doping effect in the window region (Fig. 2.3 (a)) is larger than that in the PMMA-covered region (Fig. 2.3 (b)) on the graphene. The difference in mobility (slope in R vs V_G) between the two regions originates from the PMMA, which result in different effective dielectric constant [23]. Figure 2.4 demonstrate the kinetics of the interaction between graphene and H₂ in both PMMA covered region and window region. The temporal evolution of V_{CNP} can be described by a first order Langmuir adsorption model, $-\Delta V_{CNP} = -\Delta V_{CNP}^{Sat}(1 - e^{-t/\tau})$, where $-\Delta V_{CNP}^{Sat}$ and τ are the value of the saturated V_{CNP} and the kinetic coefficient, respectively. The Langmuir type adsorption model have been widely used to describe adsorption data obtained under non-equilibrium conditions. This type of adsorption model has been studied in single layer graphene and bilayer graphene irrespective of adsorbate such as H₂ [24], O₂ [25], NO₂ [26], NH₃ [27]. We can obtain the parameters of 12.3 V and 3.4 hr for

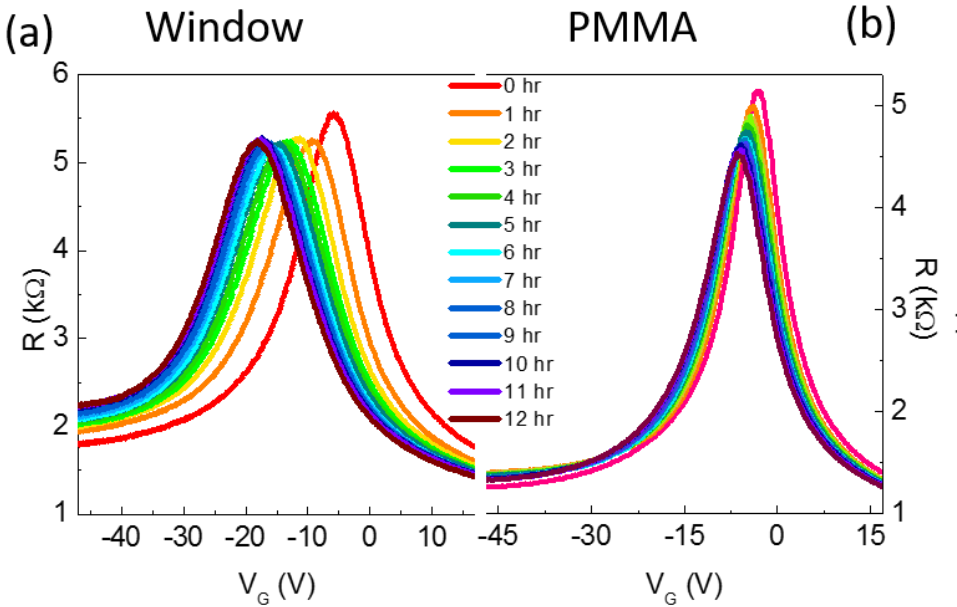


Figure 2.3 R(V_G) of the window (a) and PMMA-covered (b) regions as a function of the exposure time. The sample was exposed to 12 bars of H₂ pressure at 350 K.

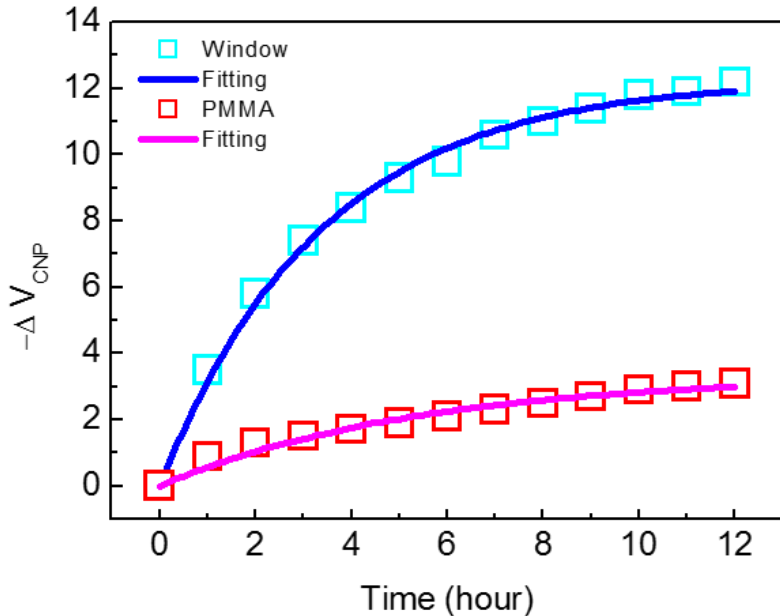


Figure 2.4 Shift in the CNP as a function of H₂ adsorption for two regions. CNPs for the window and PMMA-covered regions

window region and 3.4 V and 5.4 hr for PMMA covered region using fitting of each curves. The PMMA covered region is unexpectedly doped. because H₂ molecules are intercalated between graphene layer and SiO₂ substrate due to the roughness of SiO₂. The van der Waals interface (graphene on hexagonal boron nitride) can prevent substrate effects such as molecule intercalation, long range impurity [24].

Figure 2.5 (a) shows the transfer curve of before and after hydrogenation for window and PMMA covered region. The yellow green and blue curves are transfer curve of pristine sample and hydrogenated sample, respectively. The CNP in the PMMA covered region varied from -3.1 for 0 hr. to -6.2 V for 12 hr., while the CNP in the window region changed from -5.7 for 0 hr. to -17.9 V for 12 hr. we fitted the transfer curves to the transfer curve model for single layer graphene,

$$R = R_c + \frac{1}{e\mu} \left(\frac{L}{W} \right) \frac{1}{\sqrt{n^2 + n_0^2}}, \text{ where } R_c, e, \mu, L, W, n \text{ and } n_0 \text{ are the contact resistance,}$$

electron charge, length, width, mobility, carrier density and residual carrier density respectively [28]. The carrier density was extract from a two parallel

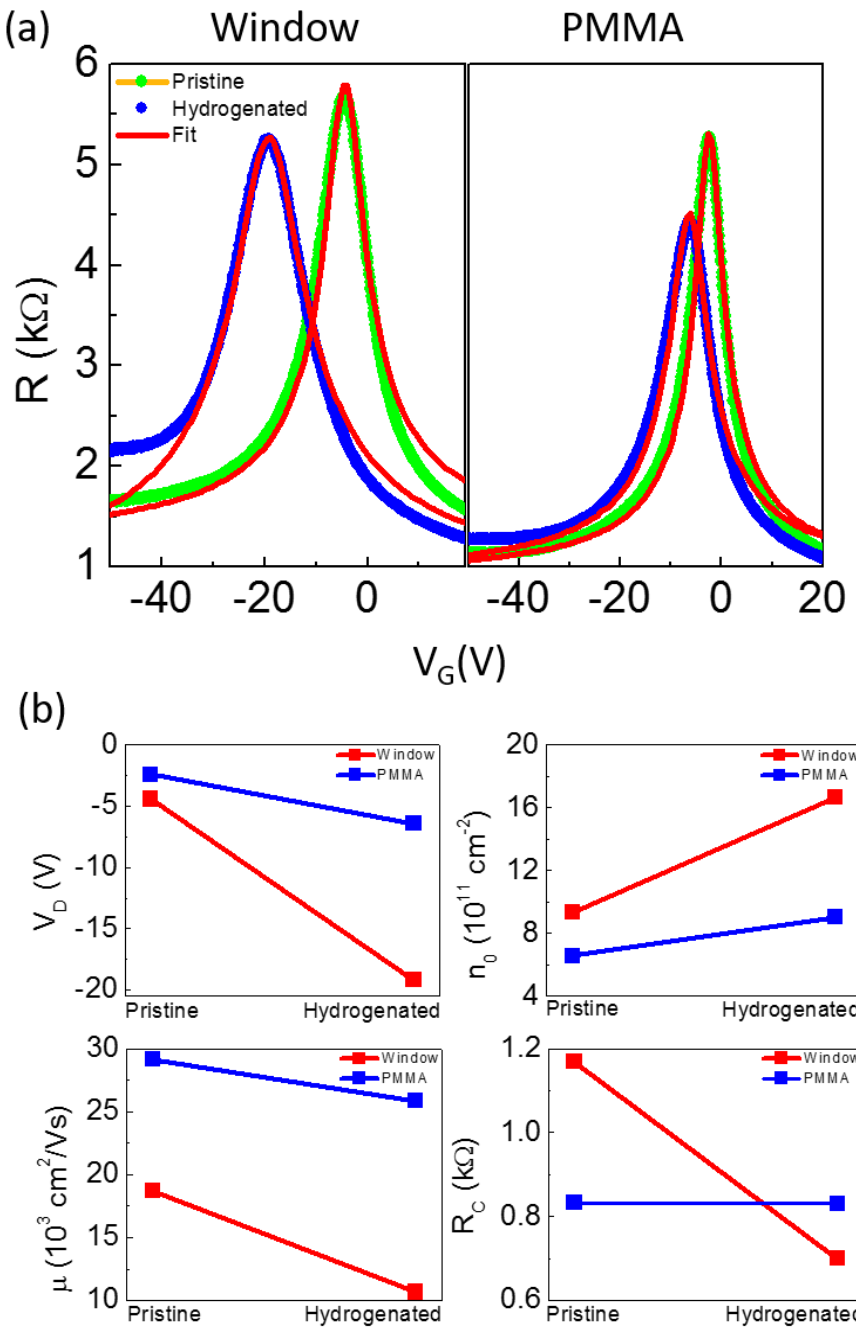


Figure 2.5 (a) Transfer curves of pristine sample and hydrogenated sample. The red lines are the fitting curves with the transfer curve model of single layer graphene. (b) The fitting parameters (charge neutrality point, residual carrier density, mobility, contact resistance) of pristine sample and hydrogenated sample for each region.

capacitor model, which is suitable for estimating the induced charge density,

$$n = \frac{\epsilon \epsilon_0}{ed} (V_G - V_{CNP}) = \alpha \Delta V_{BG}, \text{ where } V_{BG} \text{ is the CNP difference of pristine and}$$

hydrogenated sample charge neutrality point, and ϵ_0 the permittivity of vacuum, and $\epsilon = 3.9$ the permittivity of SiO_2 . α of 300 nm SiO_2 is $8 \times 10^{10} \text{ cm}^{-2}\text{V}^{-1}$. The parameter from fitting curves are plotted in Fig 2.5 (b). We figure out that The R_c and μ decrease after hydrogenation. On the contrary, the residual carriers increase and the CNP is shifted toward negative gate bias. The previous report shows that the hydrogen exposure to graphene affects the increase in the residual carrier density, which is related to the resistance at the CNP [22].

The modulations in the Fermi energy, $\epsilon_F = \hbar v_F \sqrt{\pi C V_G}$ where C is $7.2 \times 10^{10} \text{ cm}^{-2}/\text{V}$ for 285 nm of SiO_2 and the Fermi velocity v_F is $1 \times 10^8 \text{ cm/s}$, were 14.1 meV for the PMMA-covered region and 39.5 meV for the window region. $R(V_G)$ as a function of the exposure time between electrodes I and III (across the sample) was also measured (Fig. 2.6). At the moment of the H_2 exposure (0 hr.), only one peak (P_1) appeared as expected. However, another peak (P_2) gradually developed and

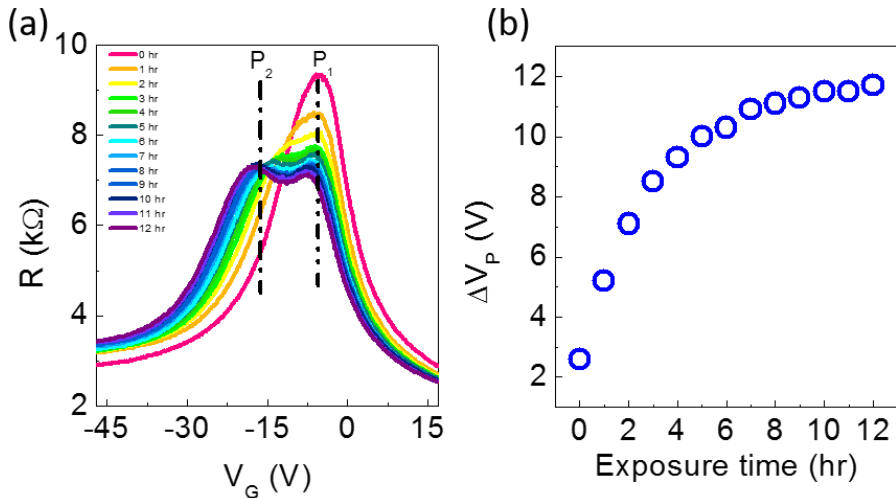


Figure 2.6 $R(V_G)$ between electrodes I and III. (a) As the exposure time increased, P_2 developed and became prominent, and (b) ΔV_P increased. This indicates that V_P in the window region shifts significantly to the negative V_G region compared with that in the PMMA-covered region.

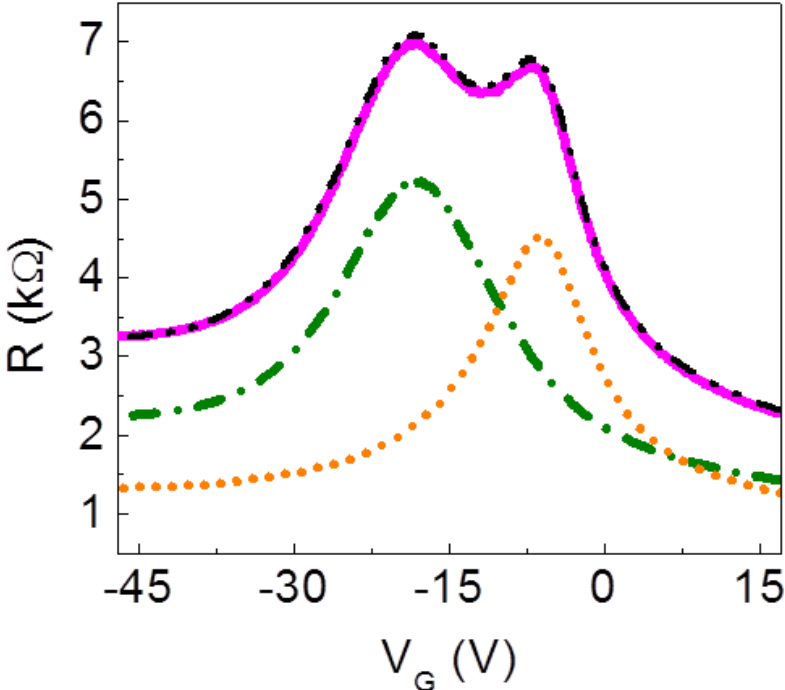


Figure 2.7 $R(V_G)$ s of the entire (between electrodes I and III, orange circles), PMMA-window (green dashed line), and the PMMA-covered (orange dotted line) regions. The superposition of $R(V_G)$ s (black dotted line) in the window and PMMA-covered regions is consistent

became prominent. Finally, two peaks are clearly observed (Fig. 2.6 (a)). Overall, the peaks decreased as the exposure time increased. In the case of the voltage for the peaks (V_P), P_1 at -4.6 V did not change significantly (-6.3 V after 12 hr. of exposure time). However, the shift in P_2 was prominent (from -12.1 to -17.4 V).

This can be confirmed by the difference in the two voltages for each peak (ΔV_P , Fig. 2.6 (b)). As the exposure time increased, the difference became larger. P_1 and P_2 originated from the interaction between the graphene and the hydrogen molecules in the PMMA-covered and window regions, respectively. To compare the peaks P_1 and P_2 with the peaks observed in the window and PMMA-covered regions, Figure 2.7 shows the $R(V_G)$ between electrode I and III obtained at 12 hr after the initial exposure to 12 bars of H₂. The orange dotted and green dashed lines represent the $R(V_G)$ in the PMMA-covered and window regions, respectively. The superposition

of these two peaks (black dotted line) is consistent with P_1 and P_2 . The small discrepancy could be due to contact between the electrodes and the graphene. However, the rectification of $I-V$ curves was not observed. It is well known that $I-V$ curve of a semiconductor p-n junction exhibits non-linear characteristics or rectifying behavior because of depletion region in the junction, but in case of graphene, depletion region could not be existed on the doped and undoped regions of graphene. Basically, $I-V$ curves of graphene show linear behavior for doped and undoped state due to the zero gap band structure. Hence, $p-n$ junction of graphene has not been demonstrated by $I-V$ curves. This is easily found in the previous reports on the graphene $p-n$ junction

2.3.2 Raman Spectroscopy

Figure 2.8 displays the Raman spectroscopy of the graphene before and after exposure to the H_2 pressure. Raman spectroscopy can provide information regarding defect and doping. The D peak near 1350 cm^{-1} is a breathing mode of A_{1g} symmetry, which is ascribed to the presence of disorder. The G peak near 1580 cm^{-1} is the in-plane stretching mode of sp^2 carbon. We measured the Raman spectra of the fabricated device and after 12 bars of H_2 exposure for 12 hr. at 350 K. under ambient condition. Figure 20 shows that the prepared sample is single layer graphene, that is, the $2D$ peak near 2700 cm^{-1} is larger than the G peak at 1580 cm^{-1} . In the PMMA-covered region (Fig. 2.8 (a)), the peaks developed at 1450 and 2950 cm^{-1} corresponding to the C-H bending and C-H stretching modes of the PMMA [27, 28]. After exposure to H_2 pressure, no significant change was observed in the PMMA-covered region. However, new peaks did develop in the window region but the peaks at approximately 1500 cm^{-1} and 2930 cm^{-1} can be interpreted by the C-H vibrations in the hydrogenated amorphous carbon [29] and the sp^3 C-H stretching mode [30], respectively. The relatively prominent peaks compared with the previous results [22] originate from the long exposure time. From the Raman spectra, we confirmed that

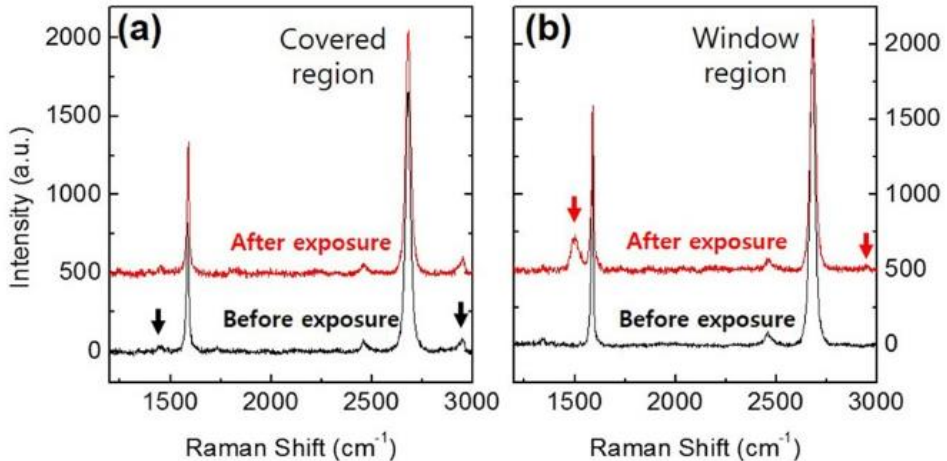


Figure 2.8 Raman spectroscopy of (a) the PMMA-covered and (b) window regions before (black line) and after (red line) exposure to 12 bars of H₂ pressure. The peaks designated by the black arrow in (a) are caused by PMMA. After exposure to H₂ pressure, two peaks pointed out with the red arrows in (b) developed, which were due to C-H vibrations.

the dissociated hydrogens bonded to carbon atoms in the window region as expected and that the thick PMMA effectively prevented interaction between the hydrogen molecules and the graphene.

2.4 Summary

In summary, we demonstrate local doping on single-layer graphene using selective adsorption of dissociative H₂ resulting from self-catalytic effect of graphene at low temperature. It was achieved with a PMMA window and fabricated with e-beam lithography. The CNP of the window region shifted prominently to a negative V_G compared with that of the PMMA-covered region. These results provide a facile method to modulate the electronic structure of graphene.

Bibliography

- [1] K. I. Bolotin, F. Ghahari, M. D. Shulman, H. L. Stormer, and P. Kim, *Nature* **462**, 196 (2009).
- [2] C. R. Dean, A. F. Young, I. Meric, C. Lee, L. Wang, S. Sorgenfrei, K. Watanabe, T. Taniguchi, P. Kim, K. L. Shepard, and J. Hone, *Nat. Nanotechnol.* **5**, 722 (2010).
- [3] A. F. Young and P. Kim, *Nat. Phys.* **5**, 222 (2009).
- [4] X. Du, I. Skachko, A. Barker and E. Y. Andrei, *Nat. Nanotechnol.* **3**, 491 (2008).
- [5] Z. Luo, N. J. Pinto, Y. Davila, and A. T. Charlie Johnson, *Appl. Phys. Lett.* **100**, 253108 (2012).
- [6] J. H. Chen, C. Jang, S. Adam, M. S. Fuhrer, E. D. Williams, and M. Ishigami, *Nat. Phys.* **4**, 377 (2008).
- [7] D. C. Elias, R. R. Nair, T. M. G. Mohiuddin, S. V. Morozov, P. Blake, M. P. Halsall, A. C. Ferrari, D. W. Boukhvalov, M. I. Katsnelson, A. K. Geim, and K. S. Novoselov, *Science* **323**, 610 (2009).
- [8] F. Chen, Q. Qing, J. Xia, J. Li, and N. Tao, *J. Am. Chem. Soc.* **131**, 9908 (2009).
- [9] T. Lohmann, K. von Klitzing, and J. H. Smet, *Nano Lett.* **9**, 1973 (2009).
- [10] E. C. Peters, E. J. H. Lee, M. Burghard and K. Kern, *App. Phys. Lett.* **97**, 193102 (2010).
- [11] D. B. Farmer, Y. M. Lin, A. Afzali-Ardakani, and P. Avouris, *Appl. Phys. Lett.* **94**, 213106 (2009).
- [12] K. Brenner and R. Murali, *Appl. Phys. Lett.* **96**, 063104 (2010).
- [13] J. R. Williams, L. DiGarlo, and C. M. Marcus, *Science* **317**, 638 (2007).

- [14] B. Özyilmaz, P. Jarillo-Herrero, D. Efetov, D.A. Abanin, L.S. Levitov, and P. Kim, Phys. Rev. Lett. **99**, 166804 (2007)
- [15] B. Huard, J. A. Sulpizio, N. Stander, K. Todd, B. Yang, and D. Goldhaber-Gordon, Phys. Rev. Lett. **98**, 236803 (2007).
- [16] G. Liu, J. Velasco, W. Z. Bao, and C. N. Lau, Appl. Phys. Lett. **92**, 203103 (2008).
- [17] J. F. Tian, L. A. Jauregui, G. Lopez, H. Cao, and Y. P. Chen, Appl. Phys. Lett. **96**, 263110 (2010).
- [18] Y. Nam, N. Lindvall, J. Sun, Y. W. Park, and A. Yurgens, Carbon **50**, 1987 (2012).
- [19] H.-Y. Chiu, V. Perebeinos, Y.-M. Lin, and P. Avouris, Nano Lett. **10**, 4634 (2010).
- [20] M. Schmidt and F. H. J. Maurer, J. Polym. Sci. Part B Polym. Phys. **36**, 1061 (1998).
- [21] K.-J. Jeon, H. Ri Moon, A. M. Ruminski, B. Jiang, C. Kisielowski, R. Bardhan and J. J. Urban, Nat. Mater. **10**, 286, (2011)
- [22] B. H. Kim, S. J. Hong, S. J. Baek, H. Y. Jeong, N. Park, M. Lee, S. W. Lee, M. Park, S. W. Chu, H. S. Shin, J. Lim, J. C. Lee, Y. Jun, and Y. W. Park, Sci. Rep. **2**, 690 (2012).
- [23] J. W. Suk, W. Hyoung Lee, J. Lee, H. Chou, R. D. Piner, Y. Hao, D. Akinwande, and R. S. Ruoff, Nano Lett. **13**, 1462 (2013).
- [24] S. J. Hong, H. Kang, M. Park, M. Lee, D. Soler-Delgado, D. H. Jeong, Y. W. Park and B. H. Kim, RSC Adv. **5**, 103276 (2015).
- [25] I. Silvestre, E. A. de Morais, A. O. Melo, L. C. Campos, A.-M. B. Goncalves, A. R. Cadore, A. S. Ferlauto, H. Chacham, M. S. C. Mazzoni and R. G. Lacerda, ACS Nano **7**, 6597 (2013).

- [26] G. Lee, G. Yang, A. Cho, J. W. Han and J. Kim, *Phys. Chem. Chem. Phys.* **18**, 14198 (2016).
- [27] S. Chen, W. Cai, D. Chen, Y. Ren, X. Li, Y. Zhu, J. Kang and R. S. Ruoff, *New J. Phys.* **12**, 125011. (2010).
- [28] S. Kim, J. Nah, I. Jo D. Sharjerdi, L. Colombo, Z. Yao, E. Tutuc, and S. K. Benerjee, *Appl. Phys. Lett.* **94**, 062107 (2009).
- [29] H.W. Choi, H. J. Woo, W. Hong, J. K. Kim, S. K. Lee, C. H. Eum, *Appl. Surface Sci.* **169**, 433 (2001).
- [30] K. J. Thomas, M. Sheeba, V. P. N. Nampoori, C. P. G. Vallabhan, P. Radhakrishnan, *J. Opt. A: Pure Appl. Opt.* **10**, 055303 (2008).
- [31] N. B. Cothup, L. H. Daly, S. E. Wiberley, *Introduction to infrared and Raman spectroscopy*. 3rd Ed. (Academic Press, La Vergne, LN, USA, 1988).
- [32] A. C. Ferrari and J. Robertson, *Phys. Rev. B* **64**, 075414 (2001).

Chapter 3

Electrical transport of reduced single layer graphene oxide and its hydrogenation

3.1 Introduction

Exotic electronic properties of graphene have attracted outstanding attention [1]. However, a lack of band gap has limited on the development of graphene based electronic device [2]. One method to overcome this limitation is making the defects, which is a useful tool to modify the electronic structure of graphene [3-5]. There have been two different approaches to obtain a disordered graphene by artificially controlling of disorder [6-9] and reduction of graphene oxide (GO) [10-12]. GO is hydrophilic and easily dispersible in water or conventional organic solvents due to the various oxygen functional groups (hydroxyl, epoxy, carbonyl, and carboxyl), which provide the electrically insulating and good processability as well [13]. The electrical properties of GO can be modified through chemical or thermal reduction. Reduction of GO gradually produces the randomly distributed crystalline domains of sp^2 carbons in nanometer size which are surrounded by the unreduced GO i.e., oxygen functional groups. Recently, several groups have investigated the charge transport of reduced GO (RGO), however, they explained the different charge transport behaviors, e. g. Mott variable range hopping (VRH) [15,16], Efros-

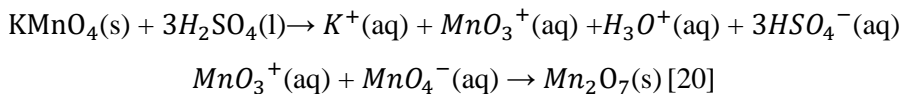
Shlovskii (ES)-VRH [17], and thermal activation [18]. However, these results were obtained with different sample geometry and different temperature range. There is no consensus on the dominant transport mechanism in RGO. The study of the charge transport mechanism of RGO is indispensable for not only understanding fundamental properties but also realizing its industrial applications.

In this chapter, we obtained large area single layer RGO by the bubble transfer method and the subsequent thermal reduction. We present the temperature dependence of resistance and thermoelectric power (TEP) as a function of gate voltage (V_g). The charge transport in the temperature range ($T < 70$ K) follows the ES-VRH model in the full range of V_g . With increase temperature, the conductivity become two dimensional (2D) VRH. The TEP shows that the two 2D Mott VRH is the main transport mechanism above $T = 50$ K.

3.2 Experimental details

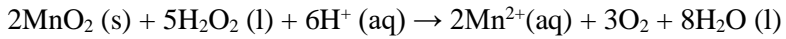
3.2.1 Synthesis of graphene oxide

Graphene oxide(GO) was prepared from natural graphite of chemical oxidization by modified Hummer's method [19]. 1g of expendable graphite (Qingdao Xinghe Graphite) and 1g of sodium nitrate were added into a 1000ml round flask surrounded with ice bath, keeping the temperature near 0 °C. in order to prevent rapid reaction. Then the 48 ml of sulfuric acid (H_2SO_4 sigma Aldrich 258105) was slowly added to the flask and it is stirred using magnetic stirrer with the speed of 400 rpm. 6g of potassium permanganate as a strong oxidant were slowly added into the flask and stirred for 1.5 hours. The ice bath should be maintained around 0°C during the oxidation since a lot of heat is generated when $KMnO_4$ is introduced into the suspension. The color of the mixture is changed from purple to green due to the formation of the Mn_2O_7 .



The ice bath was then removed, and the mixture was stirred at 35°C for 2 hr. It is

then diluted with slow and careful addition of 40 ml of distilled water drop by drop during 30 min maintain the ice bath. The reaction temperature was rapidly increase up to 98 °C with effervescence, and the color of mixture changed to purple. Further this suspension was diluted by adding additional 100 ml of distilled water stirred continuously. The solution is treated with hydrogen peroxide solution (H_2O_2 30 wt % in water) to eliminate bi-products such as unreacted oxidant.



The final mixture were transferred in tubes to centrifugation. The supernatant was removed after centrifugatin at 12000 rpm for 10 min. The bright yellowish color stat to appear and change to dark brownish color. It is clearly visible as divided a gel structure in the upper and precipitate at the bottom. The centrifugation repeated 6 ~7 times until pH of supernatant was reached around 7.

3.2.2 Preparation of single layer reduced graphene oxide

The bubble deposition method(BDM) is an easy technique to deposit flat and large GO onto arbitrary substrates, which enable to control the thickness of GO by multiple deposition [21]. Figure 3.1 shows a schematic representation of the deposition of GO with the BDM. The benefit of BDM is that when we deposit 2D material dispersed in solvents on to substrate by drop casting. It is difficult to obtain single and flat sample due to the aggregation and wrinkles. Using BDM, we can avoid this kind of issues. When we make a bubble contained GO flake, The GO membranes are flattened by surface tension on bubble surface. Then the flatten GO can be deposited onto the substrate without aggregation and wrinkles.

The mixture for BDM is prepared with GO solution and sodium dodecylbenzenesulfonates (SDBS) with 0.2 mg/ml of concentration. The concentration of SDBS in water should be less than critical micelle concentration. A piece of SiO_2/Si substrate is attached on the homemade stamp. the mixture of bubble is deposit in a close chamber using pipette and waiting few second to drain dens solution of on the bubble shown in Fig. 3.1 (a). Then, push the stamp to the

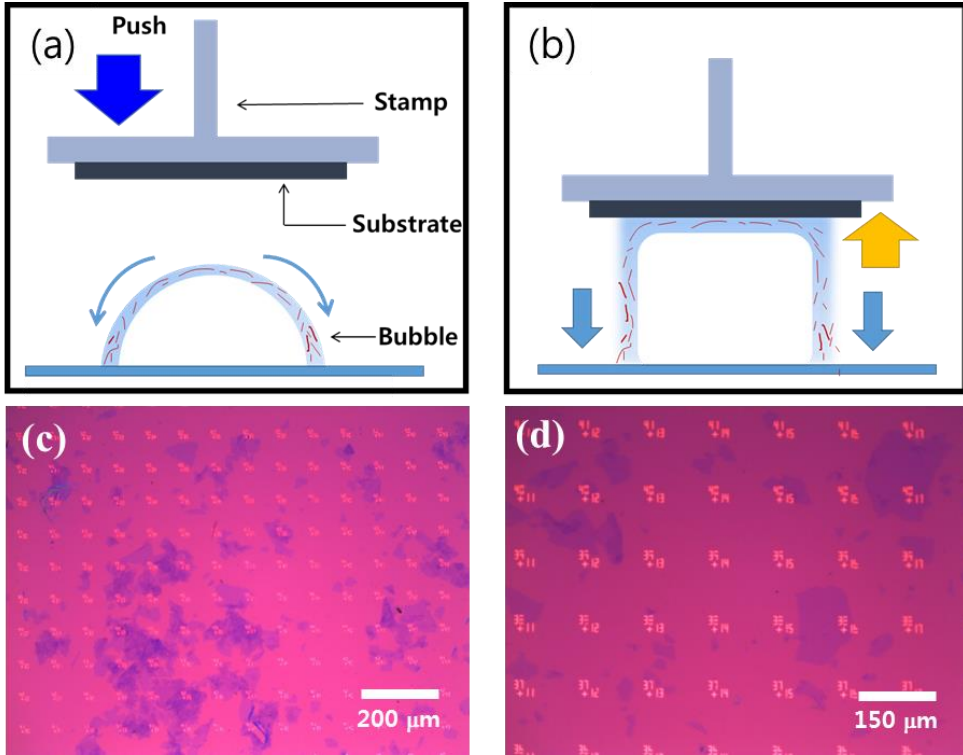


Figure 3.1 Schematic of the bubble deposition process and obtained sample by BPM
(a) After bubble formation, the water drains (blue arrows). (b) At the desired moment, the substrate is steadily lowered until the bubble film adheres to the substrate. (c)(d) deposited GO onto SiO_2/Si substrate

bubble and the GO is attached onto a substrate as shown in Fig. 3.1 (b). The residual water on substrate is quickly evaporated after bursting of the bubble. Finally, the substrate is washed using ethanol to remove SDBS. The deposited GO onto SiO_2 substrate is shown in Fig 3.1 (c), (d). The GO was reduced by thermal annealing at 1000 °C with H_2/Ar in order to prevent etching by detached oxygen. Then RGO was transferred using PMMA membrane on thermally grown SiO_2 /heavily p-doped Si Wafer substrate with pre-patterned alignment maker. The single layer RGO were selected by optical contrast using optical microscope. Rectangular shaped RGO was defined by conventional e-beam lithography and oxygen plasma etching. The two thermometer for probing temperature difference and micro-heater were fabricated using electron beam lithography followed by thermal evaporation (Cr 5 nm/ Au 50 nm) and a lift-off process in Acetone/IPA.

3.2.3 Transport measurement

The device was annealed at 180 °C in H₂/Ar flow for 12 hours to remove resist residue and decrease contact resistance prior to measurements. The Transport properties of RGO devise were studied in two terminal configurations. All measurements performed in 14 T superconducting magnet (Oxford Instruments) with pressure ($\sim 10^{-3}$ Torr) at temperature from 300 K to 1.6 K. Gate voltage dependent resistance and TEP was measured by DC method using semiconductor parameter analyzer (4200-SCS, Keithley Instrument) for the TEP measurement, a DC current is applied to the micro heater to create temperature gradient across the channel. Thermally induced voltage between two thermometers is measured using a semiconductor parameter analyzer as a function of gate voltage

3.3 Characterization (AFM, Raman, XPS)

We measured tapping mode of Atomic Force Microscopy (AFM), The thickness of RGO sheets is determined to be 1 nm shown in Fig. 3.2 (a). The 1 nm thick of RGO sheet is considered as a single-layer RGO sheet. X-ray photoelectron spectroscopy (XPS) is a powerful tool for studying chemical bonding. We utilized XPS to analyze the elemental composition of RGO. Figure 3.3 (a) show XPS spectrum of single

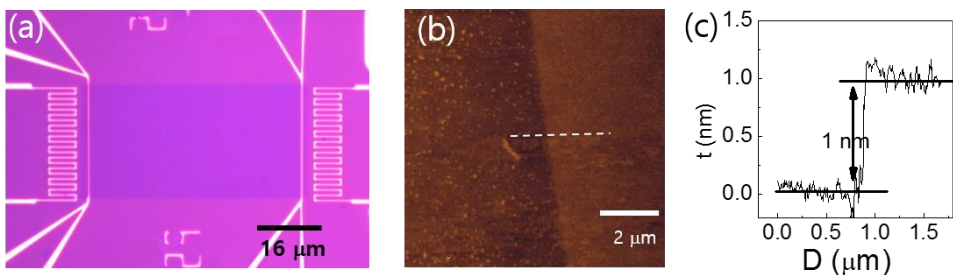


Figure 3.2 (a) Optical image of RGO device with micro-heater and two temperature sensors (or lead) (b) Tapping mode AFM image (C) The height profile of AFM image correspond to white dash line in (b)

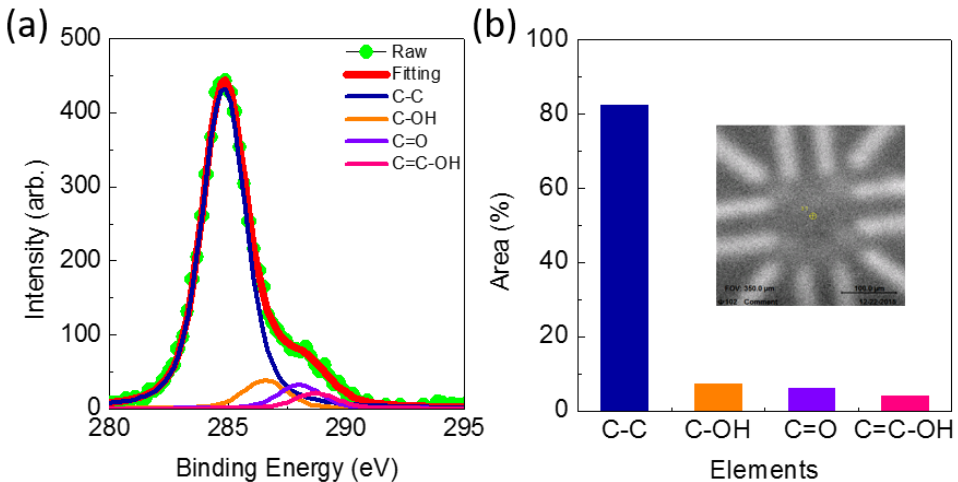


Figure 3.3 (a) XPS spectra for reduction efficiency of RGO and deconvolution of the C1's peaks. The green point is the measured point and solid lines are the deconvolution of the date. (b) The histogram of element content in RGO. Inset is the location of XPS measurement.

layer RGO with deconvolution of the C1s peak. After background subtraction, the XPS peaks were fitted to Voigt function. The deconvoluted peaks consist of the sp^2 carbon (C-C) at 284.6 eV, sp^3 hybridized carbon for hydroxyl (C-OH) at 286 eV, epoxide (C-O-C) at 286.2 eV, carbonyl (C=O) at 287.5 eV, and carboxyl acid (O=C-O) at 288.9 eV. The sp^2 carbon fraction was obtained by calculating the ratio of the integration of peak areas corresponding to each peak and contains are plotted in Fig. 3.3 (b). Graphene oxide usually contain 45 % of sp^2 carbon species [22,23]. After reduction at 1000 °C, the amount of C-C and C=C species increased by up to 82 %. Raman spectroscopy was carried out using a 532 nm laser wavelength with a power of 10 uW (LabRam 300 by JY-Horiba). Raman spectroscopy is a useful tool for characterization of carbon based materials. It gives an information related structures such as defect, disorder and degree of hybridization. The Raman spectra for GO and RGO are presented as Fig. 3.4. The Raman spectra of GO and ROG present representative peaks. The D peak near the 1340 cm^{-1} is A_{1g} breathing mode, which is attribute to presence of defect. The G peak near the 1585 cm^{-1} is E_{2g} vibrational in plane mode for sp^2 hybridization of carbon. The 2D peak near the 2700 is a two phonon vibration process, D+G mode near the 2940 cm^{-1} is a combination scattering

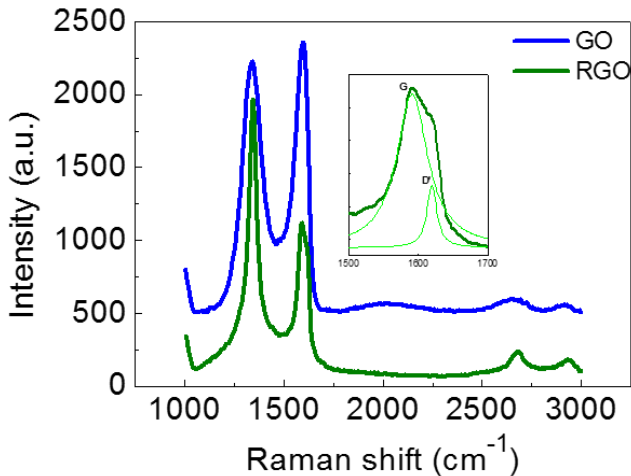


Figure 3.4 Raman spectra of before and after reduction. The insert shows deconvolution of G and D' peak

peak. The Raman spectra of sample has been changed significantly after reduction. The intensity of G peak significantly decreases as compare with D peak intensity and slightly developed D' peak near the 1620 cm^{-1} as shown insert of Fig. 3.4. The intensity of G peak and D+G peak have increased. The ratio of I_D/I_G and I_{2D}/I_G are used to evaluate the degree of disorder and recovering of graphitization in graphene based materials, respectively. [24]. After thermal reduction, we observed that the I_D/I_G ratio has increased to from 0.93 to 1.87, which indicate restoration of crystalline sp^2 carbon domain and decrease in the average size of sp^2 carbon domain upon thermal reduction. This result comes from that the removal of oxygen at high temperature leads to breaking of aromatic C=C bonds that cause the creation of disorder on the carbon structure like amorphous sp^2 network. I_{2D}/I_G ratio has increased from 0.04 to 0.16 which can be attributed to recovery of sp^2 carbon in graphitic structure. This observation is consistent with the previously reported literatures [25,26]. According to I_D/I_G ratio vs. distance between two defects (L_D) curves [27]. Analyzing I_D/I_G ratio and the full width at half-maximum (FWHM) is a good indicator for distance between two defects. The FWHM of G peak and D peak are 55 and 46 cm^{-1} , respectively. Moreover, the FWHM of 2D peak is 110 cm^{-1} . Thus, these values are corresponding to materials for the topologically disordered state “stage 2 region” [27] The L_D of the RGO can be estimated approximately 2 nm.

3.4 Result and discussion

3.4.1 Temperature dependence of conductance

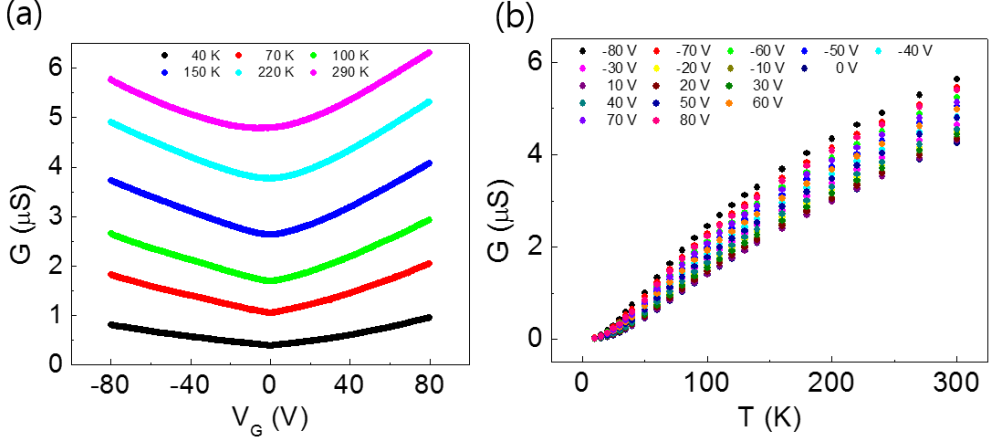


Figure 3.5 (a) The gate voltage dependence of conductance as a function of temperature (b) The temperature dependence of conductance extracted from transfer curve

We measured the gate dependent conductance (G) of the RGO as a function of temperature from 300 K to 10 K. at fixed source-drain voltage, $V_{DS} = 10$ mV. The source-drain voltage was determined from Ohmic regime from I - V curve. Since the linearity of I - V curve is disappeared below 10 K. we did not measure transfer characteristics below 10 K. Figure 3.5 (a) shows the representative transfer curve as a function of the temperature. Ambipolar transport is observed for all the temperature. In effort to determine charge transport mechanism, we extracted conductance at difference back-gate voltage plotted as a function of temperature in Fig. 3.5 (b). The decrease in conductance (resistance) at low temperature toward zero (infinite) is the general feature of transport in the strongly localized regime, where variable range hopping can occur. The conductance obeys the Mott VRH equation. The VRH model in the Ohmic regime can be described as a Mott relation, [28]

$$G(T) = G_0 \exp\left(-\frac{T_0}{T}\right)^p \quad \text{with } T_0 \equiv T_M = \frac{\beta}{k_B N(E_F) \zeta^2} \quad (1)$$

where G_0 is the high temperature limit of conductance, T_0 is Mott's characteristic temperature. The exponent p depends on the e spatial dimension of the systems or

the shape of the density of state (DOS). In 2D system the for a constant DOS at the Fermi energy level. The coulomb interaction between the localized states is neglected in Mott VRH conduction. However, the coulomb interactions are consisted in VRH system. The density of states near the Fermi level is diminish due to creating a soft gap vicinity of the Fermi energy level, called the Coulomb gap (CG) [29]. The hopping equation is governed by

$$G(T) = G_0 \exp\left(-\frac{T_{ES}}{T}\right)^{\frac{1}{2}} \text{ with } T_{ES} = \frac{\beta e^2}{4\pi\varepsilon\varepsilon_0 k_B \xi} \quad (2)$$

where β is a numerical constant with a value of 6.2 in 2D and 2.8 in 3D systems. For that, the accurate analysis is difficult due to the observation of the Mott VRH or ES-VRH at the same dimension and system. The determination of exponent (p) is the way to prevent this ambiguousness. We employed a method based on logarithmic derivation of reduced activation energy (W), introduced by Zbrodskii and Zinovera [30]. The W is expressed in the following equation.

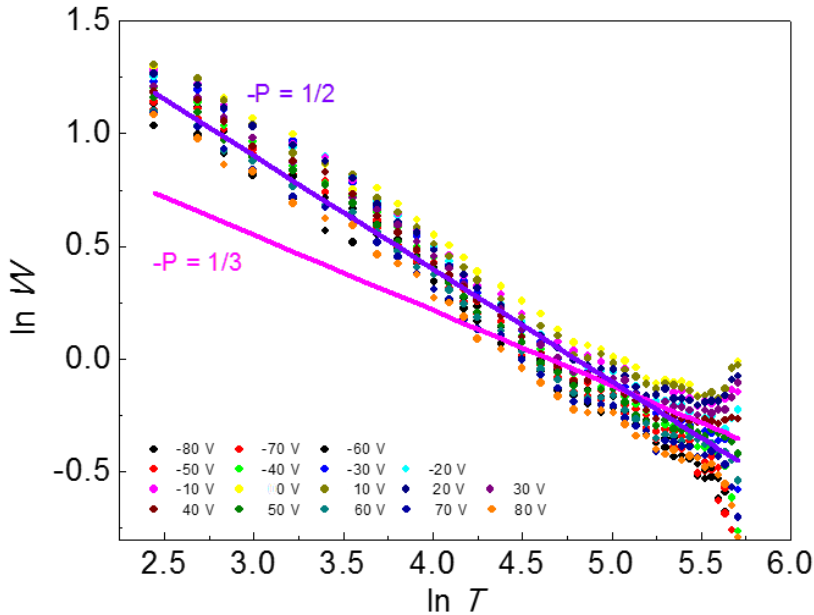


Figure 3.6 Reduced activation energy plotted versus temperature in a log-log scale for gate voltage and linear slope for 1/2 (violet) and 1/3 (pink)

$$W(T) = \frac{\partial \ln G}{\partial \ln T} = p \left(\frac{T_0}{T}\right)^p \quad (3)$$

, where the value of p can be obtained from the slope of $\ln W$ vs $\ln T$. Figure 3.6 shows the reduced activation energy at various temperatures on a log scale where the experimental data are plotted as a function of gate voltages. The linear solid violet line and pink line correspond to $p= 1/2$ and $p = 1/3$, respectively. The ES-VRH conduction is dominant at low temperature and The 2D Mott VRH is prominent

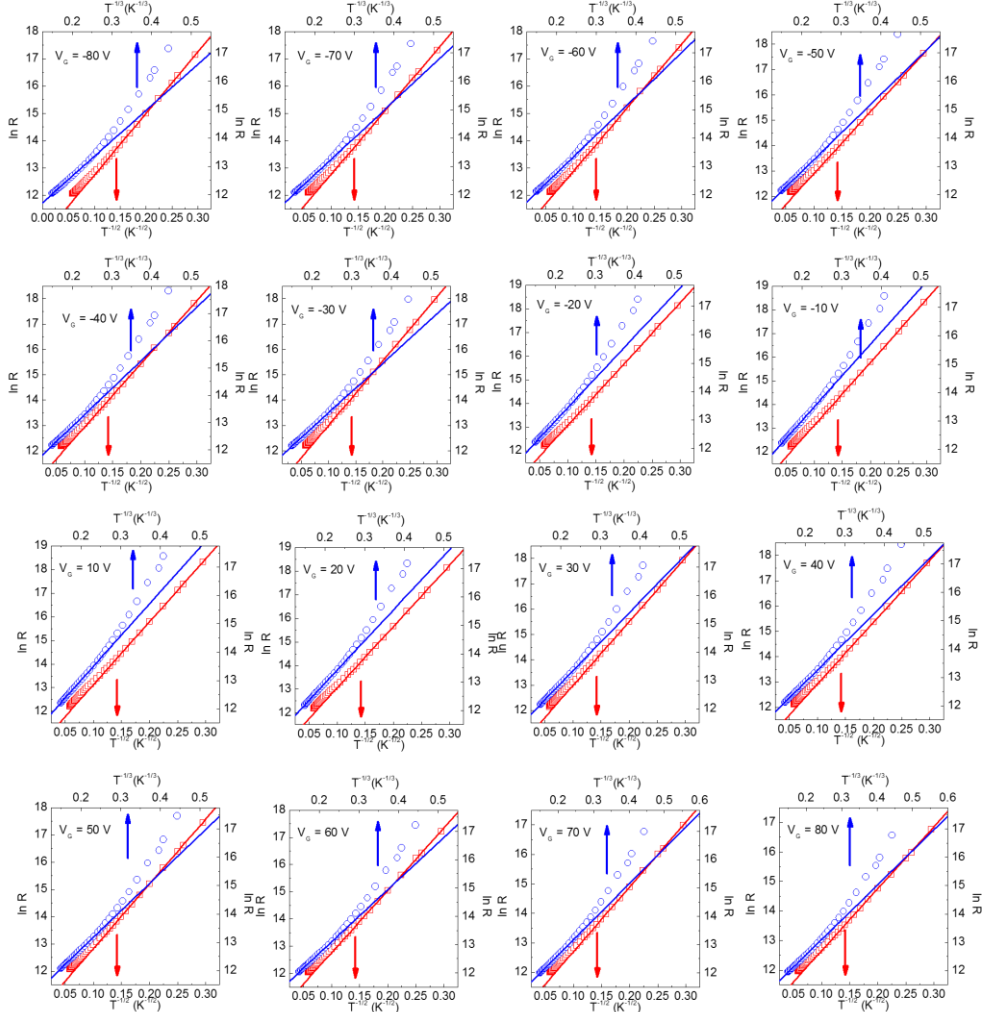


Figure 3.7 Electrical conductance of the RGO G VS $T^{-1/3}$ (blue dot) and $T^{-1/2}$ (red dot) for V_g . The red and blue solid line are a linear fit to the ES-VRH and 2D Mott VRH, respectively.

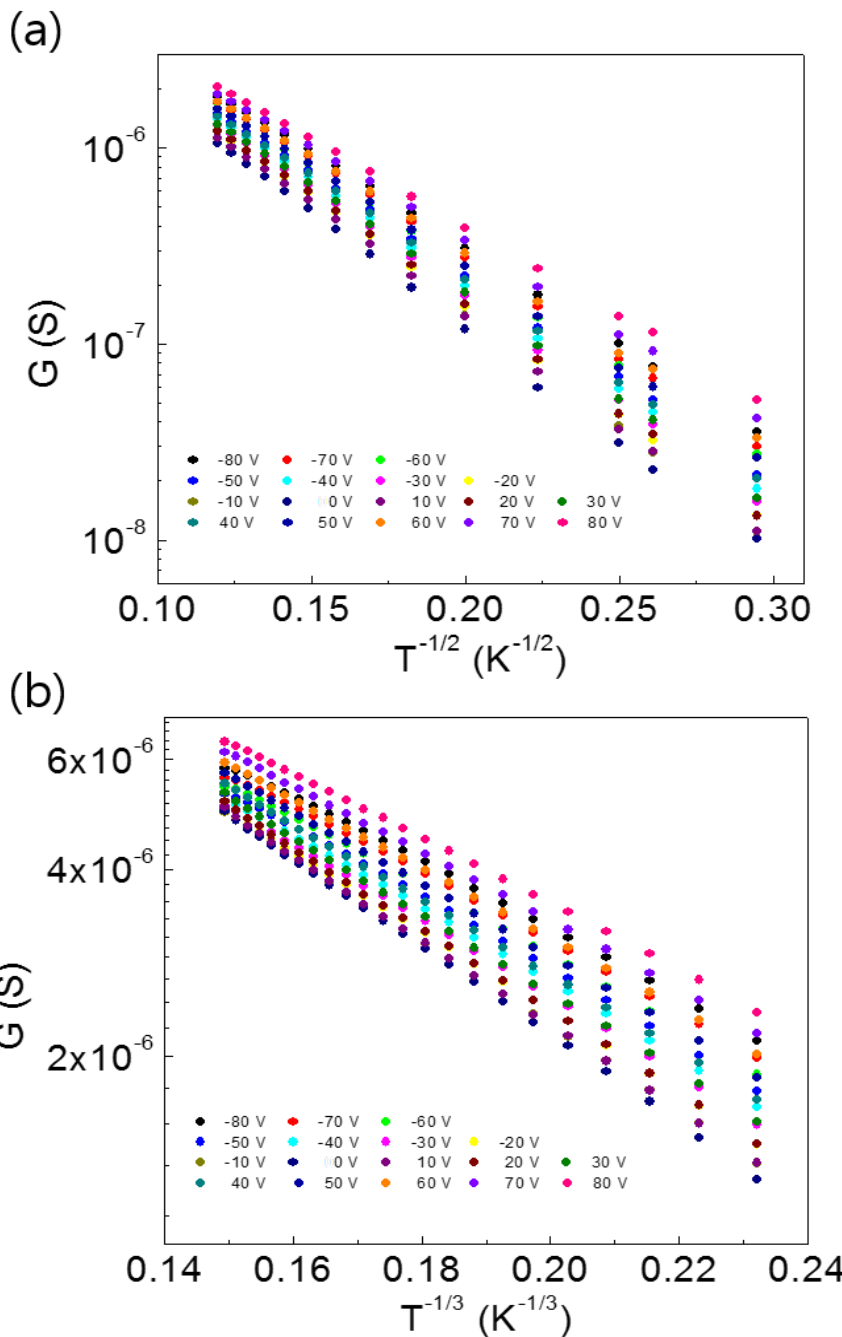


Figure 3.8 (a) semi-log scale plot of G vs $T^{-1/2}$ for different gate voltage in temperature of ($10\text{ K} < T < 70\text{ K}$) (b) semi-log scale plot of G vs $T^{-1/3}$ for different gate in temperature range of ($70\text{ K} < T < 300\text{ K}$)

charge transport mechanism at high temperature. If the thermal energy is higher than Coulomb gap energy ($k_B T \gg E_{CG}$) [31], the Coulomb interaction becomes negligible. As result, the charge transport is not affected by ES-VRH anymore. It is difficult to distinguish the accurate crossover temperature from Fig. 3.6. On this account, we plotted G vs $T^{-1/2}$ and $T^{-1/3}$ for all V_g . Figure 3.7 displays the conductance as a function of $T^{-1/2}$ (red square dot) and $T^{-1/3}$ (blue square dot) for different gate bias. The linear fittings of $\ln G$ to $T^{-1/2}$ and $T^{-1/3}$ are plotted as red solid line and blue solid line, respectively. The $\ln G$ to $T^{-1/2}$ is well fitted at low temperatures and then deviates near $65 \sim 70$ K. On the contrary, the fitting of $\ln G$ to $T^{-1/3}$ is well matched at high temperatures but it deviates near the 70 K. It is worth noting that the deviation temperature is almost same. It means that the crossover occurs at approximately 70 K. Figure 3.8 demonstrate the ES-VRH and 2D Mott-VRH behavior of $G(T)$, respectively. We can obtain the T_{ES} from the fitting of curves using Eq (2). The Coulomb gap energy (E_{CG}) is given by

$$E_{CG} = T_{TE} / \beta \sqrt{4\pi} \quad (4)$$

Figure 3.9 displays the E_{CG} values as a function of V_g . The E_{CG} is 32 K at $V_g = 0$ and

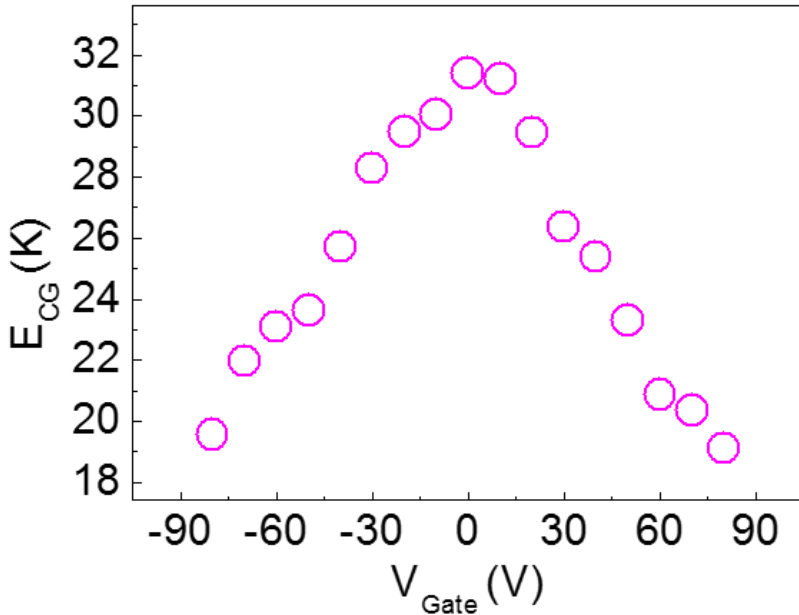


Figure 3.9 The E_{CG} vs gate voltage

it decreases as the magnitude of V_g increases. It is reasonable that E_{CG} is smaller than the crossover temperature because the thermal energy is to be larger than E_{CG} for the occurrence of crossover. The E_{CG} at $V_g = 0$ is suppressed with increasing positive and negative gate bias, which arises from the increase of overlapping of wave functions for localized electrons. The increase of overlap enlarges the domains of delocalized electrons and presumably screens the Coulomb interaction [32]. Reduction of E_{CG} at high carrier densities and switching of the ES-VRH to the Mott VRH have been reported in graphene antidot lattices [33]. Transition to the Mott-VRH is not observed presumably because the E_{CG} value of the RGO is much higher than that of antidote lattices. The ES-VRH behavior is further confirmed by the electric field dependence of conductance at high electric fields. The temperature dependence is strongly suppressed in the high electric field regime and follows the electric field dependence [34]

$$G(E) \sim \exp\left(-\frac{E_0}{E}\right)^{\frac{1}{2}} \text{ with } E_0 = \frac{k_B T_{ES}}{2e\xi} \quad (5)$$

where $G(E)$ is non-Ohmic conductance (dI/dV) in the high electric field regime. T_{ES} and ξ is equal to the value of the equation (2). It is valid at when the electric field is higher than a critical field, $E_C = 2k_B T / e\xi$ [35]. The Electric field dependence of conductance at 1.6 K as a function of gate bias is plotted in Fig 3.10 (a). We can

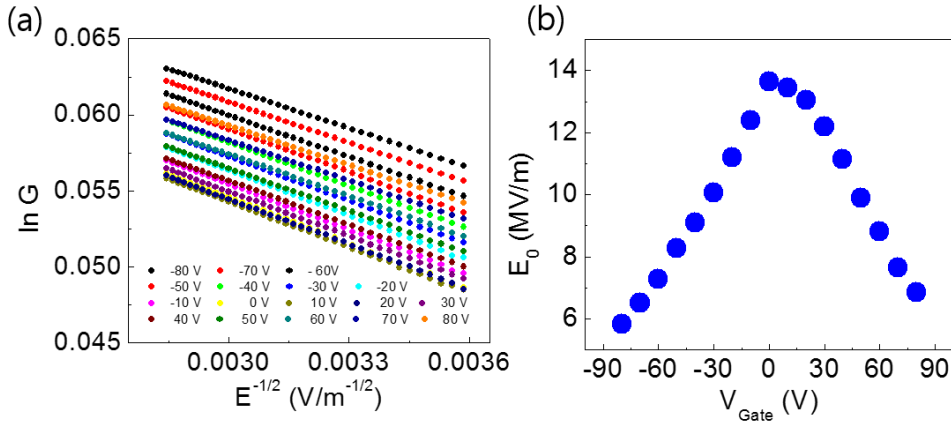


Figure 3.10 (a) $\ln G$ vs $E^{-1/2}$ for RGO device as a function of gates voltage at 1.6 K
(b) The calculated E_0 from Eq. (5)

observe the linear relation of $\ln G \sim E^{-1/2}$ plot. The E_0 is obtained from linear fitting of $\ln G \sim E^{-1/2}$ plot and plotted in Fig. 3.10 (b). The E_0 is reduced as increase gate voltage, which is consistent with previously calculated E_{CG} reduction from low-electric field linear regime.

The L_D of disordered graphene is a good indicator for estimating transport mechanism prior to transport measurement. The relation between L_D values and the transport mechanism has been studied in fluorination [36, 37], hydrogenation [38], ion beam irradiation [39, 40], and ozone treated [41] graphene and RGO [42]. In these literatures, 2D VRH and the ES-VRH have been reported with large (6.0 – 9.0 nm) and small (1.0 – 3.0 nm) values of L_D , respectively. With L_D larger than 9.0 nm, it was reported that the weak localization is dominant in graphene [38]. Therefore, L_D of 2.0 nm and the appearance of the ES-VRH in this study is consistent with the previous reports.

3.4.2 Thermoelectric Power

Figure 3.11 (a) shows the V_g dependence of TEP as a function of temperatures 50 K < T < 300 K. Typically, the sign of TEP of graphene is switched across the charge neutrality point (CNP). In addition, the sign of TEP is very sensitive to the kind of majority carrier [43]. The positive and negative values of TEP indicate that holes ($S > 0$) and electrons ($S < 0$) are the majority charge carriers, respectively. We observed that the magnitude of TEP increased regardless of the carrier type. It was reported that TEP increased with the increase of V_g near the Dirac point in graphene, which was interpreted by the result from the electron and hole puddle effect near the Dirac point [44]. Moreover, the broadening of peak to dip width in $S(V_g)$ was observed in the low mobility graphene, [45, 46] which is also related to electron and hole puddle effect due to disorder effect and charged impurity in graphene. In this regime, the compensated TEP can be expressed a simplified two-component model with carrier density of electron (n_e) and hole (n_h), as $S = S'(|n_h| - |n_e|)/(|n_h| + |n_e|)$ [47] where

the TEP increases from zero at the complete compensation as the density of majority carrier exceed that of the minority carrier. And then, the magnitude of TEP decreases as Fermi energy moves to degenerated states. However, the localized states due to the defects, impurities, and the electron-hole puddle are formed in broad bandwidth in RGO, where we observed the ES-VRH behaviors. Thus, the TEP maximum point is far from the CNP, which is not accessible in our V_g range.

Figure 3.11 (b) displays the temperature-dependent TEP, $S(T)$ with respect to V_g . The TEP follows 2D Mott VRH which is linear with respect to $T^{1/3}$. The temperature dependence of TEP in the Mott VRH is expressed [48]

$$S(T)_{Mott-VRH} \approx k_B T \left(\frac{T_M}{T}\right)^{\frac{2}{d+1}} \times \frac{dn(E_F)}{dE_F} \propto T^{\frac{d-1}{d+1}}$$

, where $n(E)$ is the density of states, d is dimensionality of the system.

We observed the 2D Mott VRH behavior in $G(T)$ within range of temperature ($70 \text{ K} < T < 300 \text{ K}$). This indicates that 2D VRH is the dominant conduction mechanism. The ES-VRH is prominent at low temperatures where thermal energy is smaller than the Coulomb gap. Furthermore, the E_{CG} estimated from temperature dependence of conductance was 32 K. Therefore, we conclude that the ES-VRH is dominant near 50 K and transition to the Mott's 2D VRH occurs at about 50 K.

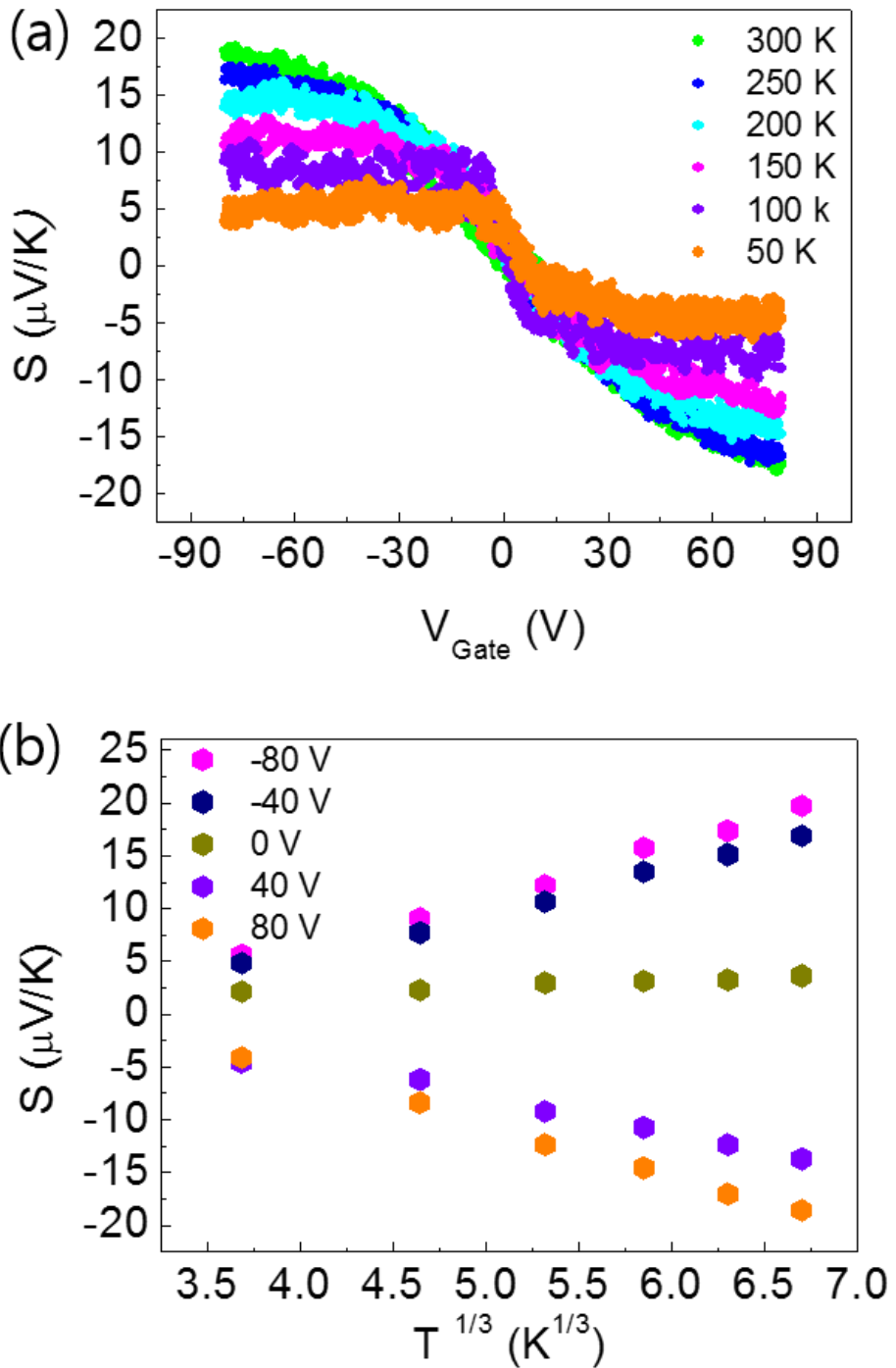


Figure 3.11 (a) TEP as a function of back gate voltage for $T=50, 100, 150, 200, 350$ and 300 K. (b) TEP vs $T^{1/3}$ for $V_G = -80, -40, 0, 40$ and 80 V

3.5 Hydrogenation

Figure 3.12 shows the transfer curve of RGO before (yellow green line) and after (pink line) hydrogenation. The CNP of pristine RGO is located at 9.4 V. After hydrogenation, the CNP is shifted toward -10.2 V, which indicates n-type doping result from hydrogen adsorption. Moreover, the maximum resistance of transfer curve decrease. The decrease in maximum resistance is explained by the improvement in reduction efficiency on annealing of RGO in hydrogen atmosphere. Since the hydrogen is reduction agent in GO thermal reduction [49]. We observed asymmetric mobility variation. It was attributed to the energy dependent scattering potential generated by adsorbates. The scattering potential suppresses mobility on one side of the CPN depending on the *n*- or *p*-type character of the dopant [50].

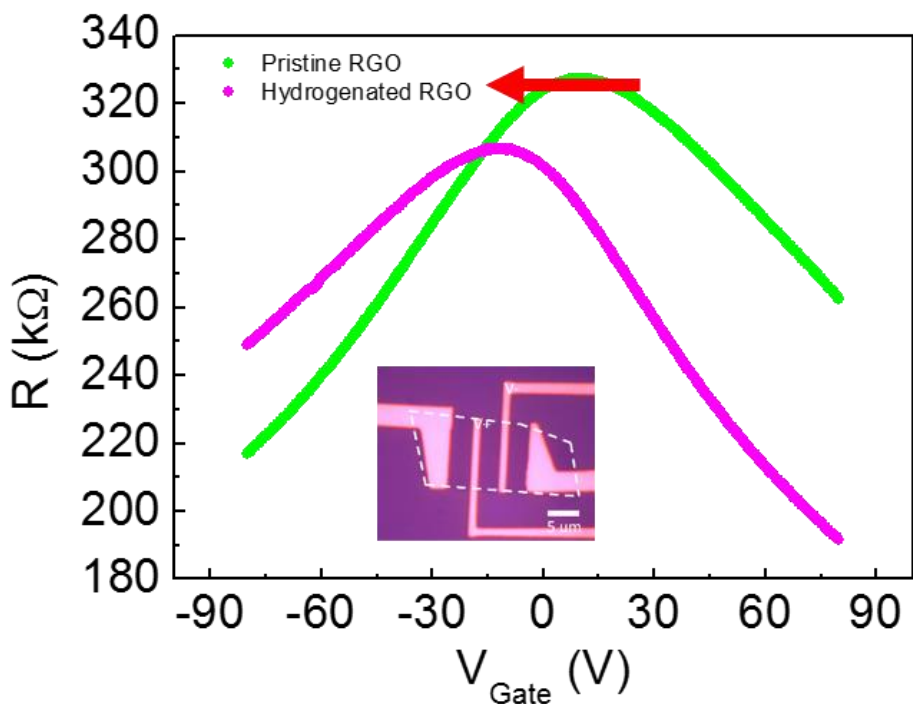


Figure 3.12 The transfer curve of RGO before and after hydrogen exposure. The yellow green line corresponds to pristine RGO. The pink line corresponds to hydrogen exposed RGO. Insert is optical image of device.

3.6 Summary

We observed change of Raman spectra upon thermal reduction of large area single layer GO, where the distance between defects of 2 nm is obtained from the analysis of Raman spectroscopy. The temperature dependence of Ohmic conductance follows the ES-VRH ($T < 70$ K) and 2D Mott-VRH ($T > 70$ K) where the size of the Coulomb gap decreases as the carrier density increases. The ES-VRH is further confirmed by the electric field dependence of non-Ohmic conductance which follows $G \sim \exp(-\frac{E_0}{E})^{\frac{1}{2}}$. The obtained E_0 is suppressed as increase gate voltage, which corresponds to E_{CG} . This reduction of E_0 is consistent with E_{CG} obtained from Ohmic regime. The gate voltage dependence of TEP indicates the broad bandwidth of the localized states. The ES-VRH is dominant below $T = 70$ K and 2D VRH is the main transport mechanism at temperatures 70 K $<$ T $<$ 300 K as confirmed by the temperature dependence of TEP. The hydrogen adsorption of RGO shows the n-type doping and conductivity enhancement due to improvement in reduction efficiency.

Bibliography

- [1] K. S. Novoselov, A. K. Geim, S. V. Morozov, D. Jiang, M. I. Katsnelson, I. V. Grigorieva, S. V. Dubonos and A. A. Firsov, *Nature* **438**, 197 (2005).
- [2] M. Y. Han, B. Özyilmaz, Y. Zhang, and P. Kim, *Phys. Rev. Lett.* **98**, 206805 (2007)
- [3] J. Haskins, A. Kinaci, C. Sevik, H. Sevincli, G. Cuniberti, and Tahir, *ACS Nano* **5**, 3779 (2011)
- [4] R. Balog, B. Jørgensen, L. Nilsson, M. Andersen, E. Rienks, M. Bianchi, M. Fanetti, E. Lægsgaard, A. Baraldi, S. Lizzit, Z. Sljivancanin, F. Besenbacher, B. Hammer, T. G. Pedersen, P. Hofmann and L. Hornekaer, *Nat. Mater* **9**, 315 (2010).
- [5] D. Haberer, D. V. Vyalikh, S. Taioli, B. Dora, M. Farjam, J. Fink, D. Marchenko, T. Pichler, K. Ziegler, S. Simonucci, M. S. Dresselhaus, M. Knupfer, B. Büchner and A. Grüneis, *Nano Lett.* **10**, 3360 (2010).
- [6] F. Withers, T. H. Bointon, M. Dubois, S. Russo and M. F. Craciun, *Nano Lett.* **11**, 3912 (2011).
- [7] D. Teweldebrhan and A. A. Balandin, *App. Phys. Lett.* **94**, 013101, (2009).
- [8] I. Childres, L. A Jauregui, J. Tian, and Y. P. Chen, *New J. Phys.* **13**, 025008 (2011).
- [9] P. Willke, J. A. Amani, A. Sinterhauf, S. Thakur, T. Kotzott, T. Druga, S. Weikert, K. Maiti, H. Hofsäss, and M. Wenderoth, *Nano Lett* **15**, 5110 (2015).
- [10] H. Huang, Z. Li, J. She and W. Wang, *J. App. Phys.* **111**, 054317 (2012).
- [11] I. Jung, D. A. Field, N. J. Clark, Y. Zhu, D. Yang, R. D. Piner, S. Stankovich, D. A. Dikin, H. Geisler, C. A. Ventrice Jr. and R.S. Ruoff, *J. Phys. Chem. C* **113**, 18480 (2009).

- [12] T. Tsuchiya, K. Terabe, M. Aono, *Adv. Mater.* **26**, 1087 (2013).
- [13] D. Li, M. B. Müller, S. Gilje, R. B. Kaner and G. G. Wallace, *Nat. Nanotech.* **3**, 101 (2008).
- [14] E. C. Mattson, H. Pu, S. Cui, M. A. Schofield, S. Rhim, G. Lu, M. J. Nasse, R. S. Ruoff, M. Weinert, M. Gajdardziska-Josifovska, J. Chen and C. J. Hirschmugl, *ACS Nano* **5**, 9710 (2011).
- [15] C. G.-Navarro, R. T. Weitz, A. M. Bittner, M. Scolari, A. Mews, M. Burghard, and K. Kern, *Nano Lett.* **7**, 3499 (2007).
- [16] A. B. Kaiser, C. Gómez-Navarro, R. S. Sundaram, M. Burghard and K. Kern, *Nano Lett.* **9**, 1787 (2009)
- [17] D. Joung and S. I Khondaker, *Rev. B* **86**, 235423 (2012)
- [18] S. Wang, P.-J. Chia, L.-L. Chua, L.-H. Zhao, R.-Q. Ping, S. Sivaramakrishnan, M. Zhou, R. G.-S. Goh, R. H. Friend, A.T.-S. Wee, and P. K.-H. Ho, *Adv. Mat.* **20**, 3440 (2008).
- [19] W.S. Hummers, JR, and R. E. Offeman, *J. Am. Chem. Soc.* **80**, 1339, (1985).
- [20] D.R. Dreyer, S. Park, C.W. Bielawski and R. S Ruoff, *Chem. SOC. Rev.* **39**, 228, (2010).
- [21] J. Azevedo, C. Costa-Coquelard, P. Jegou, T. Yu and J. J. Benattar, *J. Phys. Chem. C* **115**, 14678 (2011).
- [22] D. Zhan, Z. Ni, W. Chen, L. Sun, Z. Luo, L. Lai, T. Yu, A. T. S. Wee and Z. Shen, *Carbon* **49**, 1362 (2011).
- [23] S. J. Baek, W. G. Hong, M. Park, A. B. Kaiser, H. J. Kim, B. H. Kim and Y. W. Park, *Syn. Met.* **191**, 1 (2014).
- [24] A. C. Ferrari, *Solid State Commun.* **142**, 47 (2007).
- [25] X. Li, H. Wang, J.T. Robinson, H. Sanchez, G. Diankov and H. Dai, *J. Am. Chem. Soc.* **131**, 15939 (2009).

- [26] S.H. Huh (Ed.) S. Mikhailov (Ed.), InTech (2011), pp. 73–83
- [27] L. G. Cancado, A. Jorio, E. H. Martins Ferreira, F. Stavale, C. A. Achete, R. B. Capaz, M. V. O. Moutinho, A. Lombardo, T. S. Kulmala, and A. C. Ferrari, *Nano Lett.* **11**, 3190 (2011).
- [28] N. F. Mott & E. A. Davis "Electron Processes in Non-Crystalline Materials" (Clarendon, Oxford, 1979).
- [29] B. Shklovskii and A. Efros, 1984, Electronic Properties of Doped Semiconductors (Springer, Berlin).
- [30] A.G Zabrodskii and K.N. Ziov'eva, *J. Exp. Theor. Phys. Lett.* **59**, 525 (1984).
- [31] H. Li, A. Pourret and P. Guyot-Sionnest, *ACS Nano* **4**, 5211 (2010).
- [32] A.V. Dvurechenskii and A.I. Yakimov, *Zh. Eksp. Teor. Fiz.* **95**, 159 (1989).
- [33] A.J.M Giesbers, E. C. Peters, M. Burghard, and K. Kern, *Phys. Rev. B* **86**, 045445 (2012).
- [34] D. Yu, C. Wang, B. L. Wehrenberg and P. Guyot-Sionnest, *Phys. Rev. Lett.* **92**, 216802 (2004).
- [35] N. Apsley and H.P. Hughes, *Philos. Mag.* **31**, 1327 (1975).
- [36] F. Withers, M. Dubois and A. K. Savchenko, *Phys. Rev. B* **82**, 073403 (2010)
- [37] F. Withers, S. Russo, M. Dubois and M. F Craciun, *Nanoscale Res. Lett.* **6**, 526 (2011).
- [38] R. Jayasingha, A. Sherehiy, S.-Y. Wu and G. U. Sumanasekera, *Nano Lett.* **13**, 5098 (2013).
- [39] Y.-B. Zhou, Z.-M. Liao, Y.-F. Wang, G. S. Duesberg, J. Xu, Q. Fu, X.-S. Wu and D.-P. Yu, *J. Chem. Phys.* **133**, 234703 (2010).

- [40] E. Zion, A. Haran, A. V. Butenko, L. Wolfson, Y. Kaganovskii, T. Havdala, A. Sharoni, D. Naveh, V. Richter, M. Kaveh, E. Kogan, I. Shlimak, Graphene, **4**, 45 (2015).
- [41] J. Moser, H. Tao, S. Roche, F. Alzina, C. M. Sotomayor Torres and A. Bachtold, Phys. Rev. B **81**, 205445 (2010).
- [42] R. Negishi, M. Akabori, T. Ito, Y. Watanabe and Y. Kobayashi, Sci. Rep. **6**, 28936 (2016).
- [43] Y. M. Zuev, W. Chang and P. Kim, Phys. Rev. Lett. **102**, 096807 (2009).
- [44] P. Wei, W. Bao, Y. Pu, C. N. Lau and J. Shi, Phys. Rev. Lett. **102**, 166808 (2009).
- [45] J. Duan, X. Wang, X. Lai, G. Li, K. Watanabe, T. Taniguchi, M. Zebarjadi, E. Y. Andrei Proc. Natl. Acad. Sci. USA **113**, 14272 (2016).
- [46] X. Liu, D. Wang, P. Wei, L. Zhu and J. Shi, Phys. Rev. B **86**, 1554414 (2012).
- [47] E.H. Hwang, E. Rossi and S. D. Sarma, Phys. Rev. B **80**, 235415 (2009)
- [48] M. J. Burns and P. M. Chaikin, J. Phys. C: Solid State Phys. **18**, L743 (1985)
- [49] A. Bagri, C. Mattevi, M. Acik, Y. J. Chabal, M. Chhowalla and V. B. Shenoy, Nat. Chem. **2**, 581 (2010)
- [50] J. P. Robinson, H. Schomerus, L. Oroszlány, and V. I. Fal'ko, Phys. Rev. Lett. **101**, 196803 (2008)

Chapter 4

Effect of hydrogen on geometric and electronic structure of MoS₂

4.1 Introduction

In the past decade, two dimensional (2D) materials stacked by van der Waals force have attracted tremendous research interest due to its various novel properties and applicability of functional device [1,2]. Among them, graphene is representative material that has linear energy dispersion near the Fermi level, which results in exploring exotic electronic properties. However, the absence of band gap has limited its application as a semiconductor channel material in electronic device. In contrast to graphene, Molybdenum disulfide (MoS₂), a family of transition metal dichalcogenide, is semiconductor and have a sizeable band gap [3] as well as show outstanding properties such as high mobility ($\sim 10^3$ cm²/V·s), high on-off ratio ($\sim 10^6$) [4], high thermoelectric power ($\sim 10^{-3}$ V/K) [5], mechanical flexibility [6], large spin orbit coupling [7], and valley polarization [8] that make it a promising candidate as a building block for post silicon material in new generation. In addition to aforementioned attractiveness the single-layer, MoS₂ nanoparticles are also useful in terms of hydrodesulfurization (HDS) catalyst to remove sulfur compounds from crude oil [9]. In general, it has been accepted that the HDS with MoS₂ catalysts

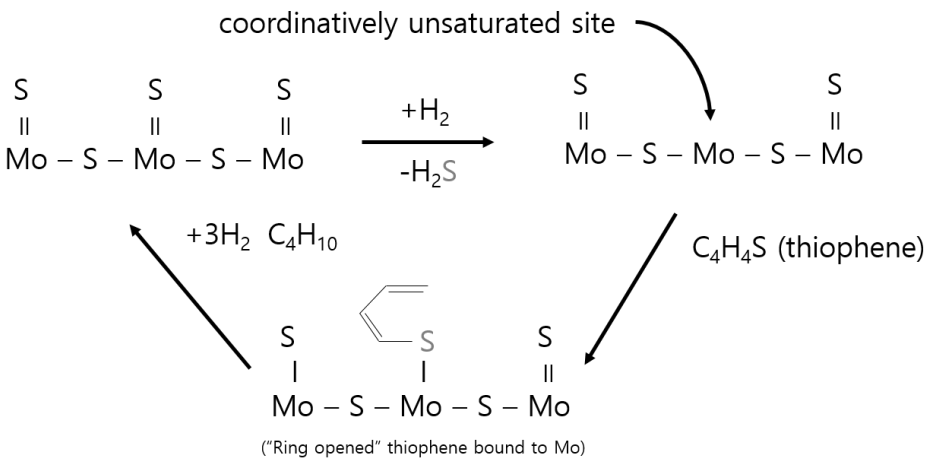


Figure 4.11 Simplified diagram of a HDS process for thiophene elimination

occurs by three steps (Fig. 4.1). First, molecular hydrogen is dissociatively adsorbed on MoS₂, inducing the coordinatively unsaturated site (CUS) by removing sulfur in the form of H₂S. Second, substrates, such as thiophene, are coordinatively bound to the CUS. Finally, hydrogenolysis is followed, which results in removing of sulfur from the substrates. In this light, molecular hydrogen plays an important role in HDS process because H₂ triggers the reaction. Since the CUS process generally progresses at high temperature ($T > 573$ K) and high H₂ pressure ($P_{H_2} > 30$ bar), most researches for the interaction between H₂ and MoS₂ have been done in high temperature with high H₂ pressure condition [10]. Notwithstanding these results, there is still the need in the fundamental properties, such as the electronic and structural change in MoS₂, the number of sulfur atoms removed, and the reaction temperature. It leads to demand for investigating the electronic property and structural modulation of MoS₂ upon exposure to low H₂ pressure at low temperature.

In this chapter, we have systematically studied the hydrogen effect on electronic properties of MoS₂. We measured the *in-situ* electrical measurement under the hydrogen atmosphere. Thermoelectric power (TEP) measurements of single-layer MoS₂ before and after hydrogen exposure. The transfer curve of the MoS₂ device was measured as a function of the H₂ exposure time at 350 K. We also measured the TEP and transfer curve simultaneously on the same device at 300 K before and after hydrogenation. The threshold voltage and peak of TEP of the MoS₂ device was significantly shifted toward the negative gate voltage after H₂ exposure, which

means the *n*-doping of MoS₂. Raman spectroscopy also provided an information regarding doping and structure modulations. We proved that hydrogenation and sulfur vacancy contribute to electron doping manipulation on MoS₂.

4.2 Experimental

Single-layer MoS₂ was obtained by mechanical cleavage of natural molybdenum disulfide single crystal (SPI supplies, USA) and then transferred onto a highly *p*-doped silicon substrate with a 285 nm of thermally grown SiO₂ layer. Monolayer was identified by optical microscope and confirmed with Raman spectroscopy. Electron beam lithography (VEGA MM5150, Tescan) followed by evaporation (ZZS550-2/D, Maestech) of (Cr/Au 5/60 nm) for outer electrode and (Au 50 nm) for inner lead were utilized to make the micro-heater, thermometer, probe. The optical image of device is shown in insert of Fig. 4.2. A home-made high-temperature and high-pressure chamber was used for hydrogenation. Prior to exposed to hydrogen, the devices were evacuated in a high vacuum ($\sim 10^{-6}$ torr) at 390 K for 12 hours to remove ad-molecules and make better electrical contact of device. The transfer characteristics of MoS₂ device were measured by the three-terminal DC method using Keithley 4200-SCS semiconductor characterization system under H₂ atmosphere at a pressure of 12 bar (99.9999 %) at 350 K. The source-drain bias voltage was fixed to 10 mV and then electrical current was measured as a function of gate bias voltage with 0.1 V/s speed. TEP measurements are carried out using a EG&G 5210 lock-in amplifier and Keithley 6517A for gate bias at 300 K. An AC current with the low frequency $\omega = 1.333$ Hz is applied to generate a temperature difference across the sample by Joule heating. A thermally induced 2ω voltage drop is measured between the two thermometer by lock in amplifier. The temperature gradient across the channel area by measuring four probe resistance of the two thermometer using delta mode of Keithley 6221 and 2182. The TEP of the MoS₂ sample is calculated from $S = -\Delta V/\Delta T$. Raman spectroscopy was carried out using a 532 nm laser wavelength with 10 μ W of power (LabRam 300 by JY-Horiba).

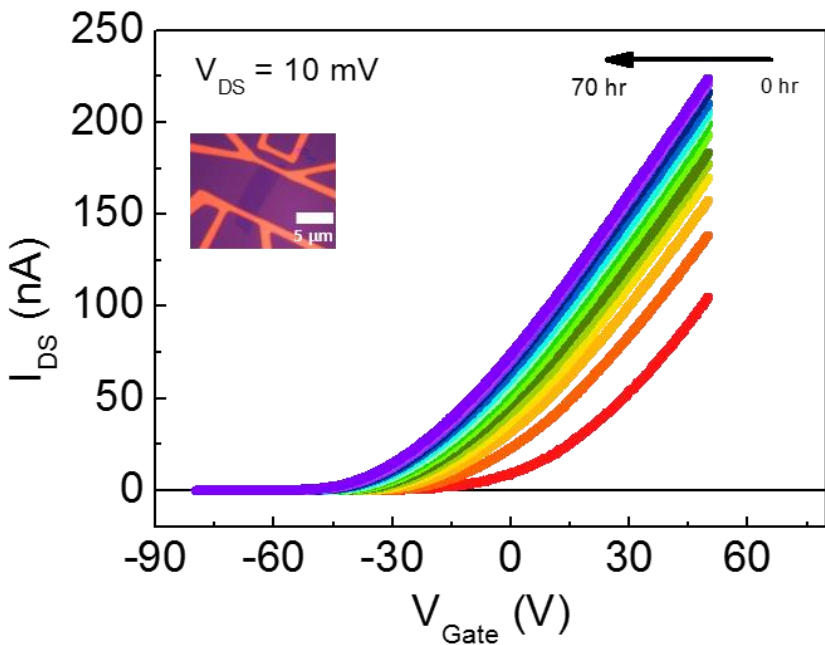


Figure 4.2 The transfer curves of MoS_2 as a function of H_2 exposure time at 350 K. Inset shows optical of MoS_2 device.

4.3 Result and discussion

4.3.1 Transfer characteristics

The transfer characteristics of single-layer MoS_2 as a function of H_2 exposure time at a fixed source-drain voltage, $V_{\text{DS}} = 10 \text{ mV}$ was measured. The electrical measurement was performed as at 350 K in a high-pressure and high-vacuum chamber. Figure 4.2 shows that transfer curves are shift toward negative region as increase exposure time. Shifting of the transfer curve voltage toward the negative gate voltage indicates the *n*-doping in single-layer MoS_2 . According to HDS process, hydrogen is dissociatively adsorbed on MoS_2 , creating coordinatively unsaturated site sulfur vacancy. The adsorption of hydrogen atom on the basal plane of the MoS_2

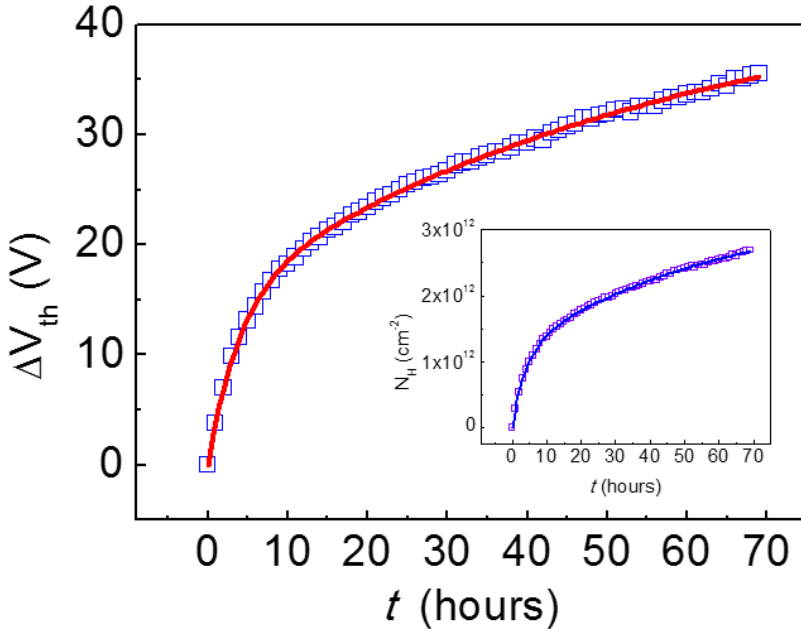


Figure 4.3 The temporal evolution of threshold voltage of MoS₂. The square is experimental data and the fitting shown by the red lines by first order adsorption model. Inset is temporal evolution of the doping induced impurities strongly affects electronic properties due to the formation of thiol(S-H) bonding. Hydrogen atom can donate an electron into the MoS₂ [11]. Furthermore, the sulfur vacancy causes the unsaturated electron in the Mo atoms which acts as electron donor to make electron rich system [12]. Both hydrogen adsorption and creating sulfur vacancy on basal plane of MoS₂ are attributed to more electron doped MoS₂. To investigate the adsorption mechanism, we measured time dependent the threshold voltage (V_{th}) evolution and electron mobility. The V_{th} is obtained by the extrapolation in the linear region (ELR) method, which is most popular extraction method for semiconductor device analysis. In the ELR method, the V_{th} is defined by the gate voltage axis intercept of the linear extrapolation of the transfer curve at its maximum first derivative point [13]. Figure 4.3 shows evolution of V_{th} and fitting line. The time dependence of V_{th} can be quantified by the first-order Langmuir type adsorption model, giving $V_{th} = V_{th\infty}(1 - e^{-t/\tau})$, where $V_{th}(t)$ is threshold voltage at time t , $V_{th\infty}$ is the steady state of V_{th} by equilibrium coverage at the fixed pressure, and

τ is the effective time constant. It turned out that the temporal evolution of V_{th} is not fitted by a single exponential model but in this case, the two major factor, sulfur vacancy and thiol bonding have an effect on *n*-type doping. So that we employ the linear combination of two term in first-order adsorption model [14], which is described as double exponential adsorption equation given by

$$\Delta V_{th} = \Delta V_1 (1 - e^{t/\tau_1}) + \Delta V_2 (1 - e^{t/\tau_2}) \quad (1)$$

We obtained the fitting parameters, ΔV_1 , τ_1 , ΔV_2 and τ_2 are 29.3 V, 59.5 h, 15.1 V and 3.9 h, respectively. The carrier density in semiconductor can be controlled by gate voltage. According to parallel plate capacitor model, the induced charge carriers are given by

$$n = \frac{c_g}{e} (V - V_{th}) = \alpha (V - V_{th}) \quad (2)$$

, where n , c_g , e and V_{th} are the induced carrier density, the gate capacitance per unit area, the electron charge, and the threshold voltage. C_g is 120 aF/ μm^2 and α is $7.5 \times 10^{10} \text{ cm}^{-2}/\text{V}$ for 285 nm thick SiO₂. Thus, the temporal evolution of the induced impurities would be given by

$$N_{imp.} = N_{Thiol}^{SAT} (1 - e^{-t/\tau_{thiol}}) + N_{SV}^{SAT} (1 - e^{-t/\tau_{SV}}) \quad (3)$$

Which is plotted as a fitting to the experimental result in inset of Fig. 4.3.

4.3.2 Mobility

Fig. 4.4 shows the field-effect mobility (μ) of single-layer MoS₂ as a function of the hydrogen exposure time. The field-effect μ of MoS₂ was obtained at the carrier density correspond to $(V_{th} - 30 \text{ V})$ using a formula, $\mu = \frac{L}{W} \frac{1}{C_g} \frac{1}{V_{DS}} (\frac{\partial I_{DS}}{\partial V_g})$, where L is the channel length, W is the channel width, $C_g = \epsilon_0 \epsilon_r A/d$ is the capacitance of gate dielectric, with $\epsilon_r = 3.9 \cdot \epsilon_0$ is the dielectric constant of SiO₂ and d is the thickness of SiO₂ and $(\partial I_{DS} / \partial V_g)$ is the transconductance (g_m) of transfer curve. V_{DS} is the source-drain voltage bias. The value of g_m is obtained by fitting of linear regime of

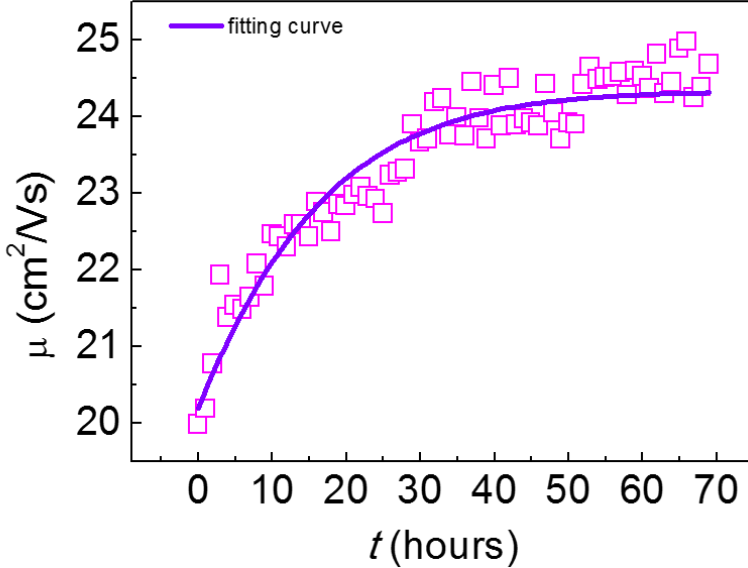


Figure 4.4 Mobility evolution as a function of hydrogen exposed time. Fitting procedures were performed using Eq. 8.

transfer curve. We observed enhancement of mobility. Hydrogen treatment also increase S-H bonding and sulfur vacancies, which acts as scattering center of basal plane of MoS₂ [15]. Moreover, it is well known that charged impurity on surface strongly limits charge transport in 2D material [16, 17]. The μ enhancement of 2D materials are interpreted that hydrogen molecules can be intercalated between the MoS₂ layer and the underlying substrate that lead to screening of long range scatterer trapped in substrate [18, 19]. We present a model regarding temporal evolution of μ using Matthiessen's rule and first-order adsorption Langmuir model. According to Matthiessen's rule, the μ of semiconductor is expressed as

$$\frac{1}{\mu_e} = \frac{1}{\mu_{Ph}} + \frac{1}{\mu_{SL}} + \frac{1}{\mu_{LR}} \quad (4)$$

, where μ_{Ph} , μ_{SL} and μ_{LR} phonon scattered, short range scattered (sulfur vacancy, thiol bonding), and long range scattered (charged impurity), respectively. We employed the first-order adsorption model to describe kinetics of hydrogen adsorption in Eq. (3) for charged impurity. The number of total impurity can be

$$N_{imp} = N_{SiO_2}^0 e^{-t/\tau_{SiO_2}} + N_{H_2}^{SAT}(1 - e^{-t/\tau_H}) + N_{SV}^{SAT}(1 - e^{-t/\tau_{SV}}), \quad (5)$$

, where $N_{SiO_2}^0$ is the initial impurity of substrate. Thus, the expression of mobility originated from charged impurity limited mobility is

$$\frac{1}{\mu_{imp}} = \frac{1}{N_{SiO_2}^0 e^{-t/\tau_{SiO_2}} + N_{H_2}^{SAT}(1-e^{-t/\tau_H}) + N_{SV}^{SAT}(1-e^{-t/\tau_{SV}})} \quad (6)$$

The short-range scattering results from sulfur vacancies and thiol bonding that is expressed by first-order adsorption Langmuir model. We obtain the expression of short-range scattered μ , which expression is

$$\frac{1}{\mu_{SR}} = \frac{1}{D_{H_2}^{SAT}(1-e^{-t/\tau_{H_2}}) + D_{SV}^{SAT}(1-e^{-t/\tau_{SV}}) + N_{SV_0}} \quad (7)$$

, where N_{SV_0} is the initial sulfur vacancies of pristine MoS₂. We consider initial phonon limited mobility (μ_{ph_0}). Since the temporal evolution of μ is measured at fixed temperature, the total expression of temporal evolution of mobility is

$$\frac{1}{\mu(t)} = \frac{1}{\mu_{ph_0}} + \frac{\frac{A}{N_{SiO_2}^0 e^{-t/\tau_{SiO_2}} + N_{H_2}^{SAT}(1-e^{-t/\tau_{H_2}}) + N_{SV}^{SAT}(1-e^{-t/\tau_{SV}})}}{\frac{B}{D_{H_2}^{SAT}(1-e^{-t/\tau_{H_2}}) + D_{SV}^{SAT}(1-e^{-t/\tau_{SV}}) + N_{SV_0}}} \quad (8)$$

, where $N_{H_2}^{SAT}$, N_{SV}^{SAT} , τ_H and τ_{SV} are the same value as obtained Eq.(3). A, B is a constant for initial value. Figure 4.4 shows temporal evolution of μ and the fitting to the Eq. (7).

4.3.3 Effect of sulfur vacancy and thermoelectric power

The hydrogen affects electronic properties on MoS₂ by both thiol bond and sulfur vacancy. The thiol bonds form metastable state. With increasing temperature, H atoms will leave the meta stable site at S atoms and overcome the potential barrier. As a result, H₂ molecules are formed, which can be physisorbed on the surface. In this state, the total energy of the system is lower than in the case of chemisorbed H atoms. The physisorbed H₂ does not affect electronic properties of the MoS₂ monolayer [20].

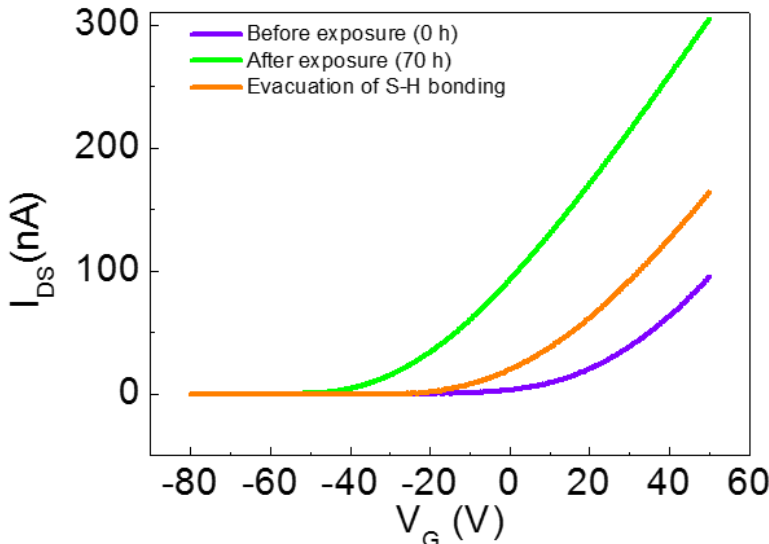


Figure 4.5 Transfer curves of MoS₂ device before (violet curve) and after (orange curve) hydrogen exposure and evacuation (yellow green)

To verify effect of sulfur vacancy on electronic properties MoS₂. We applied high vacuum ($> 10^{-6}$ torr) and high temperature (400 K) for 10 hrs to get rid of S-H bond on MoS₂. After remove hydrogen bonding on MoS₂, the sulfur vacancies are still remaining, since the creation of sulfur vacancy in HDS process is irreversible change. The transfer curves and gate voltage dependence of TEP were simultaneously measured on the same device at 300 K. Figure 4.5 shows the transfer curves of the MoS₂ before and after hydrogen exposure and evacuation. The violet, yellow green and orange curves correspond to pristine, hydrogen exposed and evacuated of MoS₂. The V_{th} was shifted from 13.7 V to -27.6V after hydrogen exposure. Then the hydrogen was evacuated at high vacuum and high temperature. As a result, the transfer curves are shifted toward positive gate bias. The V_{th} was shifted from -27.6 V to -3.1 V. The difference between evacuated value and pristine value is effect of sulphur vacancies. The fitting parameter obtained from first-order adsorption model at time dependent V_{th} is 29.3 V for the coefficient of first term and 15.1 V for the coefficient of second term of Eq. (1). We can infer whether which values correspond to hydrogen adsorption or sulfur vacancy. Consequently, the 29.3 V corresponds to hydrogenation effects and 15.1 V corresponds to sulfur vacancy effects.

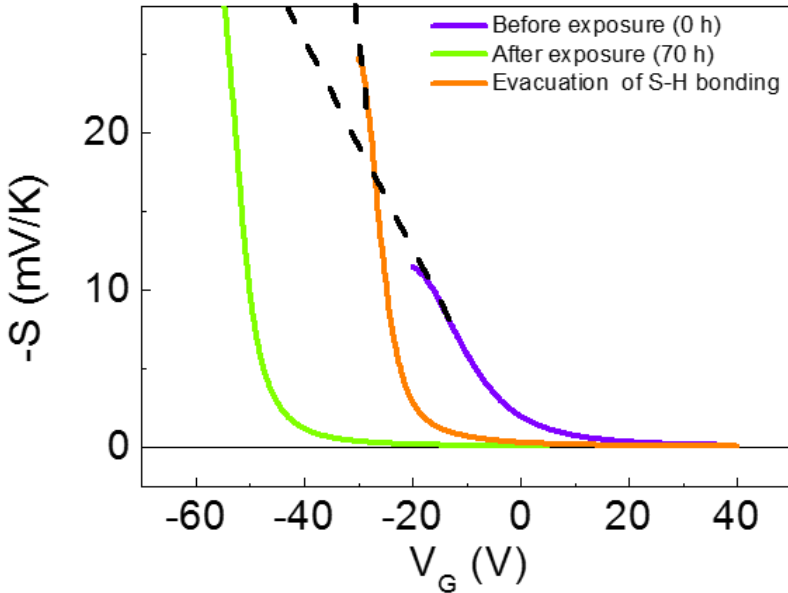


Figure 4.6 Gate voltage dependent TEP of MoS₂ device before (violet curve) and after (green curve) hydrogen exposure and evacuation (orange green)

The TEP can be used to study the intrinsic electrical properties. The TEP is sensitive probe of the electronic band structure and represents the entropy per carrier. Specifically, the TEP directly probe the sign of the majority carrier of the system.

Figure 4.6 shows the back gate dependence of the TEP before and after and evacuation. The TEP values of each case are negative, which is consistent with the *n*-type nature of MoS₂ since the sign of the TEP indicates the carrier type. There is a three distinct regime in semiconductor. As increase positive gate voltage. The TEP value become small and reach 40 μ V/K, which results from the small entropy of degenerate electron [21]. This indicates the Fermi level of MoS₂ is approaching into the conduction band, where metallic state is expected. As gate voltage decrease, the TEP starts to increase, which is understood by the large entropy of few carriers with many possible states. The Fermi level is shifted to into the bandgap. As more increase the negative gate bias, The Fermi level is entering the “off state”, where the MoS₂ has high resistance ($R > G\Omega$). After hydrogen exposure, the TEP curves is shifted toward negative gate bias regime, which indicates *n*-type doping. The Fermi level of hydrogen exposed MoS₂ is more shifted toward conduction band by *n*-doping. This is consistent with the transfer curve measurement.

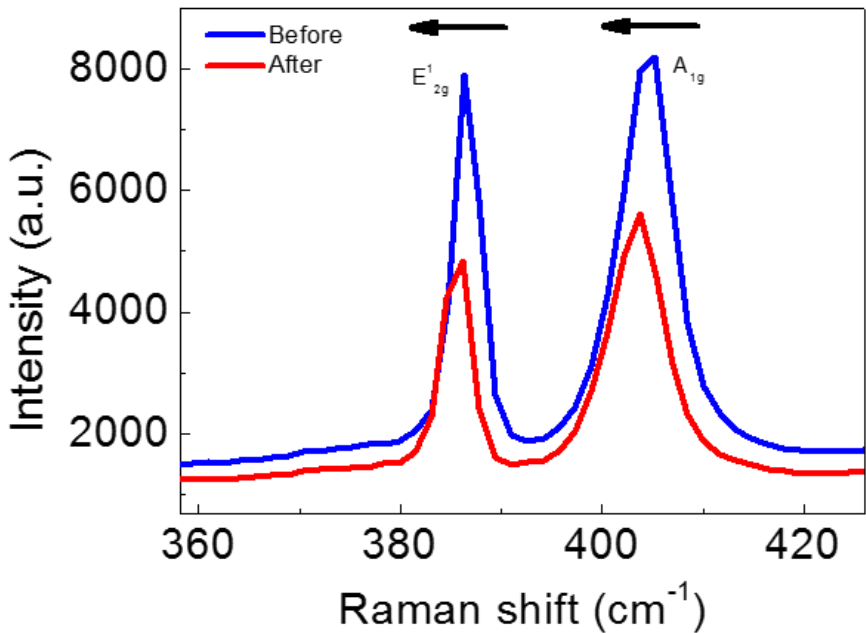


Figure 4.7 Raman spectra of pristine MoS₂ (blue curve) and Hydrogen exposed MoS₂ (red curve).

4.3.4 Raman spectroscopy

Raman spectroscopy is useful tool for probing information related to the structural change [22, 23] and electronic properties [24, 25]. Figure 4.7 shows the Raman spectroscopy of MoS₂ device before and after hydrogen exposure. The two peaks in Raman spectra, in-plane vibrational mode (E_{2g}^1) and out of plane vibration mode (A_{1g}), appear near 404.5 cm^{-1} and 386.6 cm^{-1} [26], respectively. The number of layers affects the frequency difference between two Raman peaks, indicating thickness [27]. The frequency difference of two peak is approximately 18 cm^{-1} , which indicate mono layer MoS₂. We found out that the Raman spectra of MoS₂ after hydrogen exposure shows red shifting of both E_{2g}^1 peak and A_{1g} peak compared with pristine MoS₂. A_{1g} mode is shifted from 404.5 to 403.5 cm^{-1} . Moreover, FWHM of the A_{1g} mode shows peak broadening from 5.73 to 5.95 cm^{-1} . The peak softening and broadening result in *n*-type doping [24, 25]. E_{2g}^1 mode is shifted from 386.6 to 385.5 cm^{-1} . The creation of sulfur vacancy reduced symmetry of the system. The phono frequency (ω) is

related to the restoring force constant (K) and inversion of the total mass (m) (i.e. The simple harmonic oscillator is $\omega = \sqrt{\frac{K}{m}}$), the phonon frequency can be modulated by two factors. With regard of E^{1g} mode, it corresponds to opposite in-plane vibration of Mo and S atom, the removal of sulfur atom on the top of MoS_2 leads to vibration of only one Mo and one S and the total mass of Mo-S is reduced. The restoration force of MoS_2 with sulfur vacancy is more reduced than reduction of total mass. So that the total phonon frequency is softened. On the other hand, for A_{1g} mode, The Mo atom is fixed between two S atoms in the pristine. The removal of S atom leads to vibration of Mo atom, thus, the restoring force of A_{1g} mode is medley reduced and the total mass also reduced. These two competing factors affect the phonon frequency of A_{1g} Mode. Therefore, the phonon frequency has almost same value. Moreover, it is known that the shift of E^{1g} peak attribute to the variation of lattice strain. However, H.-P. Komsa *et al.* reported that the concentration of sulfur vacancy increase, the lattice releases the stress from the lateral direction of MoS_2 edge under tensile strain from the lateral direction [28].

4.4 Summary

The exposure of MoS_2 to H_2 molecules causes the thiol bonding and sulfur vacancy on MoS_2 , which results in *n*-type doping effect. Both thiol bonding and sulfur vacancy are formed by first-order adsorption process. The electron doping is confirmed by electrical conductivity, thermoelectric power, and Raman spectroscopy. The present investigations provide not only better understanding of the interaction between the H_2 molecule and MoS_2 but also the electron doping manipulation for future electronic device applications.

Bibliography

- [1] Q. H. Wang, K. K.-Zadeh, A. Kis, J. N. Coleman and M. S. Strano, Nat. Nanotech. **7**, 699 (2012).
- [2] M. Chhowalla, H. Suk Shin, G. Eda, L.-J. Li, K. P. Loh and H. Zhang, Nat. Chem. **5**, 263 (2013).
- [3] J.A. Wilson & A.D. Yoffe, Adv. Phys. **18**, 193 (1969).
- [4] X. Cui, G.-H. Lee, Y. D. Kim, G. Arefe, P. Y. Huang, C.-H. Lee, D. A. Chenet, X. Zhang, L. Wang, F. Ye, F. Pizzocchero, B. S. Jessen, K. Watanabe, T. Taniguchi, D. A. Muller, T. Low, P. Kim and James Hone, Nat. Nanotech. **10**, 534 (2015)
- [5] J. Wu, H. Schmidt, K. K. Amara, X. Xu, G. Eda and B. Özyilmaz, Nano Lett. **14**, 2730 (2014)
- [6] A. C.-Gomez, R. Leeuwen, M. Buscema, H. S. J. van der Zant, G. A. Steele, W. J. Venstra, Adv. Mater. **25**, 6719 (2013)
- [7] A. M.-Sánchez, D. Sangalli, K. Hummer, A. Marini and L. Wirtz, Phys. Rev. B. **88**, 045412 (2013)
- [8] H. Zeng, J. Dai, W. Yao, D. Xiao and X. Cui, Nat. Nanotech. **7**, 490 (2012)
- [9] Ching Thian TyeKevin and J. Smith, Top. Catal. **37**, 129 (2006).
- [10] J.-F. Paul and E. Payen, J. Phys. Chem. B **107**, 4057 (2003).
- [11] E. W. K. Koh, C. H. Chiua, Y. K. Lima, Y.-W. Zhang, Hui, Int. J. Hydrogen Energy **37**, 14323 (2012).
- [12] H. Qiu, T. Xu, Z. Wang, W. Ren, H. Nan, Z. Ni, Q. Chen, S. Yuan, F. Miao, F. Song, G. Long, Y. Shi, L. Sun, J. Wang and X. Wang, Nat. Commu. **4**, 2642 (2013).

- [13] A. Ortiz-Conde, F.J. Gracia-Sanchez, J. Muci, A.T. Barrios, J.J. Liou and C.-S. Ho, *Microelectron, Reliab.* **53**, 90 (2013).
- [14] H. E. Romero, P. Joshi, A. K. Gupta, H. R. Gutierrez, M. W. Cole, S. A. Tadigadapa and P. C. Eklund, *Nanotech.* **20**, 245501, (2009).
- [15] J. Hong, Z. Hu, M. Probert, K. Li, D. Lv, X. Yang, L. Gu, N. Mao, Q. Feng and L. Xie, *Nat. Commun.* **6**, 6293 (2015).
- [16] S. J. Hong, H. Kang, M. Park, M. Lee, D. Soler-Delgado, D. H. Jeong, Y. W. Park and B. H. Kim, *RSC Adv.* **5**, 103276 (2015).
- [17] X. Cui, G.-H. Lee, Y. D. Kim, G. Arefe, P. Y. Huang, C.-H. Lee, D. A. Chenet, X. Zhang, L. Wang, F. Yen, F. Pizzocchero, B. S. Jessen, K. Watanabe, T. Taniguchi, D. A. Muller, T. Low, P. Kim and J. Jone, *Nat. Nanotechnol.* **10**, 534 (2015).
- [18] I. Silveste, E. A. de Morais, A. O. Melo, L. C. Campos, A.-M. B. Goncalves, A. R. Cadore, A. S. Ferlauto, H. Chacham, M. S. C. Mazzion, and R. G. Lacerda, *Nano Lett.* **7**, 6597 (2013).
- [19] B. H. Kim, S. J. Hong, S. J. Baek, H. Y. Jeong, N. Park, M. Lee, S. W. Lee, M. Park, S. W. Chu, H. S. Shin, J. Lim, J. C. Lee, Y. Jun and Y. W. Park, *Sci. Rep.*, **2**, 690, (2012).
- [20] I.N. Yakovkin and N.V. Petrova, *Chem Phys.* **434**, 20 (2014).
- [21] Y.W. Park, A. Denenstein, C.K. Chiang, A.J. Heeger, A.G. MacDiarmid, *Solid State Commun.* **29**, 747, (1979).
- [22] C. Rice, R. J. Young, R. Zan, U. Bangert, D. Wolverton, T. Georgiou, R. Jalil, and K. S. Novoselov, *Phys. Rev. B* **87**, 081307 (2013).
- [23] Y. Y. Hui, X. Liu, J. W., N. Y. Chan, J. Hao, Y.-T. Hsu, L.-J. Li, W. Guo, and S. P. Lau, *ACS Nano* **7**, 7126 (2013).
- [24] B. Chakraborty, A. Bera, D. V. S. Muthu, S. Bhowmick, U. V. Waghmare, and A. K. Sood, *Phys. Rev. B* **85**, 161403 (2012).

- [25] D. Kiriya, M. Tosun, P. Zhao, J.S. Kang and Ali Javey, *J. Am. Chem. Soc.* **136**, 7853 (2014).
- [26] J. L. Verble and T. J. Wieting, *Phys. Rev. Lett.* **25**, 362 (1970).
- [27] C. Lee, H. Yan, L.E. Brus, T.F. Heinz, J. Hone and S. Ryu, *ACS Nano* **4**, 2695 (2010).
- [28] H.-P. Komsa, S. Kurasch, O. Lehtinen, U. Kaiser and A. V. Krasheninnikov, *Phy. Rev. B* **88**, 035301 (2013).

Chapter 5

Conclusion

The effect of hydrogen on electrical properties of 2D materials are studied for the case of graphene, graphene oxide and MoS₂.

Firstly, we demonstrate local doping on single-layer graphene using selective adsorption of dissociative H₂ resulting from self-catalytic effect of graphene at room temperature. It was achieved with a PMMA window and fabricated with e-beam lithography. The CNP of the window region shifted prominently to a negative V_G compared with that of the PMMA-covered region. The hydrogen adsorption is formed by first order adsorption process at PMMA covered region and window region. According to first order adsorption model, the doping rate is relatively slow, which provide the fine control of doping on graphene. The doping rate can be modulated by control parameter such as hydrogen pressure and temperature. Moreover, the hydrogen adsorption on graphene does not cause degradation in the structural and electronic quality of graphene compare with chemical doping. Consequently, these results offer the easy means of electron doping manipulation in graphene.

Secondly, The RGO sample was prepared by bubble deposition method and thermal reduction. the electrical conductivity and thermoelectric power of single-layer RGO. The temperature dependence of conductance for entire gate voltage follows ES-VRH in the temperature range ($T < 70$ K) whereas the transport has changed above 70 K due to $k_B T > E_{CG}$. The Coulomb gap has carrier density dependence whose magnitude is reduced as increasing gate voltage. Additionally, the ES-VRH is confirmed at low

temperature and high-electric field by non-Ohmic regime ES-VRH model, $G \sim \exp(-\frac{E_0}{E})^{\frac{1}{2}}$. The obtained E_0 is suppressed as increase gate voltage, which corresponds to E_{CG} . This reduction of E_0 is consistent with E_{CG} obtained from Ohmic regime. The TEP of RGO shows that the dominant carrier in RGO can be altered by applying gate voltage. The alternation of charge carrier occurs at CNP. Furthermore, the temperature dependence TEP shows carrier density dependent transport properties which show the Mott-VRH model, which consistent with electrical conductivity at high temperature regime ($T > 70$ K). The hydrogenation of RGO shows the n-type doping and conductivity increase due to improvement in reduction efficiency. These results provide intrinsic transport properties of single layer RGO without aggregation and wrinkles. However, the sample fabrication method still insufficient for industrial application. Because the conductivity of RGO cannot be comparable with that of graphene. For that, the reduction method can be developed for high conductive RGO such as hydrocarbon solvent or hydrocarbon gas assist thermal reduction. Moreover, the bubble deposition method should be optimized for large area and uniform deposition of GO. Then, this approaches provide high performance transparent electrode.

Finally, the threshold voltage and peak of TEP of the MoS₂ device was significantly shifted toward the negative gate voltage after hydrogen exposure, which indicate n-type doping effect resulting from the thiol bonding and sulfur vacancy on MoS₂. The temporal evolution of V_{th} follows double exponential first-order adsorption process. The electron mobility increase since intercalated hydrogen suppress long range scatterer on substrate. The *n*-doping is further confirmed by TEP. We observe softening of E^{1g}_{2g} peak and A_{1g} peak resulting of electron doping and lattice strain, respectively. The present study demonstrates the possibility that the catalytic effect of MoS₂ can occur even at low temperatures and low Hydrogen pressure. The hydrogen adsorption and creation of sulfur vacancy are formed by slow rate of first order adsorption process, which offer the elaborate modulation of electronic structure of MoS₂. These significance can provide a competitive advantage in the industry. However, the interaction between hydrogen and MoS₂ on SiO₂ substrate is

still insufficient to deliver an intrinsic scattering mechanism due to the interaction of hydrogen between MoS₂ layer and substrate. So that, it is required to demonstrate MoS₂ on h-BN or suspended MoS₂ structure, which is not influenced by long range scatterer on substrate and the intercalated molecules.

Appendix

Magnetoresistance studies of 1T-TaS₂ with metallic hidden state

A.1 Introduction

Transition metal dichalcogenides (TMDs) have received much attention recently, as an attractive two dimensional (2D) materials for the study of its novel physical properties [1]. Among them, 1T-TaS₂ features three distinct charge density wave (CDW) transition with an associated lattice distortion depending on temperature [2]. The complex phases originate from lattice distortion due to Coulomb repulsion and Fermi surface instability (Fermi surface nesting) [4], forming Star-of-David of the Ta atoms with $\sqrt{13} \times \sqrt{13}$ triangular superlattice. The fully commensurate charge density wave (CCDW) state is observed in low temperature and ambient pressure, where strong electron-electron interaction localizes the electrons. That leads to insulating ground state. Near 180 ~ 225 K, phase transition occurs from CCDW to nearly commensurate charge density wave (NCCDW) state which consists of partial commensurate domain with typical size of 70 Å separated by incommensurate lattice. As temperature increases up to 355 K and 545 K, the phase becomes incommensurate charge density wave (ICCDW) and metallic state, respectively. 1T-

TaS₂ exhibits not only first order CDW transition but also additional abundant electronic phase at different condition such as reduction of thickness [5], pressure [6], gate bias [7]. Recently, ultra-fast switching between the correlated Mott insulated phase and a new metallic hidden phase in 1T-TaS₂ is observed. It is possible to be demonstrated by external perturbations such as femtosecond laser injection and short pulse current (or voltage) injection. Such external perturbations induce the increase bandwidth (W) and reduction of Coulomb repulsion energy (U) simultaneously, which drive the insulating CCDW state to critical regime of metallic state. The electronic structure and optical properties of metallic hidden state (H state) are investigated by optical spectroscopy [8, 9] and scanning tunneling microscopy [10, 11]. Therefore, the studies on magnetoresistance are expected to explore coupling between spin and charge degree of freedom in metallic hidden state of 1T-TaS₂

In this work, we measured the MR of 1T-TaS₂ with CCDW state and H state. The H state of 1T-TaS₂ is achieved by short pulse current injection at low temperature. The H state exhibit metallic behavior, which is different from Mott insulating behavior of CCDW. The MR of 1T-TaS₂ with CCDW phase shows positive MR result from intra-state interaction of electron under localization, whereas The MR of 1T-TaS₂ with metallic hidden phase shows linear MR up to 14 T without saturation.

A.2 Experimental details

1T-TaS₂ crystals were grown by chemical transport method with iodine as a transport agent with the average lateral dimensions 1–5 mm and thicknesses 100 μm. Multi-layer 1T-TaS₂ flakes were obtained by mechanical cleavage of natural 1T-TaS₂ single crystal and then transferred onto a highly *p*-doped silicon substrate with a thermally grown 285nm SiO₂. The sample is identified using optical microscopy and the thickness of multi-layered 1T-TaS₂ was confirmed by tapping mode of Atomic Force Microscope(AFM). Electrode were fabricated by standard electron beam lithography and metal evaporation of (Cr/Au 5/200 nm) and lift off process. Prior to transport

properties, 1T-TaS₂ device was annealed with Ar flow at 180 K for 6 hours to make better electrical contact. The transport measurements were performed using standard four probe technique with delta mode of Keithley 6221 current source and 2182A nanovoltmeter in 14 T superconducting magnet equipped with a variable temperature inset (VTI) for measurements at temperature between 1.4 K and 360 K. The magnetic field is applied perpendicular to the sample. The switching from CCDW state to H state were performed by applying short current pulse (the 4~5 mA and 100- μ s duration) using pulse mode of Keithley 6221 current source and 2182A nanovoltmeter.

A.3 Result and Discussion

A.3.1 Temperature dependence of resistance

Figure A.1 shows temperature dependence of resistance (R vs T) in typical 1T-TaS₂ flake and the short pulse current induced switching from CCDW state to H State. The R vs T of pristine 1T-TaS₂ is plotted by red (temperature down-sweep) and blue (temperature up-sweep) curves. It is clearly shown the first order phase transition from NCCDW state to CCDW state near 160 K in cooling. On warming from the CCDW phase, it starts to transit from CCDW to NCCDW at about 220K. Then it merges cooling curve of NCCDW. The R vs T of 1T-TaS₂ with H state is plotted by green curve. The H state transition in 1T-TaS₂ crystal is induced by short pulse current injection. The resistance drops about 2~3 order of magnitude and maintain in this state for a long time at low temperature (below 60 K). The resistance of H state shows metallic behavior from 1.6 K to 60 K. Then, the resistance state to increase rapidly to 100 K. where it merges with the temperature warming curve of the pristine. The H state can revert back to original CCDW state by electrical joule heating or thermal heating [12].

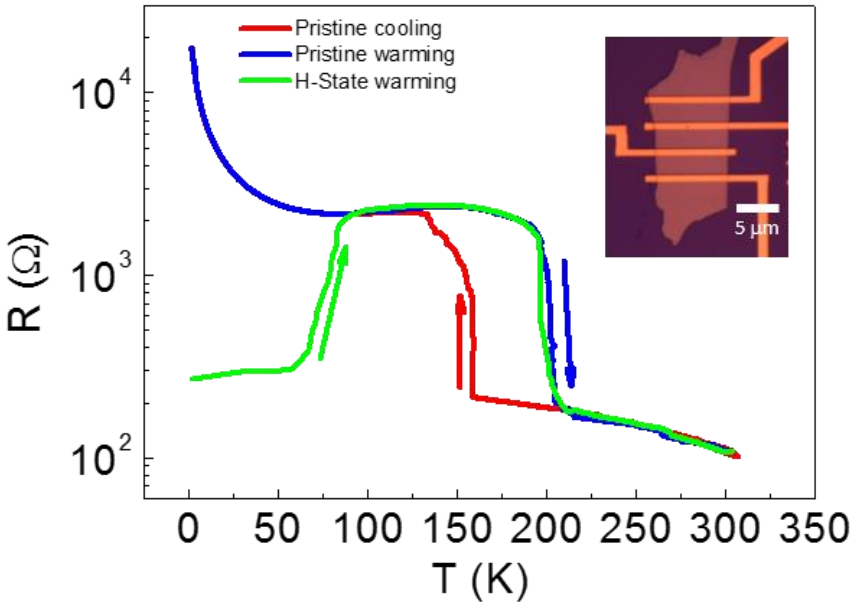


Figure A.1 Temperature dependence of the four probe resistance on temperature sweep. Red and blue curves are resistance of pristine sample, which is measured cooling and warming, respectively. Green curve is the resistance in H state. Inset : optical image of device.

A.3.2 Magnetoresistance of 1T-TaS₂ with CCDW state

Figure A.2 shows the temperature dependent transverse MR of 1T-TaS₂ with CCDW state, where $MR = \Delta R/R(0) = [R(B) - R(0)]/R(0)$. MR shows quadratic behavior at low magnetic field and then gradually change to linear dependence and finally saturated at high magnetic field. The MR is negligible above 15 K. The positive MR of strong localized system can be explained by the intra state interaction between electrons in the localized state, called spin dependent variable range hopping (VRH) [13]. The hopping rates from one site to another site can be expressed as a function of each energy level of the states and the intra state correlation energy. In the absence of the magnetic field, four possible hopping process contribute to the conduction. In

the presence of a magnetic field, the spins of singly occupied (SO) states become parallel to the field. Therefore, the hopping probability of finding a pair of SO states with anti-parallel spins becomes smaller with increasing a magnetic field, and the hopping processes from SO to SO states is suppressed because a state cannot accommodate two electrons with the same spin due to Pauli exclusion principle. The processes from doubly occupied to unoccupied states also become suppressed because they are connected to the SO to SO processes by the detailed balance. Meanwhile, the remaining two types of processes are rarely affected by a magnetic field. Therefore, the MR is positive and saturates above a certain magnetic field where only the two types of processes can contribute to the hopping conduction. The MR gradually decreases with temperature increase due to thermal fluctuation of spin.

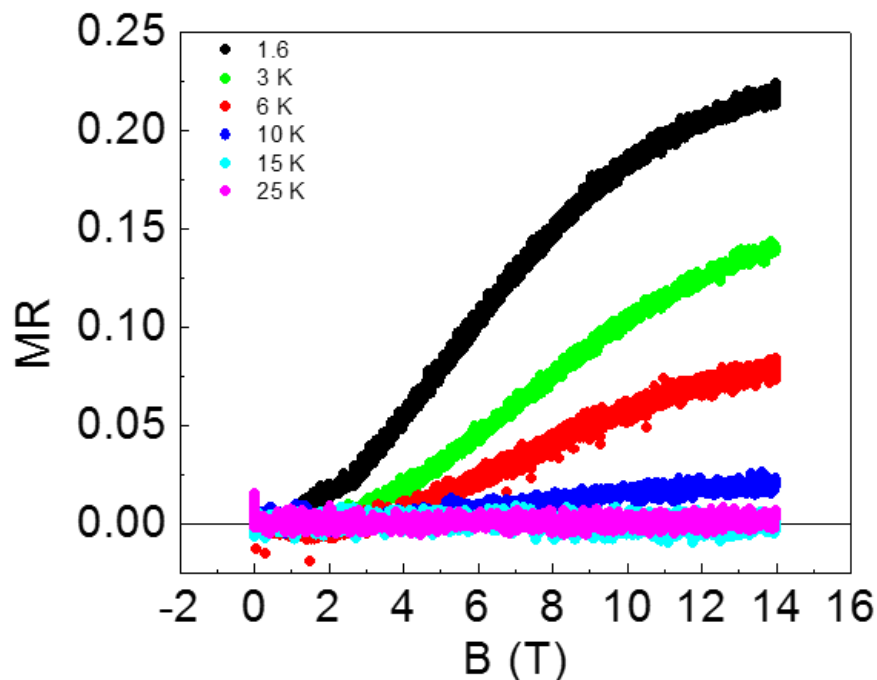


Figure A.2 MR of 1T-TaS₂ with CCDW State at 1.6, 3, 6, 10, 15, 25 K.

A.3.3 Magnetoresistance of 1T-TaS₂ with CCDW state

Figure A.3 shows transverse MR of H state at different temperature. MR decrease rapidly with increasing temperature and it is nearly negligible above 30 K. It is clearly shown that MR increase linearly with B in entire field. MR reaches 2.5 % at 1.6 K and upon 14 T. The linear magnetoresistance (LMR) can be observed in inhomogeneous system with disorder. Such a LMR is expected to be governed by the carrier mobility. Classically, Parish and Littlewood [14] have proposed that LMR can originate in inhomogeneous conductors from distortions in the current paths, which is induced by macroscopic spatial fluctuations in the carrier mobility. When the CCDW phase are injected short pulse current. The phase of the CDW changes abruptly across the domain wall and they form disordered network. The lattice structure of 1T-TaS₂ with H state consists of metallic domain surrounded by the pristine CCDW state, which is randomly distributed on the 1T-TaS₂. The domain distribution is confirmed by STM [10, 11]. Therefore, 1T-TaS₂ with randomly distributed H state domains and CCDW domains are considered as a inhomogeneous conductor.

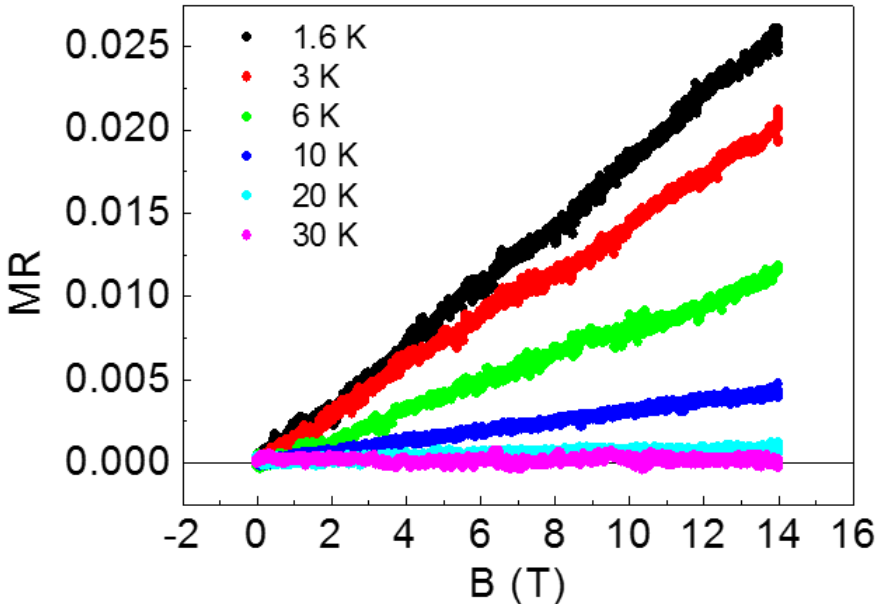


Figure A.3 MR of 1T-TaS₂ with H state at 1.6, 3, 6, 10, 15, 25 K

A.3 summary

We measured the MR of 1T-TaS₂ with CCDW state and H state. The H state is demonstrated by short pulse current injection. In CCDW state, the temperature dependent of resistance shows strong localized insulating behavior and MR follows spin dependent VRH. In H state, on the other hand, the temperature dependent resistance exhibits metallic behavior and MR shows the linear magneto resistance resulting from inhomogeneity of the metallic paths in the H state.

Bibliography

- [1] Q. H. Wang, K. Kalantar-Zadeh, A. Kis, J. N. Coleman and M. S. Strano, *Nat. Nanotech.* **7**, 699 (2012).
- [2] P. Fazekas and E. Tosatti, *Philos. Mag. B* **39**, 229 (1979).
- [3] F. Clerc, C. Battaglia, M. Bovet, L. Despont, C. Monney, H. Cercellier, M. G. Garnier, P. Aebi, H. Berger and L. Forró, *Phys. Rev. B* **74**, 155114 (2006).
- [4] M. Bovet, D. Popovic, F. Clerc, C. Koitzsch, U. Probst, E. Bucher, H. Berger, D. Naumovic and P. Aebi, *Phys. Rev. B* **69**, 125117 (2004).
- [5] M. Yoshida, Y. Zhang, J. Ye, R. Suzuki, Y. Imai, S. Kimura, A. Fujiwara and Y. Iwasa *Sci. Rep.* **4**, 7302 (2014).
- [6] B. Sipos, A. F. Kusmartseva, A. Akrap, H. Berger, L. Forró and E. Tutis, *Nat. Mater.* **7**, 960 (2008).
- [7] Y. Yu, F. Yang, X. F. Lu, Y. J. Yan, Y.-H. Cho, L. Ma, X. Niu, S. Kim, Y.-W. Son, D. Feng, S. Li, S.-W. Cheong, X. H. Chen and Yuanbo Zhang, *Nat. Nanotech.* **10**, 270 (2015).
- [8] L Stojchevska, I Vaskivskyi, T Mertelj, P Kusar, D Svetin, S Brazovskii, D Mihailovic, *Science* **344**, 177 (2014).
- [9] I. Vaskivsky, J. Gospodaric, S. Brazovskii, D. Svetin, P. Sutar, E. Goreshnik, I. A. Mihailovic, T. Mertelj, D. Mihailovic, *Sci Adv.* **1**, e1500168 (2015).
- [10] L. Ma, C. Ye, Y. Yu, X. F. Lu, X. Niu, S. Kim, D. Feng, D. Tománek, Y.-W. Son, X. H. Chen and Yuanbo Zhang, *Nat. Commu.* **7**, 10956 (2016).
- [11] D. Cho, S. Cheon, K.-S. Kim, S.-H. Lee, Y.-H. Cho, S.-W. Cheong and H. W. Yeom, *Nat. Commun.* **7**, 10453 (2016).

- [12] I. Vaskivskyi, I. A. Mihailovic, S. Brazovskii, J. Gospodarcic, T. Mertelj, D. Svetin, P. Sutar and D. Mihailovic, Nat. Commun. **7**, 11442 (2016).
- [13] A. Kurobe and H. Kamimura, J. Phys. Soc. Jpn, **51**, 1904 (1982).
- [14] M. M. Parish and P. B. Littlewood, Nature **426**, 162 (2003).

국문 초록

2차원 물질이 가지고 있는 흥미로운 특성때문에 과학적 관심을 많이 받고 있다. 수많은 2차원 물질중, 그래핀이나 전이 금속 이유화 물질 중 하나인 이황화 몰리브데늄은 표면적 대비 체적 비, 저 잡음, 주변환경에 대한 전기적 특성의 민감성 때문에 가스센서, 유연한 전자소자, 에너지 수확 응용 물질로 유망한 후보임을 보인다. 그렇기 때문에 2차원 물질과 수소의 상호작용에 대한 연구가 실험과 이론으로 진행되고 있다. 그래서 2차원 물질의 소자로서의 응용성과 2차원 물질이 수소저장 물질로서의 응용 가능성 때문에 2차원 물질과 수소의 상호작용에 대한 연구는 필수 적이다. 이 학위 논문에서는 수소가 2차원 물질, 그래핀, 그래핀 산화물, 이황화몰리브데늄의 전기적 특성에 주는 영향을 전기전도도, 열 전기력 특성, 라만 스펙트럼을 통하여 연구 하였다.

첫번째로 우리는 수소의 부분적 흡착을 통한 단 겹 그래핀의 PN 접합 제작을 소개 한다. 부분적이 수소 흡착은 그래핀 소자에 폴리메틸 메타크릴레이트(PMMA)를 이용하여 부분적으로 윈도우를 만들어 수소화 하였다. 그래핀 소자의 저항의 게이트 의존성을 350 K의 온도에서 12기압의 수소 흡착 시간에 따라 측정을 하였다. 시간에 따른 디락 점의 이용은 PMMA가 덤혀져 있는 부분과 PMMA 창이 뚫려 있는 부분 둘다 이동 정도가 다르지만 두 부분 모두 랜덤어 흡착 모델에 따라 이동됨을 확인 하였고 그래핀 소자 전체 부분의 저항의 게이트 의존성을 확인 함으로써 PN 접합이 형성 된 것을 확인 하였다.

두번째로는 환원된 단 겹 그래핀 산화물의 전하 수송 과 수소화에 대해서 논할 것이다. 시료는 단 겹의 그래핀 산화물을 방울증착 방법을 이용하여 실리콘 기판에 샘플을 만들었고 1000 °C에서 환원하여 제작을 하였다. 환원된 시료의 구조 분석은 X선 전자분광법과 라만분광법을 사용하여 환원된 시료의 구조분석 및 환원 효율을 분석 하였고, 환원된 시료는 82퍼센트의 탄소를 함유하고 있으며 샘플의 격자 결함간 거리는 약 2 nm이다. 시료의 전달 특성은 모든 온도에 대하여 양극성을 보이며 전도도는 온도가 내려갈수록 급격하게 감소를 하게 되며 이것은 가변범위도약 (Variable range hopping)의 특성이다. 전도도의 온도 의존성은 70 K 이하에서 전도도가 Efros-Skhlovskii 가변범위도약 주요한 전하수송현상이지만 70 K 이상의 온도에서는 되면 쿨롬캡에너지가 더 이상 영향을 주지 않기 때문에 2차원 가변범위 도약으로 바뀌게 된다. 열 전기력의 게이트 의존성로부터 주요 전하 운반체가 전하중성점에서 바뀌는 것을 확인 하였고 게이트 전압이 양 일 때는 전자, 음일 때는 전공에 의한 전도가 일어남을 확인 하였다. 열 전기력의 온도 의존성은 $50 \text{ K} < T < 300 \text{ K}$ 범위에서 2차원 가변범위도약 현상을 따르는 것을 알 수 있다. 환원된 그래핀 산화물에 수소화를 하게 되면 수소 흡착에 의한 전자도핑이 되는 것을 확인 하였고 전달 특성의 최고 저항 값은 감소하게 되는데 이것은 환원된 그래핀 산화물이 수소 분위기에서 환원 효과가 증가 되었기 때문이다.

세번째로는 수소가 단 겹의 이황화몰리브데늄의 전기적 구조적변화에 대해 논할 것이다. 이황화 몰리브데늄은 수소탈황공정의 촉매로 잘 알려져 있으며 수소가 이황화몰리브데늄의 활성화에 중요한 역할을 하게 된다. 그래서 수소와 이황화 몰리브데늄의 상호작용에 대한 연구는 수소탈황공정, 특히 이황화 몰리브데늄의 수소 흡착 및 황빈자리형성에 대한 이해를 하기 위해서

필요 하다. 이황화 몰리브데늄의 전달 특성을 350, 12 기압의 수소 흡착 시간에 따라 측정을 하였다. 시간에 따라 문턱 전압이 음의 게이트 전압으로 이동하는 것을 확인 하였고 이것은 수소 흡착과 황 빈자리에 의한 결과이다. 시간에 따른 문턱 전압의 이동은 수소 흡착과 황 빈자리 항으로 구성된 이중 지수로 된 랭류어 흡착 모델에 따라 형성되었다. N형 도핑은 열 전기력 측정으로 통하여 확인 하였는데. 전달 특성 특성과 마찬가지로 열 전기력의 게이트 의존성 또한 음의 게이트전압쪽으로 이동을 하였다. 그리고 라만의 두 특성 피크가 적색 편의를 보이게 되었는데 이것은 전자 도핑과 격자의 인장 변형에 의한 것이다.

주요어 : 그래핀, 이황화몰리브데늄, 전자 도핑, 수소화, 그래핀 산화물, 가변범위도약, 열 전기력.

학번: 2010-22667